Dissertation
submitted to the
Combined Faculties of the Natural Sciences and Mathematics
of the Ruperto-Carola University of Heidelberg, Germany
for the degree of
Doctor of Natural Sciences

Put forward by

Dipl.-Phys. Philippe H. M. Bräunig

born in Mainz, Germany

Oral examination on December 17th of 2014

Atom Optical Tools for Antimatter Experiments

Referees: Prof. Dr. M. K. Oberthaler
Prof. Dr. U. Uwer

Abstract:

The direct measurement of the gravitational acceleration of antimatter in the earth's field, which represents a test of the weak equivalence principle, is in the focus of several ongoing experimental attempts. This thesis investigates tools and techniques known from the field of atom optics that can be utilised for such a measurement with antihydrogen atoms as envisioned by the AEgIS collaboration. A first experimental step is presented, in which a deflection due to an electromagnetic force acting on antiprotons is measured with a moiré deflectometer. This device, which can be described with classical particle trajectories, consists of two gratings and a spatially resolving detector. Key elements of this measurement are the use of an emulsion detector with high spatial resolution and an absolute reference technique based on an interferometric fringe pattern of light, which is not deflected by forces. For future realisations, a new detection and evaluation scheme to measure gravity based on a three-grating system enclosed by a vertex-reconstructing detector is discussed. This allows the use of a grating periodicity that is smaller than the resolution of the detector while making efficient use of the particle flux. Smaller periodicities are favourable to increase the inertial sensitivity of the measurement apparatus but require to take effects of diffraction into account. To explore this near-field regime with antimatter, a Talbot-Lau interferometer for antiprotons is proposed and its possible experimental implementation is discussed.

Zusammenfassung:

Die direkte Messung der Beschleunigung frei fallender Antimaterie, die einem Test des schwachen Äquivalenzprinzips entspricht, ist das Ziel mehrerer sich im Aufbau befindender Experimente. Die vorliegende Arbeit untersucht Instrumente und Methoden aus dem Arbeitsgebiet der Atomoptik im Hinblick auf eine solche Messung mit Antiwasserstoff, wie sie von der AEgIS Kollaboration beabsichtigt wird. In einem ersten experimentellen Schritt wurde die Ablenkung von Antiprotonen durch eine elektromagnetische Kraft mit einem Moiré Deflektometer gemessen. Dieses Gerät, welches mit klassischen Teilchenbahnen beschrieben werden kann, besteht aus zwei Gittern und einem ortsaufgelösten Detektor. Entscheidende Aspekte dieser Messung sind der verwendete hochauflösende Emulsionsdetektor und eine absolute Referenzierungstechnik, die auf mit Interferometrie erzeugten Lichtstreifen beruht, die durch Kräfte nicht verschoben werden. In zukünftigen Messungen könnte ein neues Detektionsschema Verwendung finden, welches die Nutzung von Gittern ermöglicht, deren Periodizität kleiner ist als die Ortsauflösung des verwendeten Detektors. Hierzu wird das System um ein weiteres Gitter ergänzt und von einem Vertex rekonstruierenden Detektor umgeben, um die zur Verfügung stehende Teilchenstatistik effizient auszunutzen. Die Verwendung einer kleineren Gitterperiode birgt den Vorteil, dass hiermit die Empfindlichkeit des Messinstruments bezüglich Beschleunigungen erhöht werden kann; erfordert jedoch, die auftretenden Beugungseffekte zu berücksichtigen. Um diesen Nahfeldbereich mit Antimaterie zu erforschen, wird die Möglichkeit diskutiert, ein Talbot-Lau Interferometer für Antiprotonen zu realisieren.

‘But in any event, it is in the hands of our generation to perform an experiment to measure the gravitational acceleration of antimatter. Some day it will be done, whether we do it or not. It will be done. If we do not do it, and the answer eventually turns out to be what we expect, then future generations will look back upon us and say it was a shame. But if the answer turns out to be a surprise, then, if we do not do it, future generations will look back upon us and say we were fools.’

M. M. Nieto et al. Theoretical Motivation for Gravitation Experiments on Ultra-Low Energy Antiprotons and Antihydrogen. arXiv, 1994.

Contents

1. Introduction

The weak equivalence principle is a cornerstone of today's understanding of gravity. Its earliest formulation goes back to Galileo Galilei who noted

> '...veduto, dico, questo, cascai in opinione che se si levasse totalmente la resistenza del mezzo, tutte le materie descenderebbero con eguali velocità.' [1],

which translates to

> 'Having observed this I came to the conclusion that, if one could totally remove the resistance of the medium, all substances would fall at equal speeds.' [2].

Newton pointed out that this universality of free fall is equivalent to the inertial mass being proportional to the gravitational mass [3]. Up until now the weak equivalence principle (WEP) has been thoroughly tested with a wide variety of matter systems [4–7], however, since Anderson's discovery [8] of the positron, which was predicted by Dirac [9], one has wondered if the weak equivalence principle also applies to this new kind of matter known as antimatter. Many theoretical arguments [10–12] contradict the possibility of such a violation of the WEP, especially as in the framework of general relativity gravity is described as a geometrical phenomenon and objects in free-fall simply follow straight lines in curved space-time. Additionally, some experimental arguments [13–18] set tight constraints on the gravitational acceleration of antimatter, which is often denoted $\bar{g}$. On the other side these arguments are somehow indirect as they are based on assumptions and models. And the knowledge of antimatter and gravity is known to be incomplete. Prominent examples are the absence of larger quantities of antimatter in the universe, the missing unification of gravity with the other fundamental forces and that visible matter only accounts for 4 % of the matter content in the universe. These have led physicists to investigate new theories of gravity, often involving additional hypothetical vector or scalar bosons [19–22]. To address this question experimental physicists have tried to perform a direct measurement of the gravitational acceleration of an antimatter system for nearly five decades. Whatever the outcome of such an experiment would be, be it that antimatter falls as expected or not, the experiment will be 'A classic, one for the textbooks' [23]. The early experiments [18, 24, 25] aiming at direct measurements of $\bar{g}$ used charged, elementary antimatter particles and were consequently plagued with shielding problems, however, techniques of trapping, cooling, and manipulation

of charged antimatter particles have seen substantial progress in last two decades. This has ultimately resulted in the synthesis of antihydrogen atoms [26, 27] in 2002, which has opened the door to directly measure the gravitational acceleration using this neutral antimatter system. Several independent experimental [28–30] attempts are underway to investigate the gravitational acceleration of antihydrogen although some experiments lay their focus on other exotic atoms such as positronium [31] or muonium [32], which are also intriguing as these represents purely leptonic systems.

Another field of physics, in which substantial progress has been achieved over the last decades, is the field of atom optics, hence, the manipulation of uncharged matter. Many of the early experiments of this field focused on demonstrating effects with atomic or molecular beams, which were already known from optics. Prominent examples are the diffraction of atoms by a transmission grating [33], the double-slit experiment with atoms [34] and atom interferometers in the far- [35] and near-field [36, 37] regime. All these experiments have in common that they explored the wave character of matter, which was predicted by de Broglie. This distinguishes them from devices working the classical regime such as the moiré deflectometer [38]. This limit between classical and wave-mechanical regime is still being pushed, for example by experiments performing interferometry with increasingly heavy molecules [39, 40]. On the other side, the experimental tools and techniques of atom optics have developed from these early proof-of-principle experiments to reliable instruments of metrology with unprecedented sensitivity. There is an increasing number of experiments that use tools from atom optics to explore fundamental questions outside the field of atom optics itself. Paradigm examples are Raman interferometers based on atomic fountains [41–46], which – unsurprisingly – are being used to test the weak equivalence principle with matter.

The AEgIS (Antimatter Experiment: gravity, Interferometry, Spectroscopy) collaboration envisions the use of a moiré deflectometer, which is a classical tool from atom optics, to directly measure the gravitational acceleration of antihydrogen. This would expand the range of systems for which the weak equivalence principle has been directly tested to neutral antimatter.

1.1. Contents of this Thesis

This thesis focuses on the moiré deflectometer and its wave-mechanical counterpart, the Talbot-Lau interferometer for the use within the AEgIS experiment. The chapters are organised as follows: The remaining part of the introduction gives a brief overview on two existing, indirect measurements of the gravitational acceleration of antimatter. This is complemented with the description of planned experiments at CERN, which aim to perform a direct measurement – one of which is the AEgIS experiment. The second chapter establishes the required theoretical basis by reviewing the atom optical tools in question with the emphasis on the limit between the classical and the wave regime. This includes a general discussion on the inertial sensitivity of such devices and their critical dependence on the temperature of the produced antihydrogen. Chapter 3 reports on the results of a moiré de-

flectometer for antiprotons, which is simultaneously a Talbot-Lau interferometer for visible light. The approach followed in this experiment demonstrates how the sign of a force can be determined without having time-of-flight information on single events. Chapter 4 describes a new detection scheme including an adequate evaluation based on an unbinned maximum likelihood estimator. This approach does not require a spatially resolving detector as foreseen in the AEgIS proposal and opens the possibility to increase the experiment's sensitivity by using gratings with a smaller periodicity and pushing the device into the wave regime. Such Talbot-Lau interferometer, here for the use with antiprotons, is proposed in chapter 5 to examine the feasibility of such a device in the next experimental step.

1.2. Indirect Experimental Limits on the Gravitational Acceleration of Antimatter

It is important to be aware that indirect measurements exist, which set limits on a possible violation of the weak equivalence principle for antimatter. These limits are lower than the precision of planned experiments. Two of these arguments are reviewed in the following.

1.2.1. Trapped Protons and Antiprotons as Reshifted (Anti-) Clocks

Precise measurements have been reported on the ratio of the inertial mass m_i of the proton and the antiproton based on comparison of their cyclotron frequencies $\omega = eB/m_i$ in the magnetic field of a Penning trap [47–49]. These represents sensitive tests of the charge, parity, and time symmetry (CPT). Under the assumption that CPT is conserved, one can alternatively argue that measurements of this type represent a test on the weak equivalence principle. Hughes et al. [13] express this argument as follows. The trapped particles or antiparticles represent local clocks or local anticlocks, respectively. If the clocks are placed in a gravitational field, they are subject to gravitational redshift. If antiprotons couple differently to the gravitational field, whereby α in $\bar{g} = \alpha\, g$ deviates from unity, the two clocks should experience a different gravitational redshift and therefore exhibit different frequencies. The frequency difference that one should observe is derived [13] to be

$$\frac{\bar{\omega}_C - \omega_C}{\omega_C} = 3(\alpha - 1)\frac{U}{c^2} \ , \tag{1.1}$$

where U represents an absolute gravitational potential. Consequently, the observation of a frequency difference would mean that one is no longer free to choose the offset of the gravitational potential as known from Newtonian physics. This is inevitable when the weak equivalence principle is violated. The most convenient choice is then to set the zero of this absolute field to infinity, so that the frequency difference vanishes in the absence of gravity. For the absolute potential, one can use the value of our local supercluster of $|U/c^2| \approx 3 \cdot 10^{-5}$. Hughes et al. [13] concluded from the precision of the frequency ratio of $4 \cdot 10^{-8}$ reported in [48], that $|\alpha - 1| < 5 \cdot 10^{-4}$. Consequently, the gravitational acceleration of antiprotons cannot differ by more than $5 \cdot 10^{-4}$. One should note, however, that the precision of the measurements on the inertial mass ratio has meanwhile improved [49] by two orders of

magnitude, which lowers this limit further. Even though this measurement is commonly considered a strong indirect measurement, it has also been challenged. For example Fischler et al. [20] state 'That is, in order to use the absolute potential based arguments to interpret these results as limiting possible antimatter asymmetry, one must logically start with the premise that General Relativity holds in its particulars, and thus that antimatter asymmetry cannot be present *a priori*.'.

1.2.2. Neutral Kaons as a Weak Equivalent Test

If the antiproton experiences a different gravitational acceleration as the proton, this should translate to the quark level, meaning that there is a different gravitational coupling of quarks and antiquarks. A possible deviation should therefore also be observable in mesons such as the kaon [14]. A test of the weak equivalence principle based on the decay of K^0 and $\bar{K}^0$ into $\pi^+\pi^-$ at CPLEAR is reported by A. Apostolakis et al. [15]. Neutral kaons are an interesting system, as their states mix through the weak interaction, which is described by the mass matrix

$$M = \begin{pmatrix} M_{K^0} & \Delta m/2 \\ \Delta m/2 & M_{K^0} \end{pmatrix} , \tag{1.2}$$

where $\Delta m = m_{\mathrm{L}} - m_{\mathrm{S}}$ denotes the mass difference between the short (S) and long (L) living state. As the neutral kaon system violates the CP symmetry, these states are not pure, but superpositions of the CP eigenstates $K_1 = \left(|K^0\rangle - |\bar{K}^0\rangle\right)/\sqrt{2}$ and $K_2 = \left(|K^0\rangle + |\bar{K}^0\rangle\right)/\sqrt{2}$:

$$|K_S^0\rangle = \frac{1}{\sqrt{1+|\epsilon|^2}} \left(|K_1^0\rangle + \epsilon |K_2^0\rangle\right) \tag{1.3}$$

$$|K_L^0\rangle = \frac{1}{\sqrt{1+|\epsilon|^2}} \left(|K_2^0\rangle + \epsilon |K_1^0\rangle\right) \ . \tag{1.4}$$

The parameter ϵ represents the magnitude of the CP violation. If there are different interactions of K^0 and $\bar{K}^0$ with the gravitational field[1], denoted g and $\bar{g}$, the effective mass difference of $K^0 - \bar{K}^0$ is then given by [50]:

$$\delta m_{\mathrm{eff}} = M_{K^0}(g - \bar{g}) \frac{U}{c^2} \left(1 + \frac{v^2}{c^2}\right) \gamma^2 e^{-r/r_2} \tag{1.5}$$

where v is the speed of the Kaon, $\gamma = 1/\sqrt{1 - v^2/c^2}$ and r_2 is the range of the interaction. If the gravitational potential U and thus the effective mass difference δm_{eff} varies, the time evolution of K^0 and $\bar{K}^0$ would change differently causing a variation of the magnitude of the CP violation. The analysis is based on data accumulated by CPLEAR over a period of three years. It looks for annual, monthly and diurnal modulations in the experimental observables $|\eta_{+-}|$ and ϕ_{+-} of the CP violation, but no modulation is observed. Using the known variations of the gravitational potential caused by the relative motion of earth, moon and sun

[1] Assuming a tensor gravitational interaction. The effective mass difference for vector and scalar interactions can be found in [15].

one can determine limits for tensor, vector and scalar mediated gravitational interactions. The resulting upper limits are given in table 1.1 and are much lower than the envisioned precision of the proposed direct measurements on antihydrogen. On the other hand one should note that the argument requires exact CPT and that kaons are not baryons.

Table 1.1.: Limits on $|g - \bar{g}|$ reported in [15] for spin 0, 1 and 2 interactions.

variation of potential	spin 0	spin 1	spin 2
earth	$6.4 \cdot 10^{-5}$	$4.1 \cdot 10^{-5}$	$1.7 \cdot 10^{-5}$
moon	$1.8 \cdot 10^{-4}$	$7.4 \cdot 10^{-5}$	$4.8 \cdot 10^{-5}$
sun	$6.5 \cdot 10^{-9}$	$4.3 \cdot 10^{-9}$	$1.8 \cdot 10^{-9}$

1.3. Direct Measurements of the Gravitational Acceleration of Antihydrogen

J. Walz and T. W. Hänsch made a descriptive argument [51] why directly measuring the gravitational acceleration of antihydrogen represents such a formidable experimental challenge. The main difficulty is not the production of antihydrogen, which is certainly difficult enough, it is the production of antihydrogen with a sufficiently low temperature. If one wants to perform a direct experiment, meaning an experiment which is comparable to a Galilei-like free fall experiment [1] or Newton's omnipresent falling apple [3], one needs to know the antihydrogen's start condition in space and velocity. Assuming a production of an ensemble of antihydrogen atoms with temperature T, of which the velocities are Maxwell-Boltzmann distributed, the spread of the vertical velocities of such a cloud is given by $\sigma_v = \sqrt{k_b T/m}$. Antihydrogen atoms with this velocity can climb in the earth's gravitational field (presuming $\bar{g} = g$) to a height of $h = k_b T/2mg$. With a glance at table 1.2, which lists these characteristic measures for several antihydrogen temperatures, it becomes apparent that for temperatures on the level of helium's boiling point $\sim 4\,\mathrm{K}$, the attained height is much larger than a reasonable experimental drop height. Each experiment at CERN's antiproton decelerator (AD) that

Table 1.2.: Spread of the vertical velocity $\sigma_v = \sqrt{k_b T/m}$ and the climbing-height $h = k_b T/2mg$ in earth's gravitational field of an antihydrogen cloud with temperature T.

$T_{\bar{H}}$	10 K	1 K	100 mK	10 mK	1 mK	100 µK	10 µK
σ_v	$280\,\mathrm{m\,s^{-1}}$	$88\,\mathrm{m\,s^{-1}}$	$28\,\mathrm{m\,s^{-1}}$	$8.8\,\mathrm{m\,s^{-1}}$	$2.8\,\mathrm{m\,s^{-1}}$	$0.88\,\mathrm{m\,s^{-1}}$	$0.09\,\mathrm{m\,s^{-1}}$
h	4000 m	400 m	40 m	4 m	400 mm	40 mm	4 mm

aims to measure the gravitational acceleration of antihydrogen tackles this difficulty from a different angle.

1.3.1. ALPHA Experiment

The ALPHA collaboration reported on a first experiment [52] using a catch and release procedure. Antihydrogen atoms are synthesised in a nested Penning-Malmberg trap by autoreasonently exciting antiprotons into a cloud of positrons. A magnetic trap [53,54] captures the low energy tail of ~ 6000 antihydrogen atoms that are produced per cycle. The trap's potential depth corresponds to a temperature of $\sim 540\,\mathrm{mK}$, which is much lower than the mean temperature of the produced atoms and results on average in one atom being trapped per trial. The atoms are kept in the trap for 400 ms to ensure their decay into the ground state. The magnetic field of the trap is then lowered to release the atoms. The atoms subsequently leave the trap isotropically to annihilate on the trap walls, the vertices of which are identified by reconstructing the annihilation products with a silicon strip tracking detector. The flight distance from the centre of the trap to the trap wall is about 20 mm, which is by orders of magnitude shorter than the atom's climbing-height at that temperature. Consequently, the number of atoms annihilating on the top of the trap is comparable to the amount annihilating on the bottom of the trap. But the comparison of the balance of the two, for which they employ a statistical model matching their experimental configuration, allows an experimental limit to be set. The conclusion of this experimental run is that the absolute value of the gravitational acceleration of antihydrogen cannot be larger than a hundred times g. Possible future improvements, such as direct laser cooling of the atoms in the trap might enable the experiment to determine the sign of g. Nevertheless, one should keep mind that direct laser cooling of hydrogen is limited to 2 mK due to the Doppler limit [51].

1.3.2. GBAR Experiment

A collaboration named GBAR, which has been commissioned by CERN, follows an approach [29,51] aiming at even lower temperatures. It is based on the synthesis of antihydrogen ions, thus an antiproton with two positrons. Being positively charged, it can be trapped in a electromagnetic trap such as a Paul trap. The hydrogen ion possesses a single bound state, which can be assumed to be true for the antihydrogen ion. This means, that the ion cannot be directly laser cooled. As it is positively charged, it can simultaneously be trapped with positive ions such as beryllium ions, which are known to exhibit strong laser cooling transitions. Therefore, they plan to sympathetically cool antihydrogen ions with a cloud of laser-cooled positive ions to reach temperatures as low as $\sim 10\,\mu\mathrm{K}$. After a complex production and cooling scheme, the envisioned gravity measurement itself is relatively simple. The ultra-cold antihydrogen ion, still trapped in the electromagnetic trap, is neutralised with a laser that detaches the ion's additional positron. The charged ion becomes a neutral atom and is no longer confined by the electromagnetic fields of the trap. Thus, it falls freely in earth's gravitational field to annihilate on a detector placed 100 mm below the trap. In this measurement scheme, the starting and arrival time are well defined, as the fall begins with the laser-induced photo-detachment of the positron and ends with the annihilation on the detector. The GBAR collaboration aims to measure $\bar{g}$ on a percent level with a few weeks of measurement time.

1.3.3. AEgIS Experiment

There are numerous examples of experiments in the field of atom optics that resolve the deflection of an atomic or molecular beam due to gravitational acceleration. These devices are either interferometers [55,56] or are working in the classical regime like the moiré deflectometer [38]. The original antihydrogen production scheme [26], which with some variation is still used by the ALPHA experiment, does not allow to direct the atoms to form a beam towards a gravity measuring device. Additionally, it is not possible to measure the time-of-flight of the atoms as the production goes on for several seconds. The initial motivation of the AEgIS experiment was to develop an antihydrogen production scheme that allows to form a pulsed beam [28,57,58]. The scheme that AEgIS collaboration pursues is depicted in figure 1.1 and is based on the charge exchange reaction

$$\bar{p} + \mathrm{Ps}^* = \bar{\mathrm{H}}^* + e^- \tag{1.6}$$

of antiprotons and Rydberg positronium, i.e. a highly excited atom consisting of an electron and a positron, to form Rydberg antihydrogen. The individual steps of the scheme work as

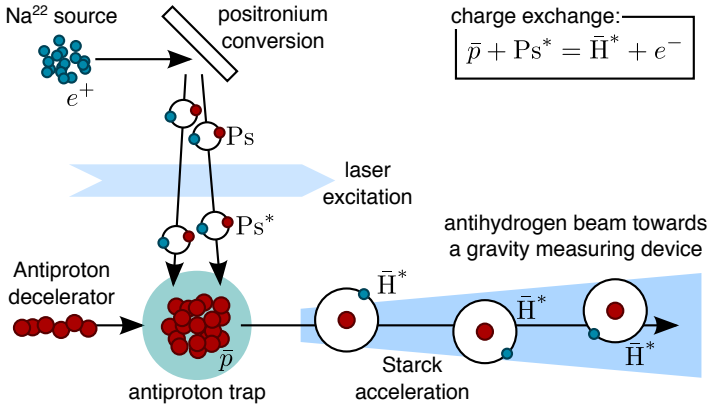

Figure 1.1.: Pulsed antihydrogen beam production as envisioned by the AEgIS collaboration [28]. The antiprotons are delivered by CERN's antiproton decelerator, trapped and cooled in several steps. The positrons are collected from radioactive sodium. In order to shape a beam, the synthesis is based on a charge exchange process of antiproton and Rydberg positronium. The large dipole moment of the excited antihydrogen atoms can be used to accelerate the atoms to form a beam towards the gravity measuring device.

follows (see figure 1.1): The antiprotons are delivered by CERN's antiproton decelerator, which provides every 90 s a bunch of $\sim 10^7$ antiprotons with a mean energy of 5.3 MeV. A fraction of the antiprotons are captured in an electromagnetic trap of the Penning style and subsequently cooled to 100 mK. The decay of the radioactive sodium isotope Na^{22} provides the positrons, which are accumulated and then implanted into a nanoporous target [59]. A fraction of the positrons thermalise with this target, forms positronium atoms with electrons from the surface of the target and subsequently escape the nanoporous material. The bunch of positronium atoms is then excited to a Rydberg state via a two-step laser excitation [60] before it crosses the trap with the cold antiprotons to form antihydrogen through the charge

exchange reaction given in equation 1.6. As the positronium is in an excited state, the synthesised antihydrogen is in an excited state as well as it inherits the inner energy of the positronium. Hence, the inner state of the antihydrogen atom can, at least to some extent, be controlled by the laser excitation of the positronium. When antihydrogen is formed, it is no longer confined by the trap, as the Penning trap only confines charged particles. But the atoms are in an excited state, which results in a large dipole moment. This can then be used to accelerate the atoms with electric field gradients, a process called Stark accleration [61–63], to form a beam of antihydrogen for a gravity measuring device.

This brief summary shows that the envisioned antihydrogen production involves very interesting physics from different fields such as particle physics, plasma physics, electromagnetic traps, cooling, atomic physics, laser physics and particle detectors. It is important to note that many experimental elements of this scheme have been individually shown to work, but the formation of antihydrogen atoms through this charge-exchange reaction remains an experimental challenge. Details on many aspect of the production can be found in the given references. For the work presented here, only two elements of this scheme are of special interest. The first one is the temperature of the antiprotons. The second one is the acceleration of the antihydrogen atoms. These parameters determine the properties of the antihydrogen beam and are discussed in detail at the end of following chapter, which focuses on tools of atom optics.

There are known knowns; there are things we know we know. We also know there are known unknowns; that is to say we know there are some things we do not know. But there are also unknown unknowns – there are things we don't know we don't know.

(Donald Rumsfeld)

2. From Moiré Deflectometry to Talbot-Lau Interferometry

The AEgIS experiment envisions to measure the gravitational acceleration of antihydrogen with a tool from atom optics. This so-called moiré deflectometer and its wave-mechanical counterpart, the Talbot-Lau interferometer are well established techniques. A wide range of theoretical [64–67] and experimental work [36–38, 55, 56, 68–79] has been reported in this field. This chapter reviews theoretical descriptions of these devices and draws conclusions that are of importance for the work with antimatter. The moiré deflectometer and the Talbot-Lau interferometer are closely related, therefore it is convenient to review both of them simultaneously. However, they exhibit distinct features that cannot be ignored and are discussed in detail. Rather than performing a Monte Carlo simulation of a specific experimental configuration, this chapter focuses on analytic descriptions in order to keep the discussion as general as possible. The approach followed is to go from a simplified to the more general description. Therefore, each new aspect is briefly introduced and then reviewed in more detail. The theoretical framework described here serves as a basis for work described in the following chapters, such as an experiment to measure forces on antiprotons with a moiré deflectometer (chapter 3) and possible future realisations of interferometers for antimatter (chapter 5).

2.1. Moiré Deflectometer

The measurement principle of the device known as a moiré[1] deflectometer [38] can be motivated by examining the simplified situation depicted in figure 2.1a. Two apertures, each consisting of an opaque material with a single slit, are placed into the path of a divergent beam of particles. The two slits restrict the particle beam to a narrow trajectory; the rest of the beam is stopped by either the first or the second aperture. The particles that pass both slits hit a detector with spatial resolution. In the absence of any force the particles perform a uniform linear motion (grey lines). If the particles are subject to a force $F = ma$, they follow parabolic trajectories (blue) and thus the position of impact on the detector is shifted by Δy with respect to the undeflected beam. This shift can be determined from the vertical

[1] The word moiré does not denote a person's name and is therefore written in lower case.

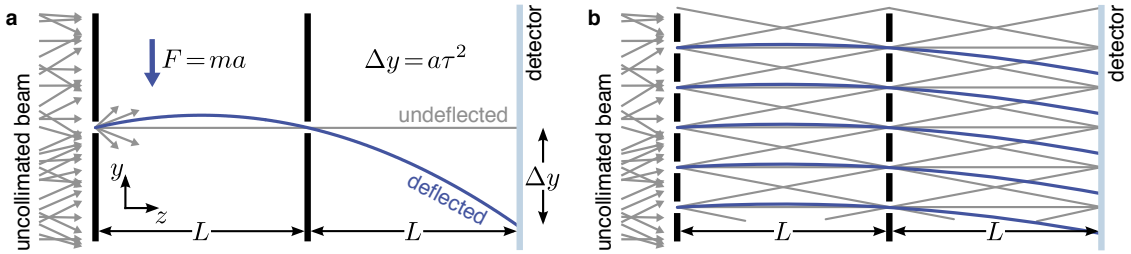

Figure 2.1.: (a) Two single slits define a possible trajectory. The particles of an uncollimated beam that pass both slits hit a spatially resolving detector. The position of the particles' impact depends on the force that acts upon them and is given by Δy. (b) The moiré deflectometer represents the generalisation of this concept. Gratings with periodicity d replace the single slits and allow an increased throughput. The result is a fringe pattern with the periodicity of the gratings.

velocity v_y at the moment of the particle's passage of the second slit and the acceleration between the second slit and the detector:

$$\Delta y = v_y \tau + \frac{1}{2} a\tau^2 = \frac{1}{2} a\tau^2 + \frac{1}{2} a\tau^2 = a\tau^2 \tag{2.1}$$

The time of flight is defined as $\tau = L/v_z$ and the vertical velocity v_y at the second slit results from the acceleration beginning on the top of the parabola, thus $v_y = a\tau/2$. This experimental approach is interesting as it is conceptually equivalent to Newton's 'apple' falling from a tree and represents a model-free measurement. The major drawback is the dramatic particle loss caused by the single slits. The use of a larger number of slits N – i.e. a grating – overcomes this limitation, as the number of possible trajectories scales with N^2, as illustrated in figure 2.1b. If the grating separation equals the distance between the second grating and the detector, the trajectories refocus in the plane of the detector. Instead of a single spot as in the case of single slits, one observes a fringe pattern that has the same periodicity as the gratings. The position of the fringe pattern is still described by equation 2.1. This configuration is known as a moiré deflectometer, which can be seen as the generalisation of the single slit configuration. The deflection Δy depends on the particles' time-of-flight, thus the moiré deflectometer is a dispersive device. In an experiment one can either measure the total shift Δy, for which the position of the undeflected fringe pattern must be known, or one makes use of the dispersion and measures the fringe position as a function of the time-of-flight. The moiré deflectometer has two main advantages. First of all, it is universal, as one can use it for any particle species one can build a detector for. Secondly, its use does not require a collimated beam, so it suits the divergent antihydrogen beam the AEgIS experiment intends to create.

A pivotal question does, however, remain: is it adequate to describe the motion of the particles as classical trajectories or must their wave-like behaviour also be accounted for? This fundamental question will be of central importance to the work presented and is reviewed on different levels throughout this elaboration. A first estimation [38] of this limit between the

classical and the wave regime can be derived from the grating equation,

$$d \sin(\phi_n) = n\lambda \ , \tag{2.2}$$

specifying the angle ϕ_n of the nth diffraction order of a plane wave with wavelength λ, which impinges on a grating with periodicity d. The spatial separation of neighbouring diffraction orders after the distance L when the diffracted beams arrive on the second grating is approximately

$$L\frac{\lambda}{d} = L \sin(\phi_1) \approx L\,\phi_1 \ll d \ . \tag{2.3}$$

If this separation is much smaller than the grating period d, one can assume, that the wave-like character is negligible. Thus, one can describe the experiment with classical paths if the condition

$$L \ll \frac{d^2}{\lambda} \tag{2.4}$$

is fulfilled. It is interesting to note that the characteristic length $L_\mathrm{T} = d^2/\lambda$ is known as the Talbot length, the relevance of which is further examined in the following section.

2.2. Talbot Effect

In 1836, H. F. Talbot was the first [73] to observe an effect that was later named after him, with a grating fabricated by Fraunhofer. He illuminated this grating with a ray of sunlight coming from a point-like source and studied the grating with a lens[2]. He was surprised to observe coloured fringes, which were parallel to the grating's slits. When he increased the distance between grating and lens, the fringes' colour changed from red over green to blue and than back to red. He increased the distance up to a foot and still observed fringes of high visibility, even though the grating was far outside the focal point of the grating. An analytical description for this effect was not found until Lord Rayleigh [74] repeated the experiment in 1881, but Talbot already correctly suspected that the maximal distance at which one can observe fringes depends on the spatial extent of the light source and thus how close the light source comes to a mathematical point source. Figure 2.2a illustrates an example of the Talbot effect. A plane wave with wavelength λ impinges on a single grating with periodicity d. The intensity field behind the grating depicts a characteristic structure that repeats itself and is known as a 'Talbot carpet'[3]. At integer multiples of the so-called Talbot length

$$L_\mathrm{T} = \frac{d^2}{\lambda} \tag{2.5}$$

one observes a self-image or a 'rephasing' of the grating. A detector with sufficient spatial resolution placed on one of these distinct distances records a fringe pattern with the periodicity

[2]The author strongly discourage the reader from looking into sunlight with a magnifying glass.
[3]The web page of the journal 'nature physics' uses a blue Talbot carpet as a background of their title line.

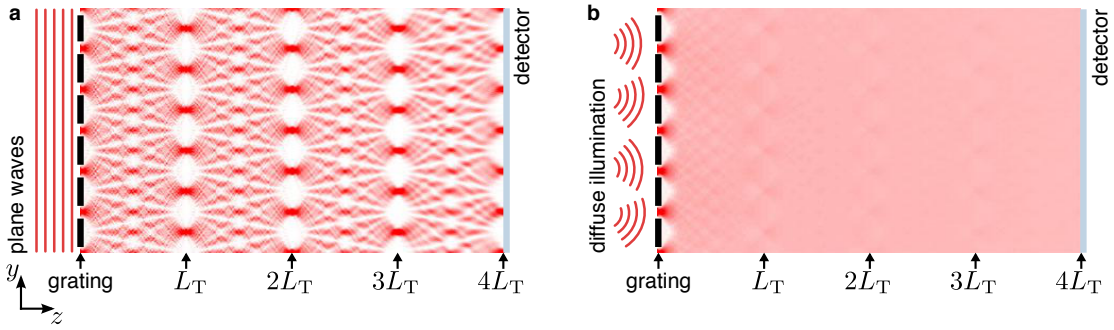

Figure 2.2.: (a) Illumination of a periodic structure such as a grating with plane waves leads to the Talbot effect, which denotes that the self-image of the grating rephases at integer multiple of a distinct length – called Talbot length $L_T = d^2/\lambda$. A detector placed on one of these self-images records a fringe pattern with high visibility. (b) Coherent illumination is a crucial requirement for the observation of the Talbot effect. A diffuse light source causes the so-called 'Talbot carpet' to smear out.

of the gratings. Between these full self-images one notices patterns with higher periodicities. This fractional Talbot effect has been subject to numerous publications and is connected to interesting fields such as number theory and fractals [67], but is of limited relevance for the work presented and consequently omitted in the following. It is important to realise that coherent illumination is a crucial requirement to observe self-images. The use of a monochromatic but diffuse light source as shown in figure 2.2b does not lead to structure in the intensity field.

The Talbot effect is a well-established phenomenon. Several approaches exist [64, 69, 71, 76, 77] to derive the effect and it has been experimentally observed with light [76, 77], electrons [78], atoms [36, 37, 79], plasmons [80–82] and heavy molecules [36, 56, 83]. The following derivation [71, 84, 85] is based on the plane-wave decomposition also known as the angular spectrum. It provides intuitive access to key features of the Talbot effect and efficient means to compute intensity fields as shown in figure 2.2. This approach allows to compute the field u at an arbitrary position $z > 0$ if the field at the position $z = 0$, where the grating is placed, is known. The Fourier transformation of a given scalar field $u(y, z = 0)$ is

$$\tilde{u}(k_y) = \mathcal{F}_y\{u(y, z = 0)\} = \int \mathrm{d}y\, u(y, z = 0) e^{-ik_y y} \,, \tag{2.6}$$

which is also known as the angular spectrum. The reverse Fourier transformation is given by

$$u(y, z = 0) = \mathcal{F}_{k_y}^{-1}\{\tilde{u}(k_y)\} = \frac{1}{2\pi} \int \mathrm{d}k_y\, \tilde{u}(k_y) e^{ik_y y} \tag{2.7}$$

and results again in the field at $z = 0$. Thus the field in the plane of the grating is a superposition of plane waves into which it can be decomposed. Each plane wave propagates freely in space. Because of the dispersion relation $\vec{k}^2 = k^2 = (2\pi/\lambda)^2$, the components

of $k = [k_y, k_z]$ are not independent but connected by

$$k_z = \pm\sqrt{\left(\frac{2\pi}{\lambda}\right)^2 - k_y^2}\ , \tag{2.8}$$

where the positive k_z describe the waves propagating in the positive z direction. Each wave accumulates on the distance between the grating and the observational plane z an additional phase of $e^{ik_z z}$. With the use of equation 2.8, the field in this plane follows as

$$\begin{aligned} u(y,z) &= \frac{1}{2\pi}\int \mathrm{d}k_y\, \tilde{u}(k_y) e^{ik_z z} e^{ik_y y} \\ &= \frac{1}{2\pi}\int \mathrm{d}k_y\, \tilde{u}(k_y) e^{iz\sqrt{(2\pi/\lambda)^2 - k_y^2}} e^{ik_y y}\ . \end{aligned} \tag{2.9}$$

If one introduces the propagator $\mathcal{P}_{k_y}(z) := \exp(iz\sqrt{(2\pi/\lambda)^2 - k_y^2})$, this can be written as

$$u(y,z) = \mathcal{F}_{k_y}^{-1}\{\mathcal{F}_y\{u(y,0)\}\cdot \mathcal{P}_{k_y}(z)\}\ , \tag{2.10}$$

which is known as the plane-wave decomposition (pwd). Note that no approximation was required so far, so that the pwd solves the wave equation $\Delta u = -k^2 u$:

$$\Delta u = \int \mathrm{d}k_y\, \tilde{u}(k_y) \Delta e^{ik_y y + ik_z z} = \left((ik_y)^2 + (ik_z)^2\right) u = -k^2 u\ . \tag{2.11}$$

Depicted intensity fields throughout this work, such as figure 2.2, are computed by numerically evaluating equation 2.10. Diffuse illuminations are simulated by summation of the intensity fields resulting from plane waves of varying incident angle θ

$$I = \sum_\theta I_\theta \quad \text{with} \quad I_\theta = u_\theta^* u_\theta\ . \tag{2.12}$$

The plane wave decomposition has the advantage that one can compute fields resulting from the illumination of finite gratings – which is of importance later on. For now, the introduction of a grating of infinite length provides an analytic form of the Talbot effect. Such an infinitely long grating with grating vector $k_d = 2\pi/d$ can be represented by its Fourier series

$$f(y) = \sum_{n=\infty}^{\infty} c_n\, e^{ink_d y} = \sum_{n=\infty}^{\infty} c_n\, e^{ik_n y}\ , \tag{2.13}$$

with $k_n = n \cdot k_d$ and the Fourier coefficients

$$c_n = \frac{1}{d}\int_{\frac{d}{2}}^{\frac{d}{2}} \mathrm{d}y\, f(y)\, e^{-ik_n y}\ . \tag{2.14}$$

The grating is assumed to be infinitely thin[4] and placed at $z = 0$. If a plane wave $u(y, z) = e^{i(k_y y + k_z z)}$ impinges on the grating from one side (denoted 0^-), the field on the other side of the grating (denoted 0^+) follows as

$$u(y, 0^+) = u(y, 0^-) \cdot f(y) = \sum_{n=\infty}^{\infty} c_n \, e^{i(k_y + k_n)y} \ . \tag{2.15}$$

The field behind the grating consists of a series of plane waves with wave vectors $k'_n = k_y + k_n$ corresponding to different angles of propagation. These are the well-known diffraction angles that were given by the grating equation

$$d\,(\sin(\phi_n) - \sin(\phi)) = n\lambda \ , \tag{2.16}$$

where ϕ denotes the incident angle of the incoming plane wave. Beginning with the field behind the plane of the grating, one can determine the propagation in two steps using the plane wave decomposition. Firstly, with the use of $\int \mathrm{d}y \exp(iky) = \delta(y)$, the Fourier transformation of the field behind the grating is

$$\begin{aligned} \tilde{u}(k_y) &= \int \mathrm{d}y \, u(y, 0^+) e^{-ik_y y} = \sum_{n=\infty}^{\infty} c_n \int \mathrm{d}y \, e^{i(k'_n y - k_y y)} \\ &= \sum_{n=\infty}^{\infty} c_n \, \delta\left(k'_n - k_y\right) \ , \end{aligned} \tag{2.17}$$

which is then multiplied with the propagator $\mathcal{P}_{k_y}(z) = iz\sqrt{k^2 - k_y^2}$ followed by the reverse Fourier transformation

$$\begin{aligned} u(y, z) &= \frac{1}{2\pi} \int \mathrm{d}k_y \, \tilde{u}(k_y) \, e^{iz\sqrt{k^2 - k_y^2}} e^{ik_y y} \\ &= \frac{1}{2\pi} \sum_{n=\infty}^{\infty} c_n \int \mathrm{d}k_y \, \delta\left(k'_n - k_y\right) \, e^{iz\sqrt{k^2 - k_y^2}} e^{ik_y y} \\ &= \sum_{n=\infty}^{\infty} c_n \, e^{iz\sqrt{k^2 - k'^2_n}} e^{ik'_n y} \ , \end{aligned} \tag{2.18}$$

where the last step uses the convention $\int \mathrm{d}k \, \delta(k) = 2\pi$. The square root in the exponent is developed to first order to

$$\sqrt{k^2 - k'^2_n} \approx k - \frac{k'^2_n}{2k} \pm \dots \ , \tag{2.19}$$

which is known as the paraxial approximation. A plane wave impinging perpendicular onto

[4] Note that the grating causes a discontinuity in the field.

the grating corresponds to $k_y = 0$, which leads to $k'_n = k_n = nk_d$. The field follows as

$$\begin{aligned} u(y,z) &\approx \sum_{n=\infty}^{\infty} c_n e^{ikz} e^{-i\pi n^2 \frac{\lambda}{d^2} z} e^{ik_n y} \\ &= e^{ikz} \sum_{n=\infty}^{\infty} c_n e^{ik_n y} e^{-i\pi \frac{n^2}{L_\mathrm{T}} z} \ , \end{aligned} \tag{2.20}$$

where the Talbot length (equation 2.5) $L_\mathrm{T} = d^2/\lambda$ is inserted in the last step. This result is notable as it only differs from the field behind the grating by the additional phase factors $\exp(ikz)$ and $\exp\left(-i\pi \frac{n^2}{L_\mathrm{T}} z\right)$, of which the former can be neglected as only the intensity $I = u^* u$ is experimentally accessible. It can be directly seen that, if the distance z equals an even integer of the Talbot length, the last phase factor becomes 1, leading to

$$u(y, z = 2mL_\mathrm{T}) \approx u(y, z = 0) \quad \text{for} \quad m \in \mathbb{N} \ . \tag{2.21}$$

At these distinct positions one observes the same intensity field as directly behind the grating, which is the reason why the observed patterns are called self-images. In literature, one therefore often finds in literature an alternative definition of the Talbot length, $L'_\mathrm{T} = 2d^2/\lambda$. Figure 2.2 depicts additional self-images, which are shifted by half a grating period, at distances which are uneven integer multiples of the Talbot length L_T. This can be seen following

$$\exp(-i\pi \frac{n^2}{L_\mathrm{T}} z) = \exp(-2\pi i\, n^2 m) \cdot \exp(-i\pi\, n^2) = 1 \cdot \exp(-i\pi\, n) \ , \tag{2.22}$$

as an uneven number squared results in an uneven number. This leads to

$$\begin{aligned} u(y, z = mL_\mathrm{T}) &\approx \sum_{n=\infty}^{\infty} c_n e^{ik_n y} e^{-i\pi\, n} = \sum_{n=\infty}^{\infty} c_n e^{i(\frac{2\pi}{d} n y - \pi n)} \\ &= \sum_{n=\infty}^{\infty} c_n e^{(ik_n (y - d/2))} = u(y - d/2, z = 0) \ . \end{aligned} \tag{2.23}$$

2.3. Talbot-Lau Interferometry

The Talbot effect described in the previous section requires coherent illumination such as plane waves. Ernst Lau described [75] in 1948 how a similar effect can be observed with a diffuse wave source using an additional grating. His argument is illustrated in figure 2.3, which shows a close-up of two gratings with periodicity d that are separated by the distance L. The red lines represent adjacent paths of which the common origin is a single slit of the first grating. One looks for the grating separation L for which the phase difference between the neighbouring slits B and D is equal to one wavelength λ. The black curve identifies points of identical phase. The tangent in point C divides BD into two equal parts for a small angle α, from which follows that $BE = 2\lambda$. The angle $\sphericalangle BDE$ is equal to α. With $\tan(\alpha) = d/L$ and $\sin(\alpha) = 2\lambda/d$ follows for a small angle α

$$\frac{d}{L} = \frac{2\lambda}{d} \rightarrow L = \frac{d^2}{2\lambda} = \frac{L_\mathrm{T}}{2} \ . \tag{2.24}$$

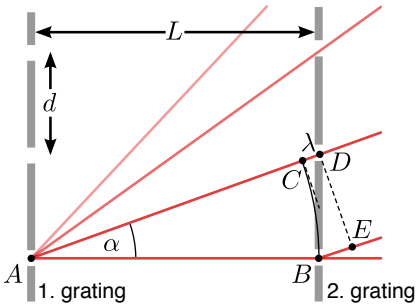

Figure 2.3.: Neighbouring paths in a Talbot-Lau interferometer. Following the argument of Ernst Lau [75], the resulting phase difference between neighbouring slits of the second grating equals the wavelength λ if the grating separation L corresponds to the half Talbot length. The second grating seems to be illuminated by a plane wave and the intensity field behind the second gratings is similar to the one observed in the Talbot effect.

This corresponds to a half Talbot length. In this configuration, the phase difference between neighbouring slits of the second grating corresponds to a full wavelength. Consequently, the second grating seems to be illuminated by a plane wave, which leads to a result behind the second grating that is comparable to the case where a single grating is illuminated with a plane wave. It is therefore the first grating that generates the spatial coherence. The argument

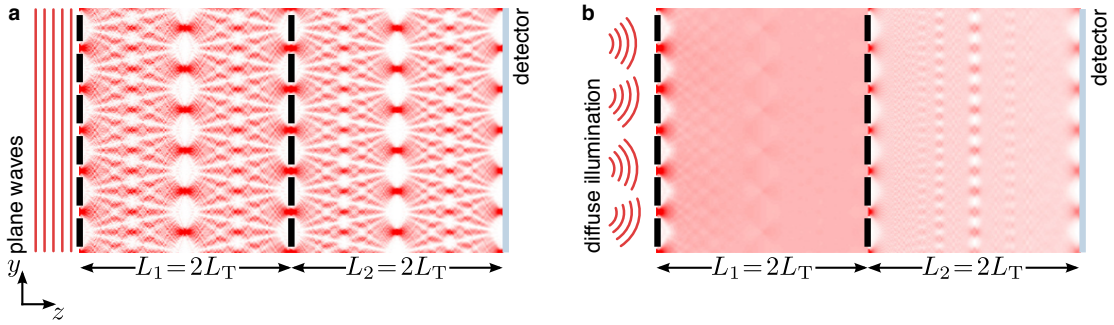

Figure 2.4.: (a) A Talbot-Lau interferometer requires a second grating. The distance between the two gratings and between the second grating and the observational plane equals an integer multiple of the Talbot length. For plane waves one observes the same Talbot carpet but in contrast to the simple Talbot effect, the fringe pattern observed on the detector remains when using a diffuse illumination as shown in (b). The reason is the spatial coherence generated by the first grating. For better perceptibility, the intensity of the light field between second grating and the detector is divided by the open fraction η to compensate for the intensity loss at the passage of the second grating.

of Lau provides an intuitive explanation of how near-field interferometry, such as the Talbot effect, can be realised with uncollimated sources. This is of special interest when working with matter waves, where Talbot-Lau interferometers make efficient use of uncollimated sources. In a configuration commonly used in many experiments the two gratings and the detector

are equidistant and the separation corresponds to an integer multiple of the Talbot length:

$$L_1 = L_2 = nL_T \quad \text{for} \quad n \in \mathbb{N} \tag{2.25}$$

Figure 2.4 depicts an example of a Talbot-Lau interferometer where the grating separation is set to twice the Talbot length. For an illumination with plane waves as depicted in (a), the intensity field is identical to the simple Talbot effect. If illuminated with a diffuse wave source as shown in (b), the majority of the field's features vanish. But in contrast to the simple Talbot effect (compare to figure 2.2), a fringe pattern of high visibility remains detectable in the observational plane. The following section provides a detailed analytical description of Talbot-Lau interferometry using the Wigner description of a stationary beam. Furthermore it reveals a direct connection to moiré deflectometry from which two important conclusions can be drawn.

2.4. Wigner Function and Classic Phase Space Representation

Talbot-Lau interferometry is a well-established field. A variety of approaches describe this near-field interferometer in great detail [65, 66, 69, 71, 73, 75–77]. This section closely follows a derivation outlined by Hornberger et al. [64], which uses the Wigner representation [86]. Furthermore, the moiré deflectometer is revised in the analogous representation in classic phase space in section 2.4.2. The similarity of these formal approaches allows a direct comparison between the Talbot-Lau interferometer and the moiré deflectometer. The results of these sections are simple expressions for the visibility and the phase of the signal of these two types of devices.

2.4.1. Talbot-Lau Interferometer in Wigner Representation

The overall experimental geometry is maintained and corresponds to the one described in the previous sections. The particles of a beam propagate in positive z direction with momentum p_z, which is assumed to be much larger than the transversal momenta. The consequence of this assumption is that the longitudinal and the transverse component of the wave function can be separated. $\psi_0(\mathbf{r})$ denotes the transverse component of the initial state, so $\mathbf{r} = (x, y)$ are two-dimensional coordinates that lie in the plane of the gratings. The Wigner function is a quasiprobability distribution. It is comparable to a probability distribution $f(\mathbf{r}, \mathbf{p})$ of a classical system described in phase space, but does not fulfil all its properties due to Heisenberg's uncertainty principle [87], which limits to what extent one can simultaneously measure a particle's position $\mathbf{r}$ and momentum $\mathbf{p}$. The Wigner function [86] is defined as

$$w(\mathbf{r}, \mathbf{p}) = \frac{1}{2\pi\hbar} \int \mathrm{d}\boldsymbol{\Delta}\, e^{\frac{i\mathbf{p}\boldsymbol{\Delta}}{\hbar}}\, \rho\left(\mathbf{r} - \frac{\boldsymbol{\Delta}}{2}, \mathbf{r} + \frac{\boldsymbol{\Delta}}{2}\right) \tag{2.26}$$

and represents the Fourier transformation of the density matrix[5]

$$\rho(\mathbf{r},\mathbf{r}') = \int \mathrm{d}\mu\, g(\mu)\, \psi_\mu(\mathbf{r})\, \psi_\mu^*(\mathbf{r}') \;, \tag{2.27}$$

where $\Delta = \mathbf{r} - \mathbf{r}'$ denotes the so called two-point separation. One requires two transformations, which are alternately applied to the Wigner function to determine the signal at the end of the interferometer. The first step is the free evolution of the Wigner function $w(\mathbf{r},\mathbf{p})$ as it propagates the distance L from one grating to the next one. The other transformation describes the changes that occur to the Wigner function at the passage of a grating. The derivation is structured as follows: First, the free evolution and the passage through a grating are examined. These transformations are then applied to the beam as it propagates through the interferometer. With explicit expressions for the gratings, one can finally derive a formula for the signal of such a device.

Free Evolution of the Wigner Function

With the free evolution of the state [64]

$$\psi(\mathbf{r}) = \frac{p_z}{2\pi i\,\hbar L} e^{ip_z L/\hbar} \int \mathrm{d}\mathbf{r}_0 \exp\left(i\frac{p_z}{\hbar}\frac{|\mathbf{r}-\mathbf{r}_0|^2}{2L}\right)\psi_0(\mathbf{r}_0) + O\left(\frac{\mathbf{r}}{L^2}\right) \tag{2.28}$$

the density matrix evolves like

$$\begin{aligned}
\rho(\mathbf{r},\mathbf{r}') &= \int \mathrm{d}\mu\, g(\mu)\, \psi_\mu(\mathbf{r})\, \psi_\mu^*(\mathbf{r}') \\
&= \left(\frac{p_z}{2\pi\,\hbar L}\right)^2 \int \mathrm{d}\mu\, \mathrm{d}\mathbf{r}_0\, \mathrm{d}\mathbf{r'}_0\, g(\mu) \exp\left(i\frac{p_z}{\hbar}\frac{|\mathbf{r}-\mathbf{r}_0|^2}{2L}\right)\psi_0(\mathbf{r}_0)\cdot \\
&\quad \exp\left(-i\frac{p_z}{\hbar}\frac{|\mathbf{r}'-\mathbf{r'}_0|^2}{2L}\right)\psi_0^*(\mathbf{r'}_0) \\
&= \left(\frac{p_z}{2\pi\,\hbar L}\right)^2 \int \mathrm{d}\mathbf{r}_0\, \mathrm{d}\mathbf{r'}_0\, \exp\left(i\frac{p_z}{\hbar}\frac{|\mathbf{r}-\mathbf{r}_0|^2 - |\mathbf{r}'-\mathbf{r'}_0|^2}{2L}\right) \int \mathrm{d}\mu\, g(\mu)\psi_0(\mathbf{r}_0)\psi_0^*(\mathbf{r'}_0) \\
&= \left(\frac{p_z}{2\pi\,\hbar L}\right)^2 \int \mathrm{d}\mathbf{r}_0\, \mathrm{d}\mathbf{r'}_0\, \exp\left(i\frac{p_z}{\hbar}\frac{|\mathbf{r}-\mathbf{r}_0|^2 - |\mathbf{r}'-\mathbf{r'}_0|^2}{2L}\right) \rho_0(\mathbf{r}_0,\mathbf{r'}_0) \;.
\end{aligned} \tag{2.29}$$

This is used [64] to determine the free evolution of the Wigner function after the distance L

$$\begin{aligned}
w_L(\mathbf{r},\mathbf{p}) &= \frac{1}{(2\pi\hbar)^2}\frac{p_z^2}{(2\pi\hbar)^2 L^2} \int \mathrm{d}\boldsymbol{\Delta} e^{\frac{i\,\mathbf{p}\,\boldsymbol{\Delta}}{\hbar}} \int \mathrm{d}\mathbf{r}_0\mathbf{r}'_0 \exp\left(i\frac{p_z}{\hbar}\frac{\left|\mathbf{r}-\frac{\boldsymbol{\Delta}}{2}-\mathbf{r}_0\right|^2 - \left|\mathbf{r}-\frac{\boldsymbol{\Delta}}{2}-\mathbf{r}'_0\right|^2}{2L}\right) \\
&= \frac{1}{(2\pi\hbar)^2}\int \mathrm{d}\boldsymbol{\Delta} e^{\frac{i\,\mathbf{p}\,\boldsymbol{\Delta}}{\hbar}} \rho_0\left(\mathbf{r}-\frac{L}{p_z}\mathbf{p}, \mathbf{r}-\frac{L}{p_z}\mathbf{p}+\frac{\boldsymbol{\Delta}}{2}\right) = w_0\left(\mathbf{r}-\frac{L}{p_z}\mathbf{p},\mathbf{p}\right) \;.
\end{aligned} \tag{2.30}$$

The important result here is that in the Wigner representation the free evolution becomes a simple expression. The propagation of the distance L causes a position shift of $\frac{L}{p_z}\mathbf{p}$ in the Wigner function.

[5] Note that $\int \mathrm{d}\mu\, g(\mu) = 1$.

Wigner Function's Passage through a Grating

The second transformation in the Wigner representation one requires is the passage of the beam through a grating. A grating $t(\mathbf{r})$ with $|t(\mathbf{r})|^2 < 1$ results in a modulation of the transverse wave function $\psi_i(\mathbf{r})$ impinging on a grating, so the wave function $\psi_{i+1}(\mathbf{r})$ behind the grating is given by $\psi_{i+1}(\mathbf{r}) = t(\mathbf{r})\,\psi_i(\mathbf{r})$. With the definition of the Wigner function (equation 2.26) and the density matrix (equation 2.27), the Wigner function behind the grating follows as

$$w_{i+1}(\mathbf{r},\mathbf{p}) = \int \mathrm{d}\boldsymbol{\Delta}\, e^{\frac{i\,\mathbf{p}\,\boldsymbol{\Delta}}{\hbar}}\, t\left(\mathbf{r}-\frac{\Delta}{2}\right)\, t^*\left(\mathbf{r}+\frac{\Delta}{2}\right)\, \rho_i\left(\mathbf{r}-\frac{\Delta}{2},\mathbf{r}+\frac{\Delta}{2}\right)\ . \tag{2.31}$$

This term represents a Fourier transformation of a product. Thus, equation 2.31 can be rewritten as the convolution

$$w_{i+1}(\mathbf{r},\mathbf{p}) = \int \mathrm{d}\mathbf{q}\, T(\mathbf{r},\mathbf{q})\, w_i(\mathbf{r},\mathbf{p}-\mathbf{q})\ , \tag{2.32}$$

where the convolution kernel $T(\mathbf{r},\mathbf{p})$ represents the grating

$$T(\mathbf{r},\mathbf{p}) = \frac{1}{(2\pi\hbar)^2}\int \mathrm{d}\Delta\, e^{\frac{i\,\mathbf{p}\,\boldsymbol{\Delta}}{\hbar}}\, t\left(\mathbf{r}-\frac{\Delta}{2}\right)\, t^*\left(\mathbf{r}+\frac{\Delta}{2}\right)\ . \tag{2.33}$$

Propagation through the Interferometer

Step-by-step, one can now proceed along the individual elements of the Talbot-Lau interferometer. Starting with an initial Wigner function $w_0(\mathbf{r},\mathbf{p}) = 1$, the passage through the first grating (see equation 2.32) yields

$$w_1(\mathbf{r},\mathbf{p}) = |t_1(\mathbf{r})|^2\ . \tag{2.34}$$

The free evolution given by equation 2.30 between the first and the second grating, which are separated by the distance L, leads to

$$w_2(\mathbf{r},\mathbf{p}) = w_1\left(\mathbf{r}-\frac{L}{p_z}\mathbf{p},\mathbf{p}\right) = \left|t_1\left(\mathbf{r}-\frac{L}{p_z}\mathbf{p}\right)\right|^2\ . \tag{2.35}$$

Here, the beam impinges on the second grating T_2, which in turn yields

$$\begin{aligned} w_3(\mathbf{r},\mathbf{p}) &= \int \mathrm{d}\mathbf{q}\, T_2(\mathbf{r},\mathbf{p})\, w_2(\mathbf{r},\mathbf{p}-\mathbf{q}) \\ &= \int \mathrm{d}\mathbf{q}\, \left|t_1\left(\mathbf{r}-\frac{L}{p_z}(\mathbf{p}-\mathbf{q})\right)\right|^2 \cdot T_2(\mathbf{r},\mathbf{q})\ . \end{aligned} \tag{2.36}$$

This is followed by another free evolution of the distance L between the second grating and the observational plane, which finally leads to

$$\begin{aligned} w_4(\mathbf{r},\mathbf{p}) &= w_3\left(\mathbf{r}-\frac{L}{p_z}\mathbf{p},\mathbf{p}\right) \\ &= \int \mathrm{d}\mathbf{q}\left|t_1\left(\mathbf{r}-\frac{L}{p_z}\mathbf{p}-\frac{L}{p_z}(\mathbf{p}-\mathbf{q})\right)\right|^2 \cdot T_2\left(\mathbf{r}-\frac{L}{p_z}\mathbf{p},\mathbf{q}\right) \\ &= \int \mathrm{d}\mathbf{q},\left|t_1\left(\mathbf{r}-2\frac{\mathbf{p}}{p_z}L+\frac{\mathbf{q}}{p_z}L\right)\right|^2 \cdot T_2\left(\mathbf{r}-\frac{\mathbf{p}}{p_z}L,\mathbf{q}\right)\ . \end{aligned} \tag{2.37}$$

The Wigner function $w_4(\mathbf{r},\mathbf{p})$ represents the state in the observational plane. One needs to integrate over the momentum variable of $w_4(\mathbf{r},\mathbf{p})$ to retrieve the density modulation or fringe pattern recorded in this plane. In order to proceed, one requires explicit expressions for the coefficients of the first and second grating given by $|t_1(\mathbf{r})|^2$ and $T_2(\mathbf{r},\mathbf{p})$, respectively. These are determined in the following. For simplicity, the discussion is limited to the dimension, which is parallel to the grating vector k_d, thus the position y and momentum $p = p_y$.

Fourier Coefficients of the Gratings

As previously discussed (see equation 2.13), the infinite gratings $t_i(y)$ can be represented by their Fourier series

$$t_i(y) = \sum_{n\in\mathbb{Z}} a_n \exp\left(ink_d y\right) \tag{2.38}$$

with the grating vector $k_d = 2\pi/d$. The three gratings $t_i(y)$ are restricted to the case of real amplitude gratings, thus they exhibit transparent slits with the open fraction η but are otherwise opaque as seen in figure 2.5. With equation 2.14, the Fourier coefficients of these

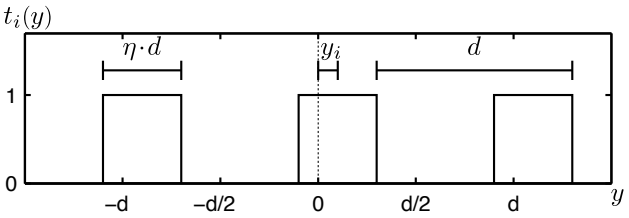

Figure 2.5.: Geometry of the gratings represented by $t_i(y)$ with open fraction η, grating period d and position y_i.

gratings, which have a rectangular shape, are

$$\begin{aligned} a_n &= \frac{1}{d}\int_{-\frac{d}{2}}^{\frac{d}{2}} \mathrm{d}y\, t_1(y) e^{-ink_d y} = \frac{1}{d}\int_{-\frac{\eta}{2}+y_\mathrm{i}}^{\frac{\eta}{2}+y_\mathrm{i}} \mathrm{d}y\, e^{-ink_d y} \\ &= \frac{i}{2\pi n}\left(e^{-ink_d\left(\frac{\eta}{2}+y_\mathrm{i}\right)} - e^{-ink_d\left(-\frac{\eta}{2}+y_\mathrm{i}\right)}\right) \\ &= \eta\,\mathrm{sinc}(n\,\eta)\cdot e^{-ink_d y_\mathrm{i}} = a_n' \cdot e^{-ink_d y_\mathrm{i}}\ , \end{aligned} \tag{2.39}$$

where the cardinal sine is given by $\mathrm{sinc}(b) = {}^{\sin(\pi\, b)}/_{\pi\, b}$. The position y_i of the ith grating denotes the shift relative to the position on which a slit is centred on zero (see figure 2.5), thus a'_n (with inverted comma) are the coefficients of the grating that is centred on zero. This notation is maintained throughout this section. The square of the absolute value of $t_1(y)$ yields

$$\begin{aligned}
|t_1(y)|^2 = t_1(y)\, t_1^*(y) &= \left(\sum_{j\,\in\,\mathbb{Z}} a_j \exp\left(ijk_d y\right)\right) \cdot \left(\sum_{h\,\in\,\mathbb{Z}} a_h^* \exp\left(-ihk_d y\right)\right) \\
&= \sum_{j,h\,\in\,\mathbb{Z}} a_j a_h^* \exp\left(i(j-h)k_d y\right) \overset{l=j-h}{=} \left(\sum_{j,l\,\in\,\mathbb{Z}} a_j a_{j-l}^* \exp\left(ilk_d y\right)\right) \\
&= \sum_{l\,\in\,\mathbb{Z}} A_l \, \exp(ilk_d y) \quad \text{with} \quad A_l = \sum_{j\,\in\,\mathbb{Z}} a_j a_{j-l}^* \\
&= \sum_{l\,\in\,\mathbb{Z}} A'_l \, \exp(ilk_d (y+y_1)) \quad \text{with} \quad A'_l = \sum_{j\,\in\,\mathbb{Z}} a'_j \, a'^*_{j-l} \; . \qquad (2.40)
\end{aligned}$$

Using equation 2.33 and the same rearrangement of the sums as for the first grating, the second grating is given by

$$\begin{aligned}
T_2(y,p) &= \sum_{l,j\in\mathbb{Z}} b_j b_{j-l}^* \exp\left(ilk_d y\right) \, \delta\left(p - \hbar\pi \frac{2j-l}{d}\right) \\
&= \sum_{l,j\in\mathbb{Z}} b'_j \, b'^*_{j-l} \exp\left(ilk_d (y+y_2)\right) \, \delta\left(p - \hbar\pi \frac{2j-l}{d}\right) \; . \qquad (2.41)
\end{aligned}$$

Detectable Signal of a Talbot-Lau Interferometer

With expressions for $|t_1(y)|^2$ and $T_2(y,p)$, one can proceed to evaluate the Wigner function $w_4(y,p)$ in the observational plane. It follows by evaluating the integral in equation 2.37

and rearranging the arguments of the phase factors.

$$\begin{aligned}
w_4(y,p) &= \int \mathrm{d}q \left| t_1\left(y - 2\frac{p}{p_z}L + \frac{q}{p_z}L\right)\right|^2 T\left(y - \frac{p}{p_z}L, q\right) \\
&= \int \mathrm{d}q \left(\sum_{l\in\mathbb{Z}} A_l \exp\left(ilk_d\left(y - 2\frac{p}{p_z}L + \frac{q}{p_z}L\right)\right)\right) \cdot \\
&\quad \sum_{j,m\in\mathbb{Z}} b_m b^*_{m-j} \exp\left(ijk_d(y - \frac{p}{p_z}L)\right) \delta\left(q - \hbar\pi\frac{2m-j}{d}\right) \\
&= \sum_{l,j,m\in\mathbb{Z}} A_l\, b_m b^*_{m-j} \exp\left(ilk_d\left(y - 2\frac{p}{p_z}L + \frac{\hbar\pi}{p_z}\frac{2m-j}{d}L\right)\right) \cdot \\
&\quad \exp\left(ijk_d\left(y - \frac{p}{p_z}L\right)\right) \\
&= \sum_{l,j,m\in\mathbb{Z}} A_l\, b_m b^*_{m-j} \exp\left(ik_d\,(l+j)\,y - ik_d(2l+j)\frac{p}{p_z}L\right) \cdot \\
&\quad \exp\left(i\pi\, l\,(2m-j)\frac{L}{L_T}\right)
\end{aligned} \tag{2.42}$$

In the last step, the Talbot length $L_\mathrm{T} = d^2/\lambda = d^2 p_z/h$ is introduced. In order to determine the density modulation, which can be detected with a spatially resolving detector placed in the observational plane, one simply needs to integrate over the transversal momentum p:

$$\begin{aligned}
w(y) &= \int \mathrm{d}p\, w_4(y,p) \\
&= \sum_{l,j,m\in\mathbb{Z}} A_l\, b_m b^*_{m-j} \exp\left(i\pi l(2m-j)\frac{L}{L_T}\right) \exp(ik_d(l+j)y) \int \mathrm{d}p \exp\left(-ik_d(2l+j)\frac{p}{p_z}L\right) \\
&\propto \sum_{l,m\in\mathbb{Z}} A_l\, b_m b^*_{m+2l} \exp\left(i\pi l(2m+2l)\frac{L}{L_T}\right) \exp(ik_d(l-2l)y) \\
&= \sum_{l\in\mathbb{Z}} A_l\, B^{(\mathrm{T})}_{2l} \exp(ik_d l y)
\end{aligned} \tag{2.43}$$

with

$$B^{(\mathrm{T})}_j = \sum_{m\in\mathbb{Z}} b_m b^*_{m-j} \exp\left(i\pi\frac{j^2-2mj}{2}\frac{L}{L_T}\right)\ . \tag{2.44}$$

Note that due to the integral over p in equation 2.43, the only remaining summands are the ones with $j = -2l$. Equation 2.43 depicts that in the observational plane, one can observe a fringe pattern with the same periodicity as the gratings. The coefficients $B^{(\mathrm{T})}_j$ express the influence of the second grating. It turns out that it is indeed the description of the second grating that differs in the wave regime from the classical description. The first grating solely

generates spatial coherence, but the second grating redirects momentum due to diffraction, which is absent in the classical regime. The coefficients $B_j^{(\mathrm{T})}$ of the Talbot-Lau interferometer are therefore marked with a (T) to distinguish them from the classical coefficients $B_j^{(\mathrm{C})}$, which are introduced further down in section 2.4.2. The position of the second grating y_2 influences the coefficients $B_j^{(\mathrm{T})}$ through an additional phase factor

$$\begin{aligned} B_{2l}^{(\mathrm{T})} &= \sum_{m\,\in\,\mathbb{Z}} b_m b_{m-2l}^{*} \exp\left(2\pi i \left(l^2 - ml\right) \frac{L}{L_\mathrm{T}}\right) \\ &= \sum_{m\,\in\,\mathbb{Z}} b'_m b'^{*}_{m-2l} \exp\left(2\pi i \left(l^2 - ml\right) \frac{L}{L_\mathrm{T}}\right) \exp\left(-k_d i l\, 2y_2\right) \\ &= B'^{(\mathrm{T})}_{2l} \exp\left(-k_d i l\, 2y_2\right) \ . \end{aligned} \tag{2.45}$$

The comparison with equation 2.40 shows that a displacement of the second grating by Δy_2 shifts the observed pattern by twice the distance and in opposite direction compared to an equal displacement of the first grating by Δy_1. The pattern $w(y)$ can be directly observed with a detector whose spatial resolution is smaller than the grating period d. An experimental realisation of this approach is presented in chapter 3. In many experiments where the fringe pattern cannot be directly resolved, a third grating (identical to the other two) can be placed in the observational plane to probe or to scan the fringe pattern. A detector with no spatial resolution behind the third grating measures only the spatial integral of the flux, thus the technological requirements for this detector are significantly reduced. Naturally, the flux measured by this detector is reduced as a portion of the particles hit the last grating. But this limitation of statistics can be circumvented with the approach presented in chapter 4. The following derivation includes the use of a third grating, which leads to the signal

$$\begin{aligned} S &= \int \mathrm{d}y\, \mathrm{d}p\, \mathrm{d}q\, w_4(y, p-q)\, T(y,q) \\ &= \int \mathrm{d}y\, w(y)\, |t_3(y)|^2 \ . \end{aligned} \tag{2.46}$$

The notation is maintained: the coefficients of the third grating are denoted C_l and its position is labelled y_3. This finally leads to the signal of the three-grating Talbot-Lau interferometer:

$$\begin{aligned} S\left(y_1, y_2, y_3\right) &\propto \sum_{l\,\in\,\mathbb{Z}} A_l B_{2l}^{(\mathrm{T})} C_l \\ &= \sum_{l\,\in\,\mathbb{Z}} A'_l B'^{(\mathrm{T})}_{2l} C'_l \exp\left(k_d i l \left(y_1 - 2y_2 + y_3\right)\right) \\ &= \sum_{l\,\in\,\mathbb{Z}} (A'_l)^2 B'^{(\mathrm{T})}_{2l} \exp\left(k_d i l \left(y_1 - 2y_2 + y_3\right)\right) \ . \end{aligned} \tag{2.47}$$

With the positions of the first (y_1) and third grating (y_3) being extracted, the coefficients of the centred gratings are identical, thus $A'_l = C'_l$ is used in the last step. A characteristic

measure of a fringe pattern is its visibility. Equation 2.47 allows to directly derive a general expression for a Talbot-Lau interferometer's visibility. It yields

$$\begin{aligned}\mathcal{V}_{\mathrm{T}} = \frac{S_{\max} - S_{\min}}{S_{\max} + S_{\min}} &= \frac{\sum\limits_{l\,\in\,\mathbb{Z}} \left((A'_l)^2 B'^{(\mathrm{T})}_{2l} - (A'_l)^2 B'^{(\mathrm{T})}_{2l} e^{\pi i l} \right)}{\sum\limits_{l\,\in\,\mathbb{Z}} \left((A'_l)^2 B'^{(\mathrm{T})}_{2l} + (A'_l)^2 B'^{(\mathrm{T})}_{2l} e^{\pi i l} \right)} = \frac{\sum\limits_{l\,\in\,\mathbb{Z}} (A'_l)^2 B'^{(\mathrm{T})}_{2l} \left(1 - e^{\pi i l}\right)}{\sum\limits_{l\,\in\,\mathbb{Z}} (A'_l)^2 B'^{(\mathrm{T})}_{2l} \left(1 + e^{\pi i l}\right)} \\ &= \frac{\sum\limits_{n=1}^{\infty} \left(A'_{2n-1}\right)^2 B'^{(\mathrm{T})}_{4n-2}}{\frac{1}{2} \cdot \left(A'_0\right)^2 B'^{(\mathrm{T})}_0 + \sum\limits_{n=1}^{\infty} \left(A'_{2n}\right)^2 B'^{(\mathrm{T})}_{4n}} \,, \end{aligned} \tag{2.48}$$

where the signal's maximum $S_{\max}$ is attained when the three gratings are aligned $y_1 - 2y_2 + y_3 = 0$. The signal reaches a minimum when the last grating is shifted by half a period with respect to the fringe pattern, thus $y_1 - 2y_2 + y_3 = d/2$. It is important to point out that equation 2.47 and 2.48 provide a direct determination of a Talbot-Lau interferometer's signal and visibility for a given configuration defined by the wavelength λ, the grating separation L, the open fraction η, and periodicity of the grating d.

2.4.2. Moiré Deflectometer in Classic Phase-Space Representation

As the treatment of the Talbot-Lau interferometer is kept very general, one can argue that the findings from the previous section include the classical case a priori. This would mean, that the signal and visibility of a moiré deflectometer can be determined by setting the wavelength λ to a sufficiently small value, so that the Talbot length L_{T} is much longer than the grating separation L – making diffraction negligible. However, one can derive a similar result [64] by treating the moiré deflectometer in classical phase space. The calculations are in many aspects analogous to the quantum mechanical treatment. A probability distribution $f(\mathbf{r}, \mathbf{p})$ in classical phase space replaces the Wigner function. Following [64], the free evolution is given by

$$f(\mathbf{r}, \mathbf{p}) = f_0 \left(\mathbf{r} - \frac{L}{p_z} \mathbf{p}, \mathbf{p} \right) \;; \tag{2.49}$$

it thus is equivalent to equation 2.30. The pivotal difference results from the different treatment of the gratings, which does not include diffraction. Here, the convolution kernel is given by

$$T_{\mathrm{C}}(\mathbf{r}, \mathbf{p}) = \frac{1}{h^2} \int \mathrm{d}\boldsymbol{\Delta} e^{i\mathbf{p}\boldsymbol{\Delta}/\hbar} |t(\mathbf{r})|^2 = |t(\mathbf{r})|^2 \delta(\mathbf{p}) \,, \tag{2.50}$$

so that the passage of a grating results in the probability distribution

$$f_{i+1}(\mathbf{r}, \mathbf{p}) = |t(\mathbf{r})|^2 \, f_i(\mathbf{r}, \mathbf{p}) \,. \tag{2.51}$$

After passing two gratings separated by the distance L, one obtains in the observational plane (compare to equation 2.37):

$$f_4(\mathbf{r},\mathbf{p}) = \left| t_1\left(\mathbf{r} - \frac{\mathbf{p}}{p_z} 2L\right)\right|^2 \left| t_2\left(\mathbf{r} - \frac{\mathbf{p}}{p_z} L\right)\right|^2 \ . \tag{2.52}$$

The signal and visibility of the moiré deflectometer with a scanning third grating are

$$S_{\mathrm{C}}(y_1, y_2, y_3) \propto \sum_{l\,\in\,\mathbb{Z}} (A'_l)^2 B'^{(\mathrm{C})}_{2l} \exp\left(ilk_d(y_1 - 2y_2 + y_3)\right) \tag{2.53}$$

and

$$\mathcal{V}_{\mathrm{C}} = \frac{S_{\max} - S_{\min}}{S_{\max} + S_{\min}} = \frac{\sum\limits_{n=1}^{\infty} \left(A'_{2n-1}\right)^2 B'^{(\mathrm{C})}_{4n-2}}{\frac{1}{2}\cdot (A'_0)^2 B'^{(\mathrm{C})}_0 + \sum\limits_{n=1}^{\infty} (A'_{2n})^2 B'^{(\mathrm{C})}_{4n}} \ . \tag{2.54}$$

Note that they have the same form as for the Talbot-Lau interferometer. The only difference is given by the coefficients of the second grating $B^{(\mathrm{C})}_j$, which do not depend on the Talbot length (compare to equation 2.44):

$$B^{(\mathrm{C})}_j = \sum_{m\,\in\,\mathbb{Z}} b_m\, b^*_{m-j} \ . \tag{2.55}$$

2.5. From Classical Paths to the Wave Regime

The classical signal S_C and the Talbot-Lau signal S_T show a strong resemblance as the only difference lies within the Fourier components $B_l'^{(\mathrm{C})}$ and $B_l'^{(\mathrm{T})}$, where the latter contains the additional phase factor $\exp\left(2\pi i \left(l^2 - jl\right) {}^{L}/_{L_\mathrm{T}}\right)$. For very short wavelengths or when the grating separation L is much smaller than the Talbot distance L_T, i.e.

$$L \ll L_\mathrm{T} = \frac{d^2}{\lambda} \ , \tag{2.56}$$

this phase factor vanishes. One can therefore see the moiré deflectometer as the classical limit of a Talbot-Lau interferometer and equation 2.56 as the characteristic limit [38] between both regimes. Another special case is even more intriguing. If the grating separation L equals a multiple, positive integer of the Talbot length L_T, i.e.

$$\frac{L}{L_\mathrm{T}} = s \in \mathbb{N} \ , \tag{2.57}$$

the Fourier components of the Talbot-Lau signal become

$$\begin{aligned} B_{2l}'^{(\mathrm{T})} &= \sum_{j\,\in\,\mathbb{Z}} b_j' b_{j-2l}'^{*} \exp\left(2\pi i \left(l^2 - jl\right) \frac{L}{L_\mathrm{T}}\right) \\ &= \sum_{j\,\in\,\mathbb{Z}} b_j' b_{j-2l}'^{*} \exp\left(2\pi i \left(l^2 - jl\right) s\right) \\ &= \sum_{j\,\in\,\mathbb{Z}} b_j' b_{j-2l}'^{*} = B_{2l}'^{(\mathrm{C})} \ , \end{aligned} \tag{2.58}$$

so they become identical to the ones of the classical signal. Here, the phase factor vanishes because with $l, j \in \mathbb{Z}$ and $s \in \mathbb{N}$, $(l^2 - jl)s$ is an integer. Two important statements can been drawn from this result:

1. Visibility: The fringe pattern of a Talbot-Lau interferometer of which the grating separation is set to a multiple, positive integer of the Talbot length cannot be distinguished from the fringe pattern of a moiré deflectometer. From the mere observation of this fringe pattern with the visibility $\mathcal{V}$ one cannot conclude whether the device operates in the wave regime or in the classical regime.

2. Phase: If one has two (or more) waves sources of different (de Broglie) wavelengths λ_i, and each of these comply either with $L/L_{\mathrm{T}_i} = s_i \in \mathbb{N}$ (Talbot-Lau) or $L \ll L_{\mathrm{T}_i}$ (classical), with L being the grating separation of a sole device, the phases of the resulting fringe patterns are identical in the absence of external forces. The observation of a phase difference is therefore a measure of a force.

Both conclusions are of importance for later sections of the work presented. The first one is crucial if one wants to make an experiment to demonstrate that a device actually operates in the wave regime. Following the above statement, this can only be done if one examines a

configuration where the grating separation is not a multiple positive integer of the Talbot length. A possible experiment to demonstrate the wave-like behaviour of antiprotons with a Talbot-Lau interferometer is discussed in chapter 5.

The second statement is visualised in figure 2.6a for the exemplary case of simultaneously having visible light waves of wavelength λ so that the Talbot criteria is fulfilled (here $4L_\mathrm{T} = L$) and particles such as atoms, of the which the de Broglie wavelength is so short that the device operates in the classical regime (see equation 2.56) of a moiré deflectometer. The intensity of the light field is indicated as red shading, the classical particle trajectories are illustrated as straight grey lines; in neither case a force is present. As stated above, in the plane of

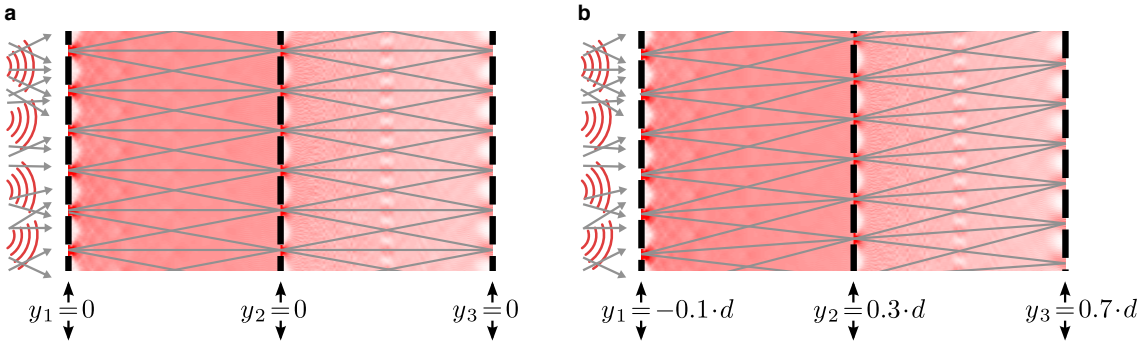

Figure 2.6.: Talbot-Lau interferometry as an absolute reference for moiré deflectometry. (a) Uncollimated particles and waves enter from the left. Classic, straight trajectories (grey) are drawn on top of light field (red shading) for a three-grating configuration. Both patterns overlay not only in the simple case of identically positioned gratings ($y_i = 0$), but also for arbitrary relative positions as exemplary show in (b). This makes the light measurement ideal to measure the undeflected, or force-free, fringe position – a technique later used for a measurement with antiprotons.

the third grating (or the spatially resolving detector), the particles arrive at the positions of the light field's maxima. The device's phase solely depends on the position of the gratings (an arbitrary situation is depicted in figure 2.6b) and does not depend on the collimation or direction of the source. Neither the light nor the particle sources are collimated.

This effect is of special interest if one uses two particle species that couple differently to external fields. The photons of light waves, for example, are not susceptible to electromagnetic fields unlike charged particles, which are deflected. Thus, the observation of a phase difference is a direct measure of a force. An experiment using this technique to measure forces on antiprotons is described in chapter 3. But this method could also be applied to measure the gravitational acceleration of antihydrogen, as the photon's deflection due to gravity is negligible. Even though being in the wave regime, photons can be used to generate a reference fringe pattern that indicates the undeflected position. In this context, one should keep in mind that the Talbot effect is a near-field phenomenon. Consequently, there must be an upper limit on the integer multiple of the Talbot length on which self-images can be observed. Thus, for a given wavelength λ and grating period d, there must be a maximum grating separation one

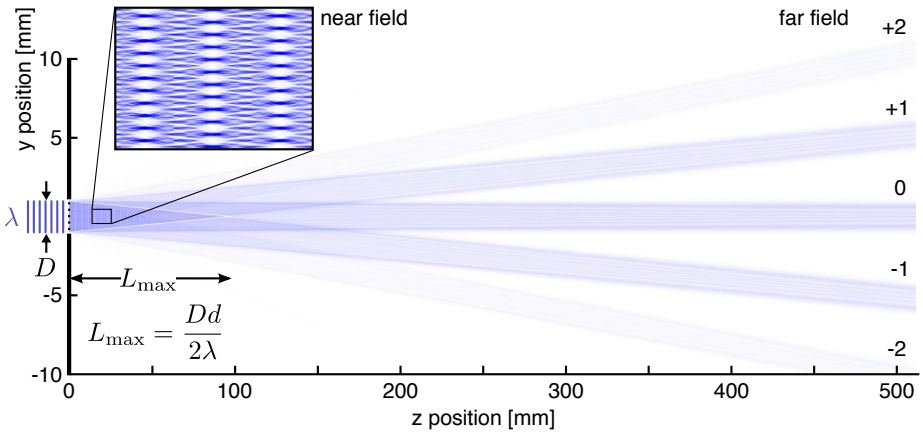

Figure 2.7.: Maximal extent of the Talbot carpet. A plane wave with wavelength λ impinges on a grating with periodicity d and length D. In the far field one observes completely separated diffracted beams, which contain no self-imaging features. The Talbot effect is restricted to areas where the diffracted beams overlap; the outer extent has the shape of a cone where the diffraction orders +1, 0, -1 interfere. The length of the cone is given by the diffraction angle $\sin(\alpha_n) = n\lambda/d$, it is therefore favourable to use short wavelengths such as blue light in the visible regime.

can realise. It is therefore important know how far the near-field goes and where the far field begins. The previous treatment of the Talbot effect presumed the use of gratings with infinite length, which results in an infinite number of self-images being observable. An approximate estimation for gratings with finite length can be derived as follows. Figure 2.7 depicts the computed light field of a finite grating with periodicity $d = 40\,\mu\text{m}$ and the length $D = 2\,\text{mm}$, which is illuminated with a plane wave with wavelength $\lambda = 405\,\text{nm}$. The field is computed with the plane wave decomposition (see equation 2.10) up to a distance of half a meter[6]. At this distant point, the diffraction orders given by equation 2.15 are completely separated and represent the far-field diffraction. Directly behind the grating, one observes the expected Talbot fringes. The principle limit to which these can be observed is therefore given by the volume in which the diffraction orders still overlap. For the ± 1 diffraction orders, this characteristic length is given by

$$L_{\text{max}} \approx \frac{Dd}{2\lambda} = \frac{1}{2} N_{\text{slits}}\, L_{\text{T}} \ . \tag{2.59}$$

The maximum number of observable rephasings cannot be bigger than half the total number of grating slits $N_{\text{slits}} = D/d$. It is favourable to use shorter wavelengths to extend the near-field. Assuming UV light of 405 nm from Blu-ray© laser diodes and the gratings used in this thesis ($d = 40\,\mu\text{m}$, $D = 100\,\text{mm}$) results in $L_{\text{max}} \approx 5\,\text{m}$.

[6] A common problem when numerically evaluating equation 2.10 with the Fast Fourier Transformation are the mirror solutions caused by the finite length of $u(y, 0)$. These are suppressed if one adds sufficient periods to gratings that are completely opaque.

2.6. Inertial Sensitivity of a Moiré Deflectometer or a Talbot-Lau Interferometer

This section focuses on the inertial sensitivity of a moiré deflectometer or a Talbot-Lau interferometer, which is ultimately limited by the shot noise and thus the finite number of particles being detected. The findings presented in the following are the subject of an internal note [88], which was distributed among the members of the AEgIS collaboration. The aim is to find an analytic expression for the relative error $\delta g/g$, rather than to determine the performance of a particular configuration with Monte-Carlo simulations. The result builds on only a few approximations and clearly depicts the scaling of the key parameters of the particle source and the measuring device itself. In this context it is negligible if the device operates in the wave regime or not, as long as one observes a fringe pattern as illustrated in figure 2.8. The fringe pattern, here approximated to first order by a sinusoidal function, is

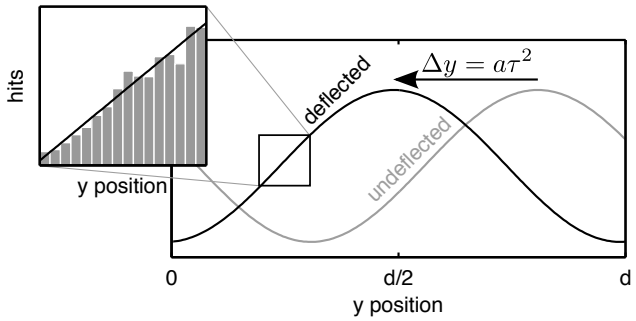

Figure 2.8.: The fringe pattern is shifted by Δy due to an uniform acceleration. The slope of the fringe provides the highest phase sensitivity. The sensitivity is ultimately limited by the shot noise, thus the finite number of detected particles.

shifted due to a uniform acceleration a by the amount $\Delta y = a\tau^2$, with τ being the particle's time-of-flight. The maxima and minima contain negligible phase information: the highest sensitivity on the phase is attained at the steepest section of the signal. The close up shows a histogram on which the count number N_i of the single bins are ultimately shot-noise limited and therefore have a relative uncertainty of $1/\sqrt{N_i}$. The sine function $\sin\phi = \phi - \phi^3/6 \pm \ ...$ has a slope of unity at its zero-crossing; consequently the phase can be determined to a precision of $\delta\phi \approx 1/\sqrt{N_{\mathrm{det}}}$. In the case of a fringe pattern S with reduced visibility

$$\mathcal{V} = \frac{\max(S) - \min(S)}{\max(S) + \min(S)} \ , \tag{2.60}$$

this is further reduced to $\delta\phi \approx 1/(\mathcal{V}\sqrt{N_{\mathrm{det}}})$. For a fringe pattern with N_{det} detected particles and a periodicty d, which is shifted by $\Delta\phi = {}^{2\pi}/_{d} \cdot \Delta y = {}^{2\pi}/_{d} \cdot a\tau^2$, it follows that

$$\delta a = a_{\mathrm{min}} = \frac{d}{2\pi \ \mathcal{V} \ \tau^2 \sqrt{N_{\mathrm{det}}}} \ , \tag{2.61}$$

which is known as the minimal detectable acceleration [38, 89]. For the antihydrogen production as envisioned by the AEgIS collaboration, the number of detected atoms depends on

the solid angle the device covers and is estimated using the simplified geometry shown in figure 2.9. $L_{1\mathrm{st}}$ and L denote the distance from the antihydrogen's starting point to the first

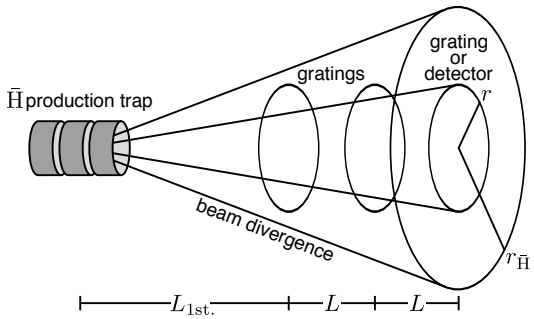

Figure 2.9.: Simplified geometry of the moiré deflectometer (or interferometer) and the antihydrogen beam.

grating and the distance between gratings, respectively. For simplicity, the detector and the gratings are assumed to be round; the size is defined by the radius r. The outer cone with radius $r_{\bar{\mathrm{H}}}$ pictures the antihydrogen beam. The number of detectable antihydrogen atoms

$$N_{\mathrm{det}} = \left(\frac{r}{r_{\bar{\mathrm{H}}}}\right)^2 \cdot \eta^2 \cdot N_{\mathrm{prod}} \tag{2.62}$$

is given by the ratio of the two cones' solid angles (or surfaces of two base areas) and the grating's open fraction η. The total number of created antihydrogen atoms is denoted N_{prod}. It is a reasonable assumption that the detector only covers a fraction of the beam's solid angle, leading to

$$\frac{r}{L_{\mathrm{total}}} \leq \frac{r_{\bar{\mathrm{H}}}}{L_{\mathrm{total}}} = \frac{v_\perp}{v_\parallel} \tag{2.63}$$

with $L_{\mathrm{total}} = L_{1\mathrm{st}} + 2L$ being the total distance from the production point to the detector. The antihydrogen beam's solid angle is given by the ratio of its transversal velocity $v_\perp$ and longitudinal velocity $v_\parallel$. Therefore, equation 2.62 transforms to

$$N_{\mathrm{det}} = \left(\frac{r}{(L_{1\mathrm{st}} + 2L)}\frac{v_\parallel}{v_\perp}\right)^2 \cdot \eta^2 \cdot N_{\mathrm{prod}} \ . \tag{2.64}$$

The transversal velocity of the antihydrogen atoms is dominated by the temperature of the antiprotons in the production trap before the synthesis of the antihydrogen atoms, as the antiproton's inertial mass is three orders of magnitudes larger than the positron's inertial mass. The cloud of antiprotons is assumed to be Maxwell-Boltzmann distributed so that the transversal velocity is given by $v_\perp = \sqrt{(kT/m)}$. The longitudinal velocity $v_\parallel$ is higher than the transversal component as it is boosted via Starck acceleration [61–63]. This envisioned acceleration is a unique feature of the AEgIS experiment as it is this acceleration that forms the beam. Without it, the antihydrogen atoms leave the trap region isotropically. One should

note that the acceleration occurs on a short distance of a few millimetres. Therefore, the atoms can be assumed to be instantaneously accelerated by a 'boosting' factor $\beta \geq 1$, leading to $v_\parallel = \beta v_\perp = \beta\sqrt{(kT/m)}$. The total number of detectable antihydrogen atoms becomes

$$\begin{aligned} N_{\mathrm{det}} &= \eta^2 \cdot \left(\frac{r \cdot v_\parallel}{L_{\mathrm{1st}} + 2L}\right)^2 \cdot \frac{m}{kT} \cdot N_{\mathrm{prod}} \\ &= \underbrace{\eta^2\, r^2}_{\text{gratings}} \cdot \underbrace{\left(\frac{1}{L_{\mathrm{1st}} + 2L}\right)^2}_{\text{geometry}} \cdot \underbrace{\beta^2}_{\text{boost}} \cdot \underbrace{N_{\mathrm{prod}}}_{\bar{H}\text{ source}} \quad . \end{aligned} \tag{2.65}$$

Equation 2.65 determines how many antihydrogen atoms make it to the detector and consequently go into the statistics of the gravity measurement. Nevertheless, the equation is a little suggestive, as it seems to be sufficient to increase the number of detectable antihydrogen atoms. Some of the parameters affect the minimal detectable acceleration (equation 2.61) of the deflectometer, which, using equation 2.65 and $\tau = L/v_\parallel$, becomes

$$\begin{aligned} \delta a &= \frac{d}{2\pi\,\mathcal{V}\,\eta\,r} \cdot \frac{(L_{\mathrm{1st}} + 2L)}{L^2} \cdot v_\parallel \cdot \sqrt{\frac{kT}{m}} \frac{1}{\sqrt{N_{\mathrm{prod}}}} \\ &= \underbrace{\frac{d}{2\pi\,\mathcal{V}\,\eta\,r}}_{\text{gratings}} \cdot \underbrace{\frac{(L_{\mathrm{1st}} + 2L)}{L^2}}_{\text{geometry}} \cdot \underbrace{\beta}_{\text{boost}} \cdot \underbrace{\frac{kT}{m} \frac{1}{\sqrt{N_{\mathrm{prod}}}}}_{\bar{H}\text{ source}} \quad . \end{aligned} \tag{2.66}$$

The parameters (grating periodicity d, visibility $\mathcal{V}$, open fraction η, detector radius r, distance of the source to first grating, grating separation L, boosting factor β, temperature T, number of produced antihydrogen atoms N_{prod}) in equation 2.65 and 2.66 are grouped by the aspects of the experiment they can be attributed to. The minimal detectable acceleration denotes the lower limit one can reach, where the relative precision of the experiment (the ultimate goal of the AEgIS experiment is to reach 1%) is given by $\delta a/g$. This estimation determines the ultimate limit. Not included are possible systematics such as the detection efficiency, the detector's resolution or the support structure within the grating surface, which additionally reduces flux and performance. In order to get a feeling for the difficulty of the task of measuring the gravitational acceleration of antihydrogen, it is instructive to put in some numbers. We already have gratings with a periodicity of 40 µm, a radius of 50 mm and an open fraction of 30 %. The AEgIS proposal foresees to place a deflectometer outside the magnet of the production trap. This implies a minimum distance of ~ 1 m between the point where the antihydrogen is synthesised and the first grating. Assuming a grating separation of 600 mm and that the antihydrogen atoms are accelerated to $500\,\mathrm{m\,s^{-1}}$, one needs a total number of ~ 2000 detected antihydrogen atoms to reach a relative precision of 1 %. Table 2.1 gives an overview of the number of measurement days required to accumulate such an amount of data as a function of the antihydrogen temperature and the number of atoms synthesised per AD shot. The new antihydrogen production scheme of the AEgIS experiment has not been shown to work yet but ones sees how the feasibility of this experiment depends on the

Table 2.1.: Estimated measurement time in days as a function of the antihydrogen temperature and the number of antihydrogen atoms synthesised per AD bunch for the following configuration: $d = 40\,\mu\text{m}$, $L = 0.6\,\text{m}$, $L_{1\text{st}} = 1\,\text{m}$, $v_{\parallel} = 500\,\text{m}\,\text{s}^{-1}$, $\eta = 30\,\%$, $r = 50\,\text{mm}$ and $\mathcal{V} = 80\,\%$.

$\bar{H}$ per AD shot	0.1 K	0.3 K	1 K	4 K
100	1	5	11	44
10	11	55	110	443
1	110	554	1108	4435

temperature and efficiency of the synthesis. One should note that equation 2.66 represents an estimation in the central limit and cannot be extrapolated to arbitrary small numbers of detected particles. Every method (a new approach that requires around 300 particles to work is introduced in chapter 4.) used for evaluating the data has a minimal number of particles required for the algorithm to produce reliable results, so one must assure that enough particles are detected. This can be estimated with equation 2.65. The following overview examines each group of equation 2.66 individually:

Boosting: The scaling of the boost factor β, describing the acceleration of the antihydrogen atoms after their synthesis, is of special interest. The number of detected particles increases significantly with the boost factor, but the minimal detectable acceleration also increases, thus the precision is actually reduced by the acceleration of the antihydrogen atoms! The direct consequence is that one must accelerate the atoms as little as possible – just enough to accumulate the minimum data set required for the evaluation to work. The optimum is to omit the acceleration, which is only a possibility if the antihydrogen synthesis is efficient enough.

Geometry: The geometry denotes the mere size of the measurement device. The distance between the source of antihydrogen and the first grating $L_{1\text{st}}$ should be reduced as much as mechanically possible. The AEgIS proposal foresees a deflectometer outside the production trap's magnet – which implies a minimum distance of at least a metre. For the distance between the gratings L one needs to find the best compromise between the number of detected particles, which favours a short device, and minimising the minimal detectable acceleration, which benefits from a long device.

$\bar{H}$ source: One wants to produce the antihydrogen as cold as possible. The AEgIS collaboration considers two different approaches: The first is to cool the production trap with a dilution refrigerator and the antiprotons with resistive cooling, the second is to cool the antiprotons sympathetically with laser-cooled negative ions or molecules[7].

[7] Fusion of heavier antinuclei is out of reach even though one can dream of catching antihelium nuclei in the cosmic background [90, 91]. Therefore, the mass m is restrained to the lightest antiatom: antihydrogen.

Gratings: Potentially the most interesting parameters are those of the gratings, especially the grating period d. One is interested in minimising it, but if the fringe pattern is detected with a spatially resolving detector (see the experimental results presented in chapter 3), the detector needs to resolve the pattern. Therefore, the periodicity needs to be larger than the resolution of the detector. Chapter 4 introduces a method that overcomes this technical limitation while making efficient use of the antihydrogen statistics. At the same time, the periodicity plays a central role in whether the device operates in the wave regime or not. The visibility $\mathcal{V}$ depends on the open fraction η and, additionally, in the wave regime, on the wavelength itself as described in section 2.4.1. Nevertheless, the visibility and the open fraction leave little room for improvement. Figure 2.9 shows that the detector and the gratings are of comparable size r. In the current status of the AEgIS experiment, both the gratings and the detector have grown to an extent of approximately 100 mm in diameter. Both are based on silicon wafer technologies and are limited by wafer sizes and companies being able to machine large wafers. Without building arrays of gratings and detectors only limited advancement can be expected here.

The general experimental limitation given by the gratings is that one needs to get them, so one depends on what gratings can be realised. It is interesting to note that the ratio between grating period d and $2r$ in equation 2.66 is simply the amount of periods on the grating. The total number of slits on a grating is therefore a valid criterion to evaluate the usefulness of this grating for gravity measurements. When looking for quotes for a new, better set of gratings, one can break down the requirement to: 'How many slits can you make?'.

2.7. Discussion

The review of established descriptions of the moiré deflectometer and the Talbot-Lau interferometer depicts that these devices can be understood within a generalised framework and that their key features such as the shape of the fringe pattern or its visibility can be determined analytically. The characteristic measure to differentiate between the regimes of this framework is the Talbot length, for which an overview is given in table 2.2. Furthermore,

Table 2.2.: The Talbot length $L_\mathrm{T} = d^2/\lambda$ represents the characteristic measure between the different regimes of diffraction.

classical regime	1st Talbot order	upper Talbot limit	far field
$L \ll L_\mathrm{T}$	$L = L_\mathrm{T}$	$L \approx \frac{1}{2} N_\mathrm{slits} L_\mathrm{T}$	$L \gg L_\mathrm{T}$

this elaboration has shown that the simultaneous use of a single device with different particle species enables the measurement of forces based on the phase shifts between their patterns. This also works if the device is not in same regime[8] for each particle species (e.g. classic moiré deflectometer for particles, but Talbot-Lau for photons of visible light).

[8] Interestingly, one uses devices for neutron interferometers also for experiments with X-rays, but the wavelength of these two species are comparable, so that the interferometers are in the same regime [92].

The inertial sensitivity these kinds of devices attain can also be estimated analytically, which depicts the scaling of the critical parameters. The direct measurement of the gravitational acceleration of antihydrogen is a challenging goal and one cannot foresee the performance of the new antihydrogen production scheme. As the AEgIS experiment offers a high modularity, it is worthwhile to use this flexibility to divide this challenge into several experimental steps in order to identify the most promising configuration and determine its systematics. For this purpose, the use of antiprotons from the AEgIS apparatus is of special interest as it is always the antiproton's annihilation that is being detected – also when working with antihydrogen.

Photons have mass? I didnt even know they were Catholic.

(Woody Allen)

3. A Moiré Deflectometer for Antimatter

This chapter reports on a moiré deflectometer for antimatter using antiprotons. It is the first experimental realisation of this tool from atom optics to measure the deflection of an antimatter beam due to a force. The device is in the classical regime for antiprotons but in the wave regime for photons of visible light. The illumination with visible light generates a Talbot-Lau fringe pattern that indicates the undeflected position of the antiprotons[1]. The measured deflection is consistent with a force of 530 aN. The force measured here origins from an electromagnetic stray field and is much larger than gravitation. Still, the combination of techniques from different fields of physics, such as atom optics, particle physics and detector physics denotes a first experimental step towards the detection of gravitational acceleration of antihydrogen with a moiré deflectometer as envisioned by the AEgIS collaboration [28,57,58]. The results presented here are the subject of a publication in *Nature Communications* [89], of which a printout can be found in appendix D.

3.1. Measurement Principle and Experimental Setup

This measurement is based on a two-grating moiré deflectometer and a spatially resolving emulsion detector making snapshots of the antiprotons' annihilations. Figure 3.1a illustrates how the antiprotons enter the deflectometer from the left as a divergent beam. Certain trajectories can pass the two gratings and these antiprotons annihilate inside the emulsion detector, leaving characteristic annihilation stars as in figure 3.2. It is interesting to note that the first observation of an antiproton's annihilation star at the Bevatron succeeded using an emulsion detector [93] and that this type of detectors still provide the highest spatial resolution. The emulsion detector is identical to the ones used in the OPERA experiment [94], which is searching for neutrino-induced τ-leptons. Further details on emulsion detectors can be found in reference [95,96]. Figure 3.1b depicts the possible trajectories through the two gratings. The ensemble of detected antiprotons forms a fringe pattern on the detector. If no force is present, the trajectories (indicated as straight grey lines) are not deflected. If a force acts on the antiprotons, the trajectories (blue lines) are deflected by $\Delta y = {}^{F}/_{m} \cdot \tau^2 = a\tau^2$ in comparison to the force-free trajectories. The position of the undeflected fringe pattern is independently measured with light, using this two-grating system as a Talbot-Lau interferometer for visible

[1] The measurement principle is therefore a direct application of the second conclusion made in section 2.5.

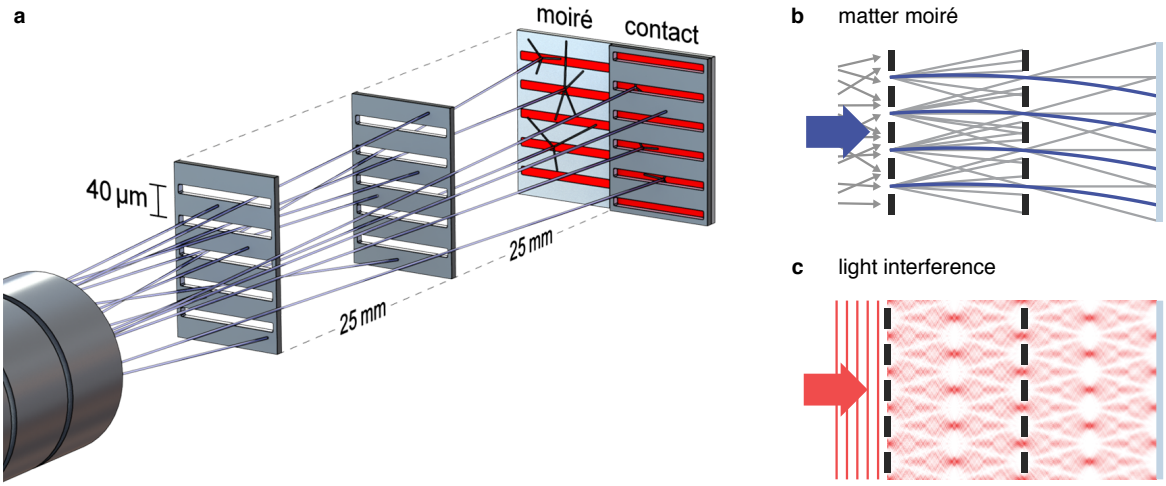

Figure 3.1.: Moiré deflectometer for antimatter [89]. Two identical gratings with periodicity d and a spatially resolving emulsion detector form the moiré deflectometer in (a). A divergent beam of antiprotons enters from the left. The slits only allow certain trajectories to pass both gratings and reach the detector, on which one observes a fringe pattern with the same periodicity d. (b) In the presence of a force along the direction of the grating vector, the fringe pattern is shifted (blue trajectories) in comparison to the fringe pattern without a force (grey trajectories). The position of the undeflected fringe pattern can independently be measured with light (c) using near-field Talbot-Lau interferometry in a subsequent measurement. An additional grating is placed directly on the detector right next to the deflectometer in (a). Its 'contact' patterns are simple shadows for antiprotons and light, which are used to align the antiproton and light measurement in the post-processing.

light. Figure 3.1c shows the corresponding light field of the two gratings being illuminated with a plane wave. With this technique one can determine the absolute deflection due to a force.

In this realisation, the interference pattern with light is recorded in a subsequent measurement with a flat-bed ccd scanner with high resolution. In order to align the two measurements in the post-processing, an additional identical grating is placed in direct contact with the detector, which is also depicted in figure 3.1a. The illumination of the whole structure with antiprotons or light generates a pattern behind this 'contact' grating, which is a simple shadow. Therefore, the measurements can be aligned in the analysis by overlaying the patterns of the contact grating.

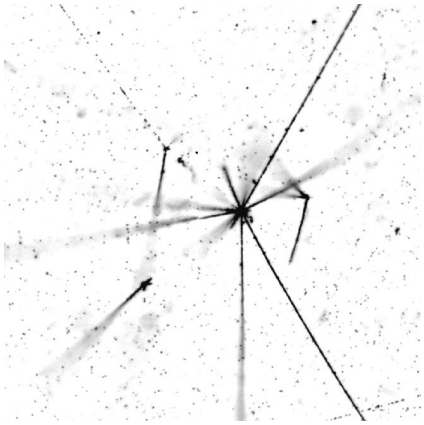

Figure 3.2.: Antiproton annihilation stars observed with the AEgIS apparatus [89]. The annihilation of an antiproton with a proton of a nucleus within the emulsion leaves characteristic, star-shaped tracks. Courtesy of T. Ariga.

3.1.1. Setup

When this experiment was designed, it was intended to assign a single day[2] of antiproton beam time to it before C.E.R.N.'s Antiproton Decelerator (AD) shut down together with the Large Hadron Collider at the end of 2012. An additional operational constraint came from the emulsion detector. As the emulsion detector is photosensitive, it was mounted into the experiment's vacuum chamber in a dark room. The vacuum chamber was then sealed with a gate valve. The whole chamber was then brought to the experimental zone at the AD, mounted to the vacuum chamber of the AEgIS apparatus and pumped down to 10^{-6} mbar. The preparation procedure before beam time took about two hours. One shift of beam time at the AD is eight hours long. A change of an experimental parameter in the middle of the beam time or a repetition of the experiment under modified conditions was therefore not possible. As a consequence, the overall design prerequisite was to incorporate several experimental realisations onto a single support structure to enhance the chance of success. The plan was to illuminate the whole structure for a full shift without interruptions.

The final setup is shown in figure 3.3a. The structure is made from aluminium and brass and is mounted directly onto the emulsion detector with eight screws. The structure's rigidity ensures passive stability over the measurement time. The detector has a feed size of 68 mm. The structure contains two moiré deflectometers of different lengths (2×25 mm and 2×16.7 mm). Additionally, there is a second order moiré, for which the distance between first and second grating is twice as long as the distance between the second grating and the detector (2×33.3 mm and 2×16.7 mm). For this special configuration one expects a fringe pattern of low visibility but with twice the periodicity of the gratings. At last, three contact gratings are placed directly onto the detector. All gratings for this setup were quarried out

[2]Eventually, two shifts were devoted to this experiment. Unfortunately, the emulsion of the second run got overexposed with high energy antiprotons as one of the degrader foils had to be removed from the beam line to debug the antiproton trap, an experimental effort that ran parallel to this measurement.

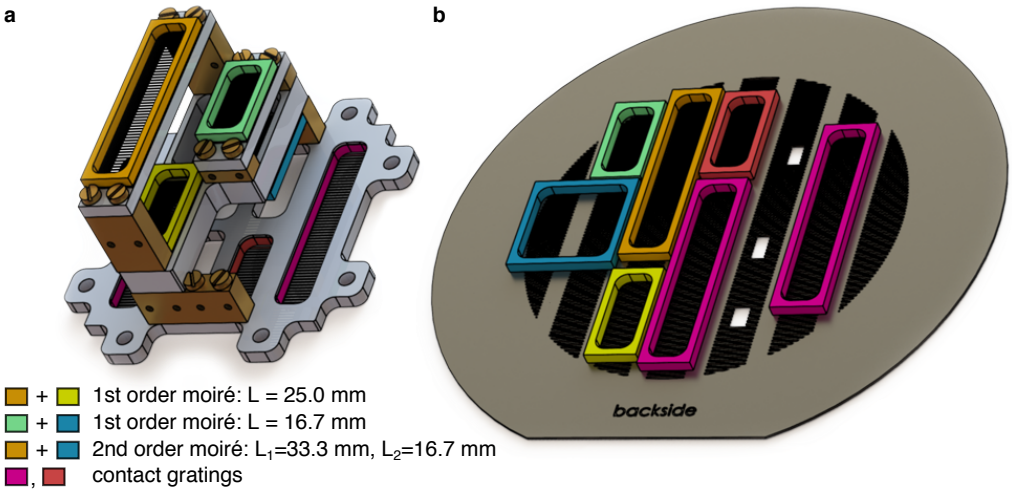

Figure 3.3.: Experimental Setup (a) The structure incorporates several experimental realisations to increase the chance of a successful measurement with a single day of beam time: Two conventional moiré deflectometers, one second order moiré deflectometer and three contact gratings. During the measurement, the emulsion detector is placed below the device and the antiprotons enter from the top. L denotes the grating separation. (b) The required grating pieces are cut out of a 150 mm grating. The arrangement makes efficient use of the undamaged sectors of the grating from an early production batch with several defects such as holes. The coloured aluminium frames are glued with high-vacuum epoxy Torr Seal© onto the silicon grating before scoring rupture lines onto the surface of the silicon. This protects the grating structures when they are subsequently quarried out. The framed grating pieces are subsequently glued onto the structure shown in (a).

of a larger grating etched into a 150 mm silicon wafer[3] with a grating period of 40 µm, a thickness of a 100 µm and a open fraction of 30 %, leading to slit openings of 12 µm. Firstly, stabilising aluminium frames (highlighted in rainbow colours in figure 3.3b) were glued onto the back side of the delicate silicon wafer, making efficient use of the available grating surface. A diamond cutter was used to score rupture lines into the surface of the wafer's front side. By applying the right amount of force, the pieces were subsequently broken out. The single elements were glued onto the support structure while the gratings were illuminated with a Helium-Neon laser. The diffraction patterns of the gratings were used to align the grating vectors of the moiré deflectometers' gratings to a deviation smaller than a 1 mrad.

3.1.2. Data Acquisition

The antiprotons were delivered from the existent parts of the AEgIS apparatus, which is located at the Antiproton Decelerator at C.E.R.N. Every 90 s, the AD provides an antiproton bunch with narrow energy distribution and a mean energy of 5.3 MeV. When a bunch is extracted from the decelerator ring, it passes a set of degrader foils to reduce the mean energy right in front of AEgIS' first Penning trap. The degrading system consists of 170 µm

[3]Details on the production of these wafers can be found in reference [69].

of aluminium and 55 µm of silicon. A simulation, of which the details are discussed below (see figure 3.13a), reveals that the energy distribution after the foils is broad and that the beam is divergent. The mean energy is 106 keV with a root mean squared value of about 150 keV. The antiprotons then pass the 5 T superconducting magnet of the catching trap, followed by the 1 T magnet of the antihydrogen production trap and finally reach the experimental chamber after a flight distance of 3.6 m. Because of the long distance between the foils and the experiment, only a small fraction of the antiprotons reach the experiment but the total number of detected antiprotons is on the order one can expect for future measurements with antihydrogen. In measurements using antihydrogen it is still the antiproton, which is detected, as it provides a much stronger signal than the annihilation of the positron. Many aspects of the following analysis, such as efficient fringe detection, are based on small count numbers and can be deployed to future antihydrogen measurements. The de Broglie wavelength can be estimated to $\lambda_{\mathrm{dB}} = h/p \approx 8.8 \cdot 10^{-14}\,\mathrm{m}$. The device is not in the wave regime and can be described with classical particle trajectories, as $\lambda_{\mathrm{dB}} \ll d^2/L$ is clearly fulfilled (this is classical limit given by equation 2.56). The energy of the antiprotons is so low that the probability of one passing through 100 µm of silicon is practically zero. It is therefore ensured that the antiprotons can only pass the gratings through the slits and that the gratings act as true amplitude gratings. After the exposure to antiprotons, which was reduced to 6.5 hours due to downtime of the AD, the emulsion detector was removed in the darkroom, sealed in lightproof foil and shipped to the microscope lab of the LHEP group at the University of Bern. It was then chemically developed and analysed with an motorised microscope to determine the positions of the annihilation stars.

The reference measurement with light was performed subsequently and did not involve an emulsion detector. An array of red light-emitting diodes (LED) with a spatial diffuser served as a homogenous light source. The whole structure with deflectometer and contact grating was placed on a flat bed ccd scanner with a resolution of 2.7 µm to record the patterns of light. The LED illumination was placed on top of it. The Talbot length[4] for the wavelength used is $T_{\mathrm{L}} = d^2/\lambda = (40\,\mu\mathrm{m})^2/640\,\mathrm{nm} = 2.5\,\mathrm{mm}$, which means that for the deflectometer with $L = 25\,\mathrm{mm}$ one observes the tenth rephasing of the fringe pattern in the plane of the detector.

3.2. Antiproton Fringe Pattern

This section focuses on the evaluation of the antiproton data. This data is basically a list of the x, y - coordinates of the antiproton annihilation stars, which are retrieved from the emulsion with a motorised microscope. Theses positions can be determined with a typical resolution of about 2 µm. The density of detected events is so low that, on average, less than one antiproton is detected per grating period. Consequently, it is not possible to directly *see* the fringe patterns. The primary task is therefore to determine if a fringe pattern is present or not. The exact orientation angle and the periodicity of the patterns are not known a priori,

[4]Two definitions of the Talbot distance are found in literature. The version with an additional factor 2 denotes the first rephasing without a phase shift of $d/2$. The smallest distance to observe a fringe pattern with the same periodicity as the grating is given by the definition used throughout this work.

even though tight limits are given. As described above, the two gratings of the deflectometers were aligned to each other when they were glued onto the support structure, but they are not aligned to the support structure itself with the same precision. Additionally, when the emulsion is placed on the microscope, the rotational alignment is done by hand. Still, the upper limit on the angle is estimated to be about $\pm 20\,\mathrm{mrad}$. The effective periodicity is expected to be slightly larger ($\approx 1\,\%$) than the nominal periodicity of the gratings because of the known expansion [97] of the emulsion during the chemical development. The orientation and the periodicity are therefore extracted from the dataset. It is important to note that the expansion of the emulsion is not completely homogenous and causes distortions (or deformations), which are the cause of a systematic error. The method to measure periodicity and orientation of the patterns, which is discussed in the following, is sensitive enough to detect these local distortions and, as a consequence, it is chosen to restrict the data to two-thirds of the initial emulsion surface. The details on this selection process are discussed in section 3.2.3 and the impact on the result is given in this chapter's discussion.

3.2.1. Rayleigh Test for Efficient Detection of Fringe Patterns

Suitable statistical methods are paramount when working with a small number of events as it is the case with the antiproton measurement described here. A method called Rayleigh test will be shown to be very sensitive for the detection of two-dimensional fringe patterns on unbinned data with unknown periodicity d and unknown angular orientation α. The knowledge of the orientation of the patterns is crucial as one wants to align them with the measurement performed with light to determine a possible deflection. The Rayleigh test produces reliable results even if there is less than one event per grating period. The test was described at first by Lord Rayleigh [98] and later put into the wider context of circular statistics [99–101]. It is used in fields such as the research on the magnetic compass navigation of birds [102, 103] or in astronomy to look for periodicity in the arrival time of X-ray and γ photons to detect pulsars [104–107]. For data given here, one is looking for a periodic signal in the scattered positions of the detected annihilations. It is elegant to investigate this problem on a circle where trigonometric functions replace modulo calculations and the circumference equals the periodicity of the pattern. The Rayleigh test, for which the interested reader can find a derivation in the appendix A, is defined [100] as

$$Z^2 = \frac{2}{n}\left[\left(\sum_{i=1}^{n}\cos\left(\theta_i\right)\right)^2 + \left(\sum_{i=1}^{n}\sin\left(\theta_i\right)\right)^2\right] \,, \tag{3.1}$$

where n denotes the total number of detected events and θ_i is the position of the i-th annihilation star. Figure 3.4 visualises how this test works with antiproton data of the contact pattern. In order to map the two-dimensional annihilation positions of the n antiprotons into the Rayleigh test these positions are projected onto a new axis under the angle α_{test} as seen in figure 3.4a. The original positions are depicted as grey dots and the new projected positions are the blue dots. This new axis is rolled to a circle with circumference $\mathrm{d}_{\mathrm{test}}$ as

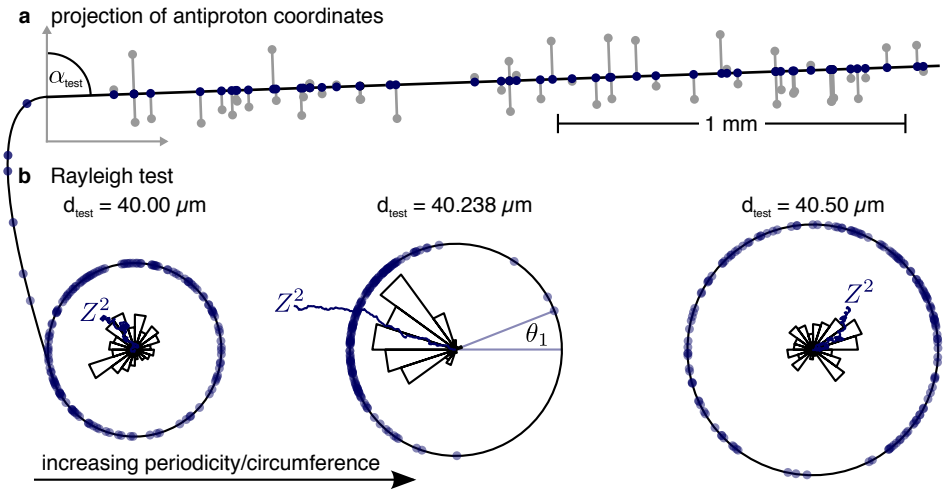

Figure 3.4.: Visualization of the Rayleigh test on antiproton data from the contact grating. (a) The coordinates of the antiproton's annihilation (grey dots) are projected onto a new axis (blue dots) under the angle α_{test}. (b) These 'pearls on a string' are then wrapped several hundred times around a circle with circumference equaling the periodicity d_{test}. If α_{test} and d_{test} match the parameters of the antiproton fringe pattern (here, the circle in the middle), the points accumulate on one side of the circle. Z^2 is a measure of this imbalance. It is proportional to the squared length of the chain of the added vectors $v_i = (\cos(\theta_i), \sin(\theta_i))$, which are plotted in blue. The rose diagrams, which are histograms on a circle, only serve as a guide to eye.

visualised in figure 3.4b. These two steps are expressed by

$$\theta_i = \frac{2\pi}{d_{\text{test}}} \cdot y_i \quad \text{and} \quad y_i = y' \cdot \cos(\alpha_{\text{test}}) + x' \cdot \sin(\alpha_{\text{test}}) \ . \tag{3.2}$$

If d_{test} and α_{test} match the true parameters of an existing fringe pattern, the blue data points accumulate on one side of the circle, which is shown in the middle of figure 3.4b. If they do not match, the points are distributed uniformly on the circle. Examples for d_{test} being to small or to large are shown on the two outer circles of figure 3.4b. The rose diagrams, which are histograms on a circle, only serve as a guide to the eye to better estimate the circular distribution of the points in this figure. To each point i one can attribute the vector $v_i = (\cos(\theta_i), \sin(\theta_i))$ with a length of one. The value Z^2 can then be understood as a normalised squared length of the sum of the single vectors v_i. If all of the vectors point in the same direction, the Rayleigh test Z^2 is maximised. This is visualised in figure 3.4b with the blue string of the vectors v_i, of which the length is maximised for the circle in the middle. Figure 3.5 shows the result of the Rayleigh test on the antiproton data from the long moiré deflectometer ($L = 25\,\text{mm}$) and the adjacent contact grating for a wide parameter range (orientation angle $\alpha_{\text{test}} = (-20\,\text{mrad}, ..., 20\,\text{mrad})$, periodicity $d_{\text{test}} = (38\,\mu\text{m}, ..., 42\,\mu\text{m})$. For these two areas one observes well defined maxima showing that indeed there is a periodicity in the positions of the antiprotons and therefore fringe patterns are detected[5]. Their attributed

[5]The analogous examination of the short ($L = 16.7\,\text{mm}$) and the double fringe deflectometer ($L_1 = 33.3\,\text{mm}$

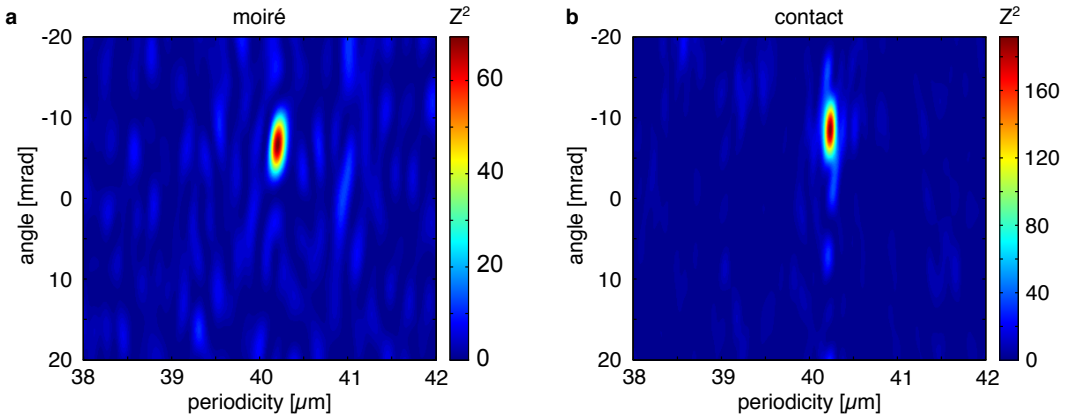

Figure 3.5.: Rayleigh test applied on the antiproton data of moiré and contact area [89]. Z^2 is computed for different orientation angles α_{test} and periodicities d_{test}. Both datasets show clear maxima, from which these parameters are extracted. The measured periodicity is slightly larger than the nominal grating periodicity of 40 µm as the emulsion detector expands during the chemical development.

parameters are within the expected range. Note that Z^2 can reach a maximum value of $2n$ for all vectors v_i pointing in the same direction. The fringe pattern of the moiré deflectometer reaches $Z^2_{\text{max}} = 69.4$ with 241 antiprotons, the pattern of the contact area reaches $Z^2_{\text{max}} = 192$ with 146 antiprotons. The lower value of the moiré pattern results from its reduced visibility in comparison to the contact pattern, which is shown in figure 3.6. Table 3.1 summarises the extracted parameters. The errors are estimated by dividing the data into subsamples, an approach described in detail in section 3.2.3.

Table 3.1.: Key figures of the antiproton fringe patterns.

	peridodicity [µm]	angle [mrad]	hits	size [mm^2]
moiré	40.210 ± 0.011	-6.64 ± 0.18	241	11×6
contact	40.238 ± 0.010	-8.65 ± 0.19	146	15×6

3.2.2. Antiproton Fringe Pattern

An exemplary emulsion area of 1 mm^2 is depicted in figure 3.6a showing ten annihilation stars from the moiré pattern. The emulsion shows stronger darkening than the example shown in figure 3.2. This was caused by a Penning vacuum gauge that was not switched off during this measurement. The photons of its discharge were sufficient to significantly expose the detector. The tremendous advantage of emulsion detectors is that they provide unambiguous and robust particle identification. Despite the background, the positions of the vertices were still retrieved with a resolution of 2 µm. With the knowledge of the fringe pattern's parameters,

and $L_1 = 16.7$ mm) do not reveal a distinct peak so that no fringe pattern can be retrieved.

all antiprotons vertices can be collapsed to one period along the grating vector for the data of the moiré deflectometer (figure 3.6b) and the contact grating (figure 3.6c). The black

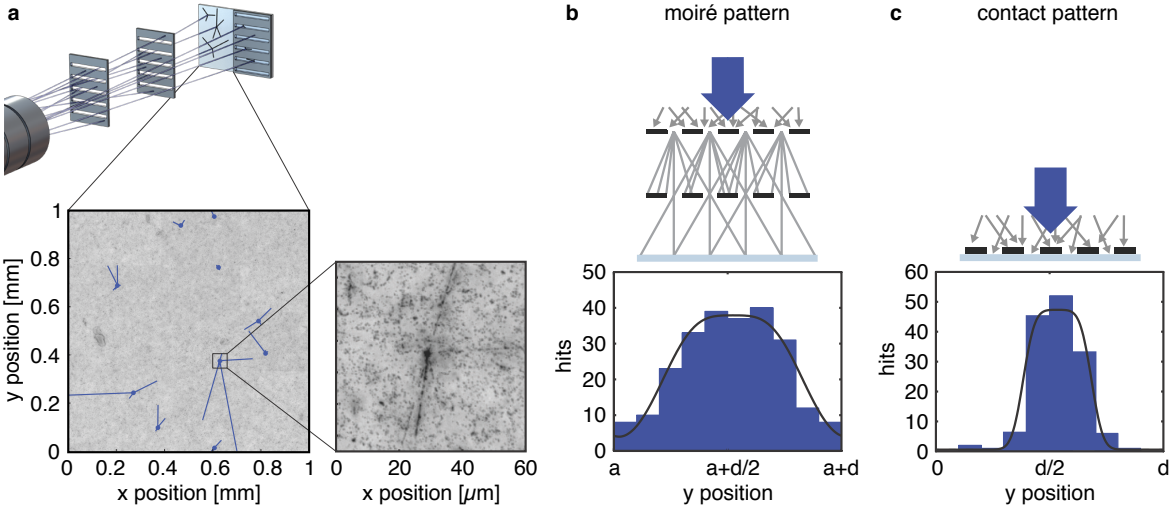

Figure 3.6.: Antiproton measurement [89]. (a) An exemplary emulsion area of 1 mm^2 shows the traces of ten antiproton annihilations, which are highlighted in blue. With the low density of events, there is less than one annihilation per lattice period so that the fringe pattern is not directly visible. With the parameters of orientation and periodicity obtained with the Rayleigh test, the events can be mapped into one period by binning the vertical position modulo the extracted periodicity – revealing the fringe of the moiré (b) and the contact (c) pattern. The black line denotes the expected pattern determined via simulations. A possible shift a due to a force can be determined by comparing this antiproton fringe pattern to the light measurement, which is not deflected.

lines denote the expected distributions due to geometrical constraints and are determined via Monte Carlo simulations. The resulting distribution of the contact pattern is simply a convolution of a box function with an opening fraction of 30 % (the shadow of the gratings) and a normal distribution with $\sigma = 2\,\mu\text{m}$ (the resolution of the detector). The contact pattern has a visibility close to one and the moiré pattern has a visibility[6] of (71 ± 10) %. It is interesting to note that the mere presence of a fringe with high visibility sets an upper limit on the force being present, as an increasing force reduces the visibility for a broad velocity distribution because the moiré deflectometer is a dispersive device. A dedicated simulation based on this effect is used to perform an independent cross-check on the magnitude of the force. This is discussed in detail in section 3.4. The comparison with the measurement of light determines the absolute position of the moiré fringe (indicated as the offset a in figure 3.6b) and therefore provides additional information on the magnitude and the sign of the force. The few hits outside the expected distribution of the contact pattern (figure 3.6c) are consistent with independently observed local grating defects. The gratings used for this experiment originate from an early production batch. Besides substantial defects such as holes

[6]The error of the visibility is estimated with a resampling technique: One repeats the fit on the observed histogram in figure 3.6b with randomised bin counts assuming the single bins to be shot-noise limited.

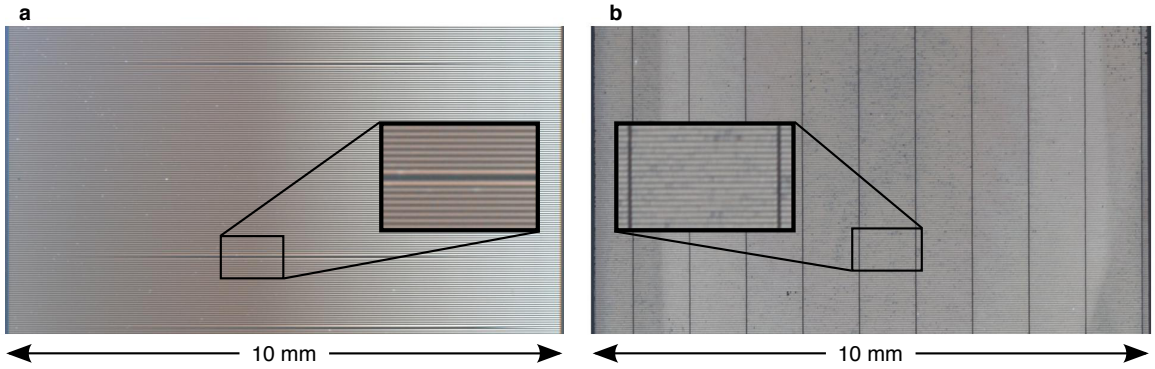

Figure 3.7.: Continuous improvement of grating technology. (a) Photograph of the gratings used for the experiment described here shows partial 'sticking'. A few neighbouring rods stick to each other, leading to a local disruption of the pattern. (b) A new batch of gratings for future use does not show this effect because it features a denser micro support structure.

on the millimetre level, one observes a microscopic effect called 'sticking', where neighbouring rods of the grating touch each other. The larger defects can be easily eliminated by sensible selection of undamaged sectors of the gratings (see figure 3.3). The remaining 'sticking' allows antiprotons arriving on this period to annihilate outside the expected area as the slit's opening is displaced. Figure 3.7a shows a photograph of an exemplary grating area with sticking. A newer batch of gratings shown in figure 3.7b with additional support structures does not show this effect and completely overcomes this issue for future experiments.

3.2.3. Performance of Rayleigh Test and Detected Distortions in the Emulsion

The repetition of the experiment was unfortunately not possible due to the shut-down of the antiproton decelerator at the end of 2012. Two measures are taken to estimate the uncertainties of this single measurement. Firstly, the performance of the Rayleigh test on retrieving periodicity and angular orientation of a pattern is tested with simulated data sets with known parameters d and α. Secondly, the data of the measurement is divided into subsets, which are then individually reanalysed in order to estimate systematic effects. The results of the simulation are shown in figure 3.8, which depicts the standard deviation of the estimates of the orientation angle and the periodicity as a function of the particle number. The results of this figure are determined as follows: Fringe patterns with N particles are generated with random periodicity and orientation angle, which are subsequently re-estimated with the Rayleigh test. This procedure is performed a thousand times for each configuration to estimate the standard deviation and repeated for different numbers of particles N and pattern sizes. Both measured patterns have a longish extent due to the grating geometry; they are approximately three times longer than they are wide. The width of the pattern is set to the experimental value of $\sim 6\,\mathrm{mm}$. The height is varied from 5 to 20 mm. Figure 3.8 shows how the estimates of the statistical errors generally decrease with $\sqrt{N}$. Additionally, the error estimate of the periodicity is inversely proportional to the height the pattern. These clear

dependencies make it possible to parametrise the estimates of the errors for later use such as in figure 3.9. The error estimates from the simulation are now compared to the experimental

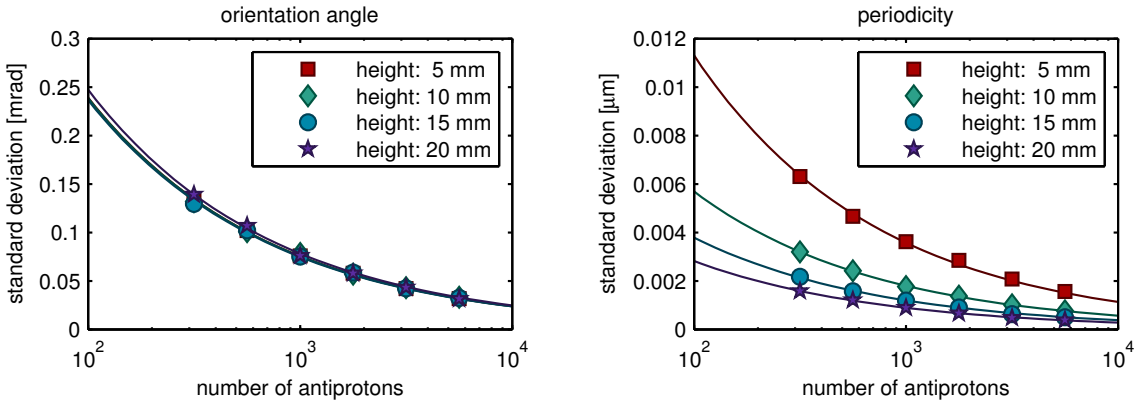

Figure 3.8.: The performance of the Rayleigh test is estimated with simulated datasets for different segment heights and particle numbers. The error estimates generally decrease with the square root of the particle number. The error of the periodicity is inversely proportional to the height of the pattern, which is the direction of the grating vector. The error of the rotation, however, shows a very low dependence on the height.

data via subdivision of these datasets. For data free of systematic errors, one expects that, when the data is divided into smaller subsets, the results on the subsets are within the now increased statistical error limits of the other segments. Figure 3.9 depicts the results of this segmentation analysis for the moiré (left) and the contact pattern (right). The data of each pattern has been divided in up to three segments. Due to the longish extent of the fringe patterns, the datasets are subdivided into shorter segments, which is visualised on top of figure 3.9. For each segment, the Rayleigh test is applied to determine orientation angle and periodicity. The error bars are individually estimated using the results from the simulation (see figure 3.8), thus they depend on the size of the segment and the number of annihilations within the segment. For both patterns, the result on the upper third of the emulsion shows that the periodicity and the orientation angle deviate much more than the statistical fluctuations. This deviation is attributed to and consistent with the known inhomogeneous component of the emulsion's expansion. As a consequence of this detection of deformation, the data of the emulsion is restricted to the lower two thirds of the original area, which show only negligible distortions. The deviation between the remaining two segments, which is used to estimate the uncertainty on the measured angle and periodicity, corresponds to a displacement uncertainty between the moiré and contact pattern of $\pm 1.2\,\mu\text{m}$. To determine the impact of the exclusion of data on the evaluation, the final result using the full dataset is computed as well and given in the discussion. One should keep in mind that the use of the full dataset means to ignore that one can detect distortions with the methods discussed here.

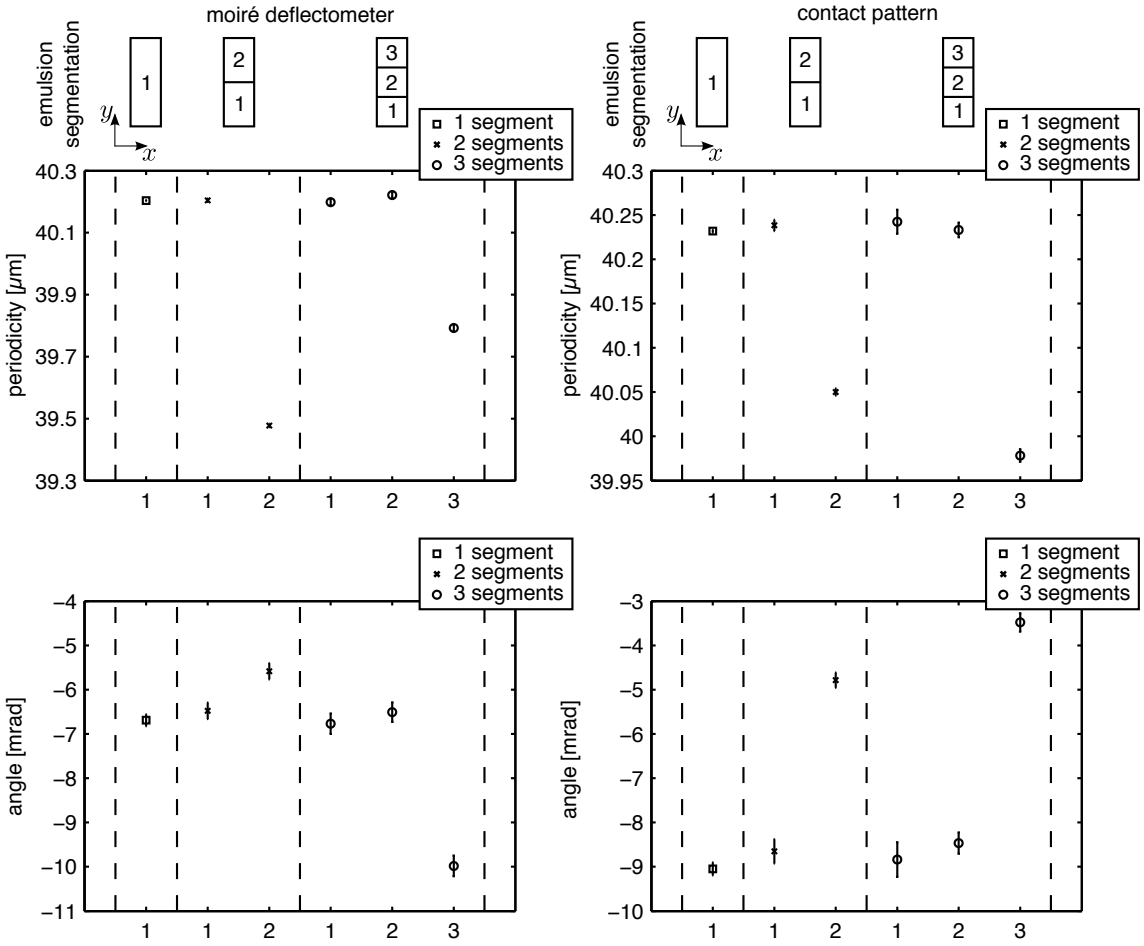

Figure 3.9.: Segmented analysis: In order to look for systematic effects, the emulsion areas (moiré and contact) are divided into up to three subsets as indicated on top of the figure. The Rayleigh test is applied to each subset to determine the patterns' orientation (periodicity and angle). The error bars are estimated with simulated datasets (see figure 3.8). The uncertainties increase for smaller segments as the remaining number of events per segment decreases. As one observes deviating results in the upper third of the emulsion area for both the moiré and the contact pattern, the analysis is restricted to the lower two-thirds of the emulsion area.

For future measurements, the distortion of the emulsion can be overcome with the use of a photomask as shown in [97] or the use of emulsions on glass substrates instead of plastic substrates. The most promising route, though, is to directly imprint the reference fringes of light onto the emulsion, which is photosensitive, before it is chemically developed. The additional advantage of this approach is that the use of the contact grating then becomes obsolete as all information is saved in the emulsion.

3.3. Fringe Pattern of Light and Antiproton Deflection

The evaluation of the antiproton data revealed the deflectometer's fringe pattern, but not if the pattern is shifted or not. The reference measurement conducted with light provides the undeflected fringe position because photons are not deflected by external forces[7]. The analysis of the measurement with light is discussed in this section. The comparison with the results on the antiprotons leads to a measure of deflection due to a force. Systematic limits are discussed and put into perspective with an independent cross-check. Again, there

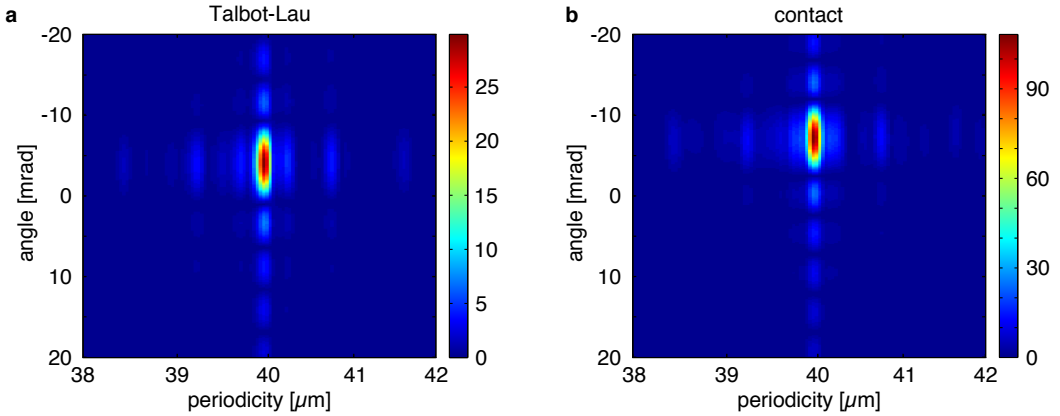

Figure 3.10.: Periodicity and orientation angle of the fringe patterns of light determined with the Fourier transformation. Both datasets show a clear peak.

are two patterns to be analysed in order to determine their periodicity and their orientation. The contact pattern creates a simple shadow, the two gratings of the moiré deflectometer act as a Talbot-Lau interferometer if they are illuminated with visible light. The two fringe patterns of light are recorded using a flat bed ccd scanner with a resolution of 2.7 µm, which is sufficient to resolve the fringes' expected periodicity of 40 µm. The evaluation is analogous to the antiproton analysis, but in contrast to the data retrieved from the emulsion, which is unbinned, the data here is discrete in space as it is a pixelated figure. Hence, one can simply use the Fourier transformation instead of the Rayleigh test to determine periodicity and angular orientation of the fringe pattern. The Radon transformation is used to project the two-dimensional picture onto one axis under the angle α_{test} followed by the one-dimensional Fourier transformation. Figure 3.10 depicts the result of this analysis on the data of the

[7]The deflection of photons due to gravitational lensing is negligible.

Talbot-Lau area and the contact area. Both patterns of light depict distinct peaks similar to the ones of the analysis on the antiprotons shown in figure 3.5. The extracted values of the periodicity and the angle of these two fringe patterns of light are listed in table 3.2. With

Table 3.2.: Key figures of the two fringe patterns of light.

	peridodicity [µm]	angle [mrad]
moiré	39.948 ± 0.030	-4.13 ± 0.08
contact	39.932 ± 0.023	-7.06 ± 0.03

the measured orientations of the four two-dimensional patterns (two antiproton patterns and two patterns of light), one can finally compare antiproton and light measurement. This is shown in figure 3.11a for the same area depicting ten annihilation stars as in figure 3.6, but here in direct comparison to the zero-force reference fringes measured with light. The fringes of light are indicated as a red-coloured shading[8]. The tracks of the annihilation stars are highlighted with blue lines. The alignment of the antiproton and light data is conducted as

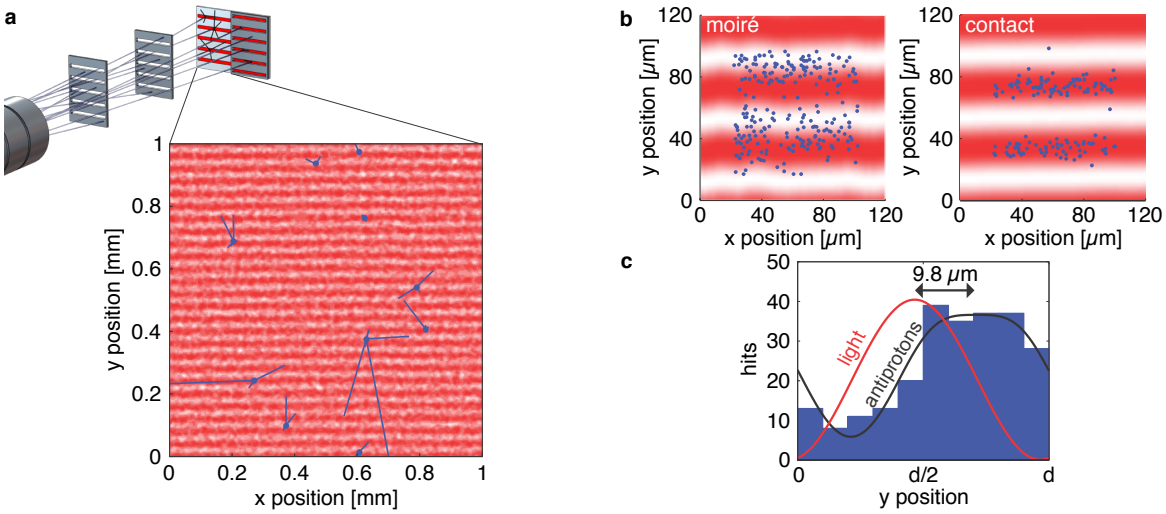

Figure 3.11.: Light measurement [89]. To determine a shift due a force, the antiproton pattern (blue) is compared to the subsequently recorded Talbot-Lau fringe pattern (red) indicating the force-free fringe position. Inset (a) shows the same area as in figure 3.6. In this post-processing, antiproton and light measurement are aligned using the patterns of the contact grating. This is visualised on the right hand side of (b), where the data has been mapped into an area of $80 \times 80\,\mu m^2$. Here, both patterns (blue and red) are simple shadows and are aligned to overlay. Without further alignment, the moiré pattern is compared to the Talbot-Lau pattern on the left hand side of (b). The same data is shown binned into one period in (c), where the shift of 9.8 µm discloses the presence of a force being present.

[8]The data, of which constant offset is substracted, is based on the red channel of the scanner's RGB data.

follows: Firstly, the coordinates of the annihilation stars are globally rescaled to compensate for the emulsion's expansion by multiplying the coordinates with the ratio of the mean values of the measured periodicities given in table 3.1 and 3.2. Secondly, the entire antiproton data is rotated and shifted so that the antiproton pattern and the light pattern of the contact grating overlay. As both patterns of the contact grating are simple shadows they should superimpose as their phase is not susceptible to forces. This is visualised on the right of figure 3.11b, where all annihilation points are mapped[9] into an area of $80 \times 80\,\mu\text{m}^2$. Without further alignment, the pattern of the moiré deflectometer and the Talbot-Lau interferometer can be compared on the left hand side of figure 3.11b, where a slight shift is notable. The same data projected onto the vertical axis and binned into one period is shown in figure figure 3.11c and discloses a mean shift of $\Delta y = 9.8 \pm 0.9(\text{stat.}) \pm 6.4(\text{syst.})\,\mu\text{m}$. The statistical error results from the involved fits, but the dominant uncertainty on this mean shift is given by the uncertainty of the described rotational alignment. The uncertainty of the alignment origins from the

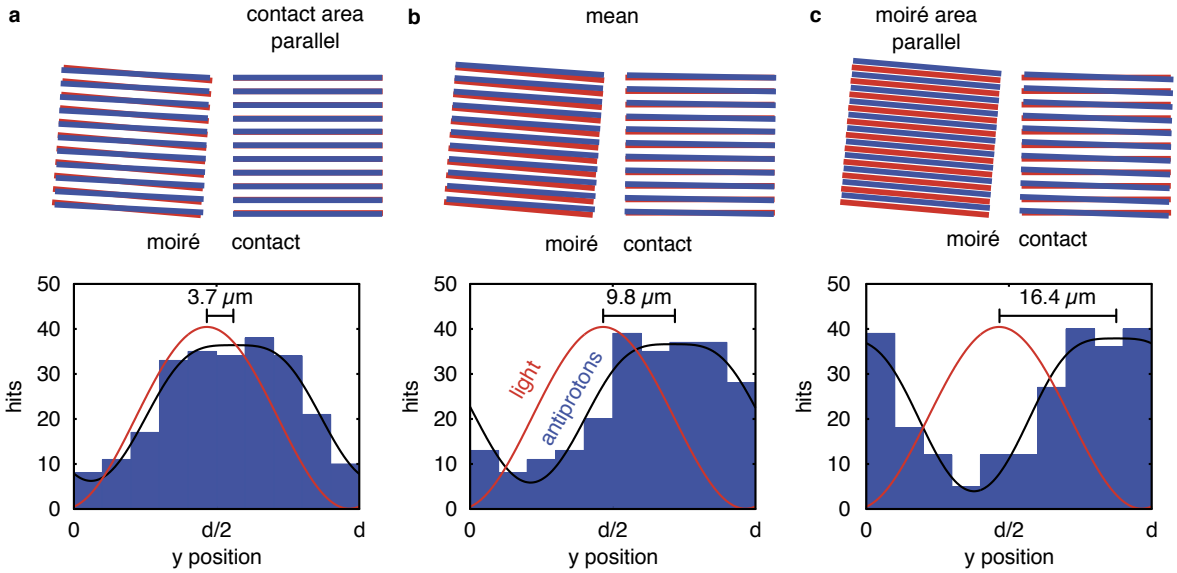

Figure 3.12.: Distortions in the emulsion detector cause a systematic uncertainty on the rotational alignment. The measured angle between the antiproton patterns (blue) and the light patterns (red) should be identical, but they exhibit a deviation of $\Delta\theta = (0.92 \pm 0.27)\,\text{mrad}$. To estimate the impact on the result one can examine the outer bounds of the possible alignments. One can either parallelise the patterns of the contact grating (a) leading to a minimal shift or parallelise the patterns of the moiré deflectometer and the Talbot-Lau interferometer (c). The specified shift of 9.8 µm results from the intermediate alignment (b); the symmetric error interval of ±6.4 µm corresponds to the limits given by (a) and (c).

fact that one observes a different angle between the patterns in the antiproton and in the light measurement. The observed difference is $\Delta\theta = (0.92 \pm 0.27)\,\text{mrad}$. This difference is attributed to the distortions in the emulsion detector and it implies an intrinsic systematic

[9]The mapping is conducted by taking the modulo of the annihilation positions using the measured periodicity.

error. One cannot know how exactly the emulsion's distortions occurred but the systematic limits on the alignment can be estimated by examining the border cases of the rotational alignment for which the analysis is then repeated. This is depicted in figure 3.12, where the top row visualises the rotational alignment of the patterns and the histograms in the bottom line depict the resulting shift between the antiproton and the light pattern. If one assumes that the deformation of the emulsion can be completely attributed to the area of the moiré pattern then the alignment is performed in such a way that the two contact patterns are parallel, which is shown in figure 3.12a. This results in a minimal shift of $\Delta y_{\mathrm{min}} = 3.7 \pm 0.9(\mathrm{stat.})\,\mu\mathrm{m}$. The opposite assumption is that the antiproton contact pattern underwent a deformation. The moiré and the Talbot-Lau pattern are then aligned, as can be seen in figure 3.12c, leading to a maximal shift of $\Delta y_{\mathrm{max}} = 16.4 \pm 0.9(\mathrm{stat.})\,\mu\mathrm{m}$. For the value of the mean shift, it is chosen to repeat the analysis for the intermediate angle and specify the systematic error as a symmetric interval, on which the limits are given by the minimum and maximum shift. This leads to the result of $\Delta y_{\mathrm{mean}} = 9.8 \pm 0.9(\mathrm{stat.}) \pm 6.4(\mathrm{syst.})\,\mu\mathrm{m}$.

3.4. Discussion

The energy distribution of the antiprotons has been simulated[10] with the Geant 4 toolkit [108], taking into account the antiproton beam, the geometry of the experiment, the degrading foil system, and the magnetic fields of the 5 T and 1 T Penning trap magnets along the beam line. The result is shown in figure 3.13a. The mean energy of the energy distribution corresponds to a velocity of $v = 4.5 \cdot 10^6\,\mathrm{m\,s^{-1}}$ and a transit time of $\tau = 5.6\,\mathrm{ns}$. As the pattern's shift is given by $\Delta y = {}^{F}/_{m} \cdot \tau^2$, the measured shift of the antiproton fringe pattern corresponds to a force on the antiprotons of $F = 530 \pm 50(\mathrm{stat.}) \pm 350(\mathrm{syst.})\,\mathrm{aN}$. The antiproton is charged so that the deflection could have been caused by the Lorentz force of a static electromagnetic stray field. An electric field component of $\sim 33\,\mathrm{V\,cm^{-1}}$ in direction of the deflection or a magnetic field component of $\sim 7.4\,\mathrm{G}$ perpendicular to the deflection would have been sufficient to cause the observed shift. A stray field of $\sim 10\,\mathrm{G}$ from the superconducting magnets of the AEgIS apparatus were measured in the area of the moiré deflectometer.

With the use of the velocity distribution one can perform an independent cross-check on a possible shift that does not require any reference or alignment. The moiré deflectometer is a dispersive device. A constant force deflects particles of different velocities by a different amount. Without time-of-flight information on the single events, the fringe patterns of the different velocity classes inevitably mix and smear out the pattern. Consequently, the mere observation of a fringe pattern with high visibility sets an upper bound on a force being present. Figure 3.13b shows the expected visibility of the fringe pattern as a function of the force. The visibilities are determined with a Monte Carlo simulation based on the geometry of the experiment and the energy distribution. This simulation generates the expected fringe patterns, of which three examples are depicted in figure 3.13c. The visibility of these fringes is then determined with the fit of a suitable function. The result of the measurement presented, which is also plotted in figure 3.13b, is consistent with this simulation. The horizontal error

[10] The author gratefully acknowledges the help of G. Bonomi, who conducted the simulation of the energy distribution.

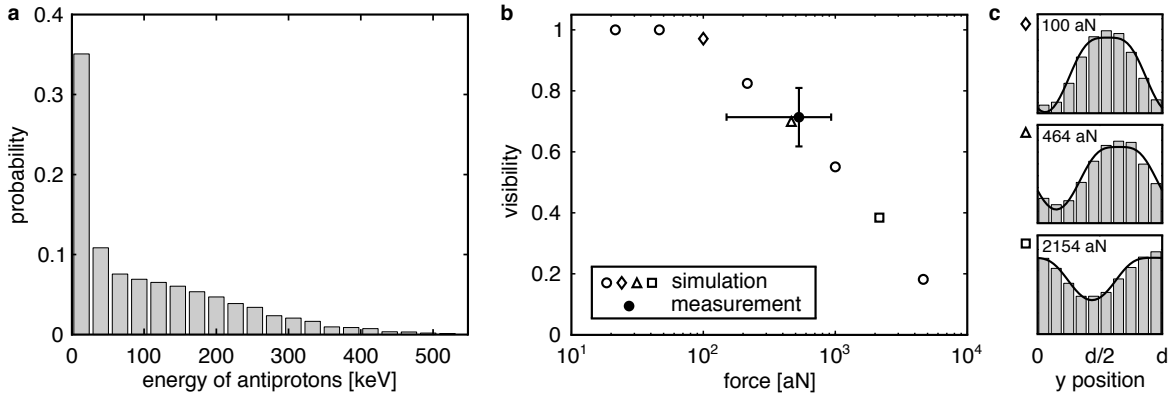

Figure 3.13.: The mere presence of a fringe with high visibiliy sets an upper limit on the force being present [89]. The moiré deflectometer is a dispersive device: particles of different velocities are deflected by a different amount. Consequently, the fringe's visibility decreases for an increasing force. Inset (a) shows the simulated velocity distribution of the antiprotons. This results from a Monte Carlo simulation using the Geant 4 toolkit [108] and is a courtesy of G. Bonomi. Based on this velocity distribution, the expected fringe visibility as a function of the force can be determined and compared to the visibility and force measured (b). This represents an independent cross-check requiring no light reference. Inset (c) depicts three exemplary fringe patterns.

bar is the sum of the systematic error and the statistical error of one sigma. The vertical error bar of the visibility is determined with a resampling technique (see the footnote in section 3.2.2). A force of only 10 fN decreases the visibility below 10 %. For the same reason, one can exclude the possibility that the fringe pattern was deflected by more than one period because the visibility would have been significantly reduced. Note that this indirect approach cannot determine the sign of the deflection and only sets upper limits as the visibility can be reduced due to other reasons.

To quantify a possible bias caused by the selection process described in section 3.2.3, the entire analysis on the phase shift is repeated without excluding any events from locally distorted areas of the emulsion – thus ignoring that one can detect local distortions with the methods presented. The selection process actually introduces a bias as the antiproton patterns slightly change their orientation, but this bias of 2.1 µm is within the systematic error bounds and positive, thus the mean shift of the antiprotons moves away from zero if the full dataset enters the analysis. One can therefore exclude that the observed shift is caused by the exclusion of data points.

In summary, one can say that the result presented does not represent a precision measurement but is a first experimental step of a moiré deflectometer for antimatter. The systematic uncertainty given by this realisation does not represent a principal limitation and can be reduced in future realisations. A new generation of emulsions on glass substrates – a recent development triggered by the results of this work – show less distortions. A major improvement can be achieved by imprinting the reference fringes of light directly onto the

photosensitive emulsion. This way the reference fringes and the antiproton annihilations are saved in the emulsion before the expansion. The direct outcome of such a measurement would be figure 3.11a without the necessity of the contact grating or any alignment in the post-processing.

Many aspects of this experiment are of importance for future antihydrogen measurements as envisioned by the AEgIS collaboration. When using antihydrogen it is still the antiproton's annihilation being detected, for which the emulsion detector provides a clear, practically background free signal with a very high resolution. Additionally, the emulsion detector can easily be scaled up. That makes it compatible to geometries described in the AEgIS proposal [28]. Gravity is a force that is much smaller than the 500 aN reported here. The improvement in sensitivity required to measure the gravitational acceleration of antihydrogen is about ten orders of magnitude – which at first glance may seem inaccessible. This gap results mainly from the ultra short transit time of $\tau = 5.6\,\mathrm{ns}$ of the 100 keV antiprotons. One can easily see how the device can reach a sufficient sensitivity to measure gravity: The minimal detectable acceleration of the moiré deflectometer is given by

$$a_{\mathrm{min}} = \frac{d}{2\pi\,\mathcal{V}\,\tau^2\,\sqrt{N_{\mathrm{det}}}}\ . \tag{3.3}$$

It is inversely proportional to the square of the transit time. The reduction of the antihydrogen's speed to $\bar{v} = 500\,\mathrm{m\,s^{-1}}$ corresponds to an improvement of the sensitivity of eight orders of magnitude. An additional improvement of three orders of magnitude can be achieved by increasing the distance between the gratings from 25 mm to 1 m. The expected shift due to gravity of such a beam ($\bar{v} = 500\,\mathrm{m\,s^{-1}}$ and $L = 1\,\mathrm{m}$) is about 40 µm. This means that the expected shift due to gravity in this future device is comparable to the shift detected in the measurement presented here. An additional lesson learned from this measurement is the importance of the new, absolute referencing technique based on Talbot-Lau interferometry with light. It provide the means to determine a shift without time-of-flight information on the single particles. It also has the potential to generate the required reference when one wants to connect data from different runs – as it will be the case for the future gravity measurement, during which the experiment will accumulate data for several weeks.

The minimal detectable acceleration in equation 3.3 indicates that a smaller grating period is favourable to increase the inertial sensitivity. This is ultimately limited by the spatial resolution of the detector, as one needs to resolve the fringe pattern, which has the same periodicity as the gratings. The following chapter describes a new method using an additional grating in the plane of the detector and an additional vertex reconstructing detector. This approach which will show that this principal limitation can be overcome while making efficient use of the particle statistics.

The 50-50-90 rule: Anytime you have a 50-50 chance of getting something right, there's a 90 % probability you'll get it wrong.

(Andy Rooney)

4. On the use of a third Grating

Two different approaches can be used to detect the fringe pattern of a moiré deflectometer or an interferometer and to measure its phase. The first method is to directly resolve the pattern with a position sensitive detector; the second one is to probe the fringe pattern with a third grating followed by a detector with no spatial resolution. The optimal choice varies from application to application and there are countless examples of both solutions. This section discusses a new detection scheme and a suitable evaluation based on a maximum-likelihood estimator to show that one can efficiently use the particle flux with a three grating system.

To spatially resolve the fringe pattern one requires a position sensitive detector with a resolution considerably smaller than the grating period. For a given detector system this sets a lower limit on the grating periodicity. An integrating detector, meaning a detector whose resolution is insufficient to resolve the pattern but still measures the arrival time of the particles, in combination with a third grating is less complex, however, it comes at the cost of reduced flux as the last grating absorbs on average $1 - \eta$ of the beam's particles, with η being the grating's open fraction. Thus, the majority of the flux does not pass the last grating and does not reach the detector. Typically the third grating is mechanically moved to scan the fringe patten, however, neutron interferometers [92, 109] made of single crystals serve as excellent examples of this not being an absolute necessity. This will be shown to work for antihydrogen (or antiprotons) as well. Experiments with antimatter are in general more challenging than experiments with matter. Nevertheless, figure 4.1 shows that the use of antimatter opens possibilities to obtain information about the system that are unavailable in a matter based experiment. An antiproton stopping in the material of the third grating annihilates. The emerging pions (red tracks) can be reconstructed by a particle tracking detector that surrounds the gratings. The position of the annihilation vertex is determined by extrapolating the pions tracks back to a common point of origin. By reconstructing the annihilation vertex it can be determined if the particle passed through the third grating or stopped within it. In this approach, the statistics of the particles hitting the last grating is not lost but in the contrary provides a complementary output (red tracks) to particles that make it through the last grating (green tracks). A tracking detector based on the scintillation of charged particles as they traverse plastic optical fibres has already been built for the production trap region of the AEgIS apparatus and would be well suited for this application [110]. The design of this existing detector could straightforwardly be adapted to

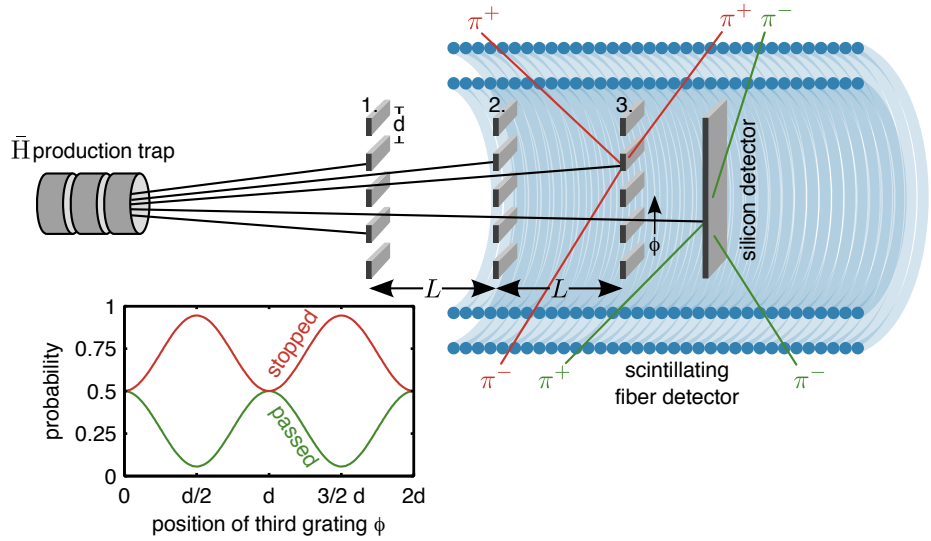

Figure 4.1.: Proposed detection of antiprotons being stopped by a third, scanning grating (red tracks). A third grating reduces the flux of particles that make it to the spatially integrating detector thus reduces the available statistics. Antiprotons however leave a noticeable trace as the annihilation point can be reconstructed by detecting the emerging pions. These events provide a secondary output with a complementary signal.

match the requirements of this method. The following section details a method by which a comparison of the count numbers of transmitted and stopped atoms can be used to measure the gravitational acceleration of antihydrogen atoms. The performance of this method is tested with simulated data sets. For simplicity, the following derivation and simulations focus on the case of a moiré deflectometer. One must stress that the method described in the following can be equivalently applied to a device in a wave regime as long as the probability density function or the shape of the expected fringe pattern is known.

4.1. Coin Toss

For a single antihydrogen atom passing the moiré deflectometer, the following information is acquired: First of all one knows if the atom made it through the third grating or not. Additionally, for a pulsed source one knows the time-of-flight of this atom. The grating position ϕ can be independently measured, for example with Talbot-Lau interferometry using light. The binary character of the first information makes one think of a coin toss, where the result is either heads or tails, with p being the probability of heads for a single throw. The repetition of n throws resulting in k times heads is known as the Bernoulli process where the probability of the outcome is given by

$$L(p) = \binom{n}{k} p^k (1-p)^{n-k} \ . \tag{4.1}$$

For a coin with unknown 'fairness' p, the result of a series of tosses can be used to derive an estimator $\hat{p}$ by maximising $L(p)$, leading to the intuitive result of

$$\frac{\mathrm{d}L}{\mathrm{d}p} = 0 \rightarrow \hat{p} = \frac{k}{n} \ , \tag{4.2}$$

which is a text book example [111, 112] of a maximum-likeliness estimator (MLE). In the following, such an estimator is derived for a three grating system.

4.2. Probability Function for a Maximum-Likelihood Estimator

For a device as seen in figure 4.1, the probability of passage $p_{\mathrm{p},j}$ of the jth antiproton is not a constant like for the coin toss, but a periodic probability function that can be approximated to first order to

$$p_{\mathrm{p},j} = A_0 + A_1 \cdot \cos\left(\frac{2\,\pi}{d}\left(\phi_j + g\,\tau_j^2\right)\right) \ , \tag{4.3}$$

with the grating period d, the last grating's position ϕ_j, the time-of-light $\tau_j = L/v_j$ and gravity g. The probability of the particle being stopped follows as $p_{\mathrm{s},j} = 1 - p_{\mathrm{p},j}$. The probability of the ensemble in which the particles $1 \ldots k$ pass and $k+1 \ldots n$ are stopped is given by

$$L \propto p_{p,1} \cdot \ldots \cdot p_{p,k} \cdot p_{s,k+1} \cdot \ldots \cdot p_{s,n} \ , \tag{4.4}$$

where g is the only free parameter. To evaluate this function it is convenient to apply the logarithm on both sides to circumvent the numerical difficulty of multiplying many very small numbers. As one is only interested in maximising $L(g)$ and the logarithm is monotone for positive numbers, this does not represent a constraint. If $L(g)$ shows gaussian behaviour in proximity of the maximum, its logarithm has parabolic shape to which

$$\log(L(g)) \approx C_1 + C_2 \cdot g + C_3 \cdot g^2 \ , \tag{4.5}$$

can be fitted to determine the parameters C_i. Equation 4.5 directly provides an estimate of the gravitational acceleration and its error. The latter is given by the curvature of the parabola [112]:

$$\hat{g} \pm \delta\hat{g} = -\frac{C_2}{2\,C_3} \pm \sqrt{-\frac{1}{2\,C_3}} \ . \tag{4.6}$$

4.3. Performance on Simulated Data

The maximum-likelihood estimator is tested in the following with simulated data sets. The configuration of this Monte Carlo simulation is chosen to be somewhat realistic in terms of what kind of moiré deflectometer could be built to date. The parameters of the antihydrogen beam reflect the performance one hopes to achieve with production scheme envisioned by

the AEgIS collaboration. The grating's periodicity and thickness is set to 40 µm and 100 µm, respectively. The diameter of the gratings is 100 mm and the open fraction η is 30 %. This corresponds to the parameters of gratings we have at our disposal and are the ones used for the antiproton measurement (see chapter 3). The distance between the gratings is set to $L = 600$ mm leading to a total length of the deflectometer of 1.2 m. The starting point and the velocity of the antihydrogen atoms in three dimensions are randomised. For this, the radial temperature of the antihydrogen atoms is assumed to be 100 mK before being accelerated towards the deflectometer to a uniform distribution between 200 m s^{-1} and 600 m s^{-1}. The trajectories from the starting point towards the first grating, which is placed at a distance of 900 mm, are determined to eliminate the particles that hit a rod of this grating. For the ones passing the first grating, this procedure is repeated until the third grating is reached. A single simulation consists of up to 1000 detected particles. The maximum-likelihood estimator is then applied to the simulated data set. Smaller periodicities of 20 µm and 10 µm are considered as well to investigate the MLE's dependence on the grating period. For each configuration, the simulation and the MLE is repeated 1000 times in order to investigate the statistical performance. One should note that the probability functions need to match

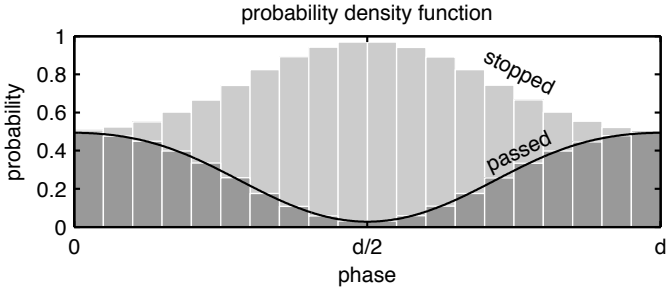

Figure 4.2.: Simulation to determine the coefficients A_i of the probability functions p_p and p_s.

Table 4.1.: The coefficients A_i for the probability function 4.7 for different periodicities d show little variation as the aspect ratio between periodicity to thickness of the grating is kept constant.

	40 µm	20 µm	10 µm
A_0	0.278	0.278	0.278
A_1	0.236	0.239	0.236
A_2	−0.017	−0.015	−0.017
A_3	−0.004	−0.003	−0.003

the actual experimental configuration. For instance the aspect ratio between a slit's opening and the grating thickness can not be ignored as the grating's slits act as tunnels which stop more particles than a infinitesimal thin grating. This effect is increased when reducing the periodicity while keeping the thickness constant. The probability function are therefore

determined to higher order $m = 4$ with

$$p_{\mathrm{p},j} = A_0 + \sum_{i=1}^{m} A_i \cdot \cos\left(i \cdot \frac{2\,\pi}{d}\left(\phi_j + g\tau_j^2\right)\right) \tag{4.7}$$

for every different periodicity d using the Monte Carlo simulation. Figure 4.2 shows the resulting signals of the particles passing the last grating and the one being stopped as function of the last grating's position. For this evaluation the aspect ratio of the gratings is kept constant leading to comparable coefficients A_i which are given in table 4.1. The evaluation's first step is to compute $\log(L(g))$ for a wide parameter scan of

$$g_{\mathrm{test}} = [-1000\,\mathrm{m\,s^{-2}}, ..., 1000\,\mathrm{m\,s^{-2}}]\ . \tag{4.8}$$

The exemplary result of a single run ($d = 40\,\mu\mathrm{m}$ and $N_{\mathrm{det}} = 1000$) in figure 4.3 shows a distinct maximum around the nominal value of $g = 9.81\,\mathrm{m\,s^{-2}}$. The parabolic shape in close

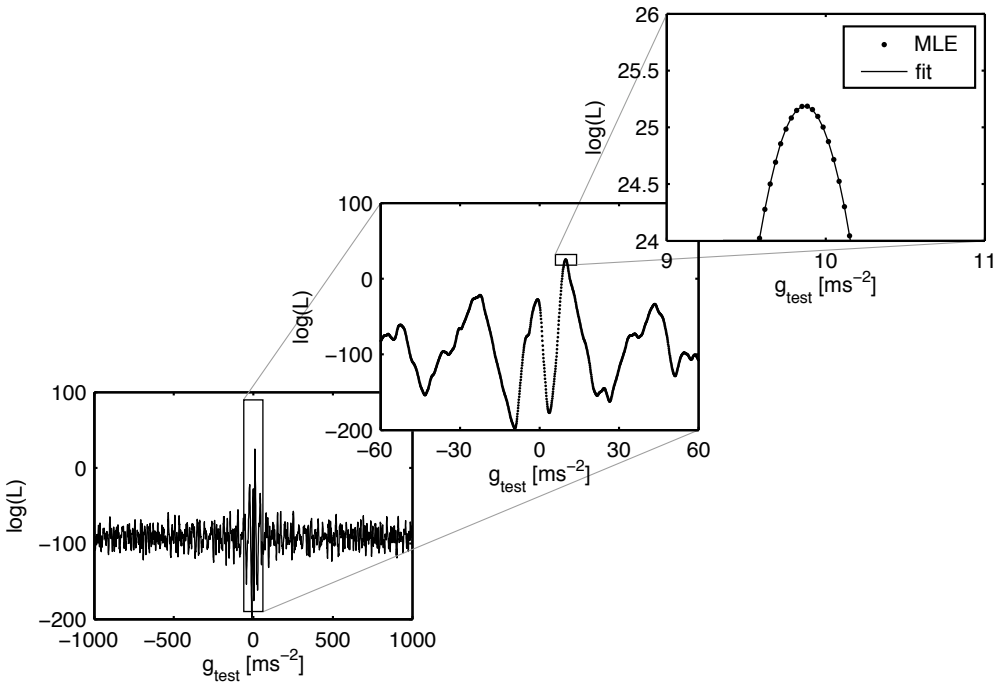

Figure 4.3.: The parameter scan on $g_{\mathrm{test}} = [-1000\,\mathrm{m\,s^{-2}}, ..., 1000\,\mathrm{m\,s^{-2}}]$ on an exemplary simulation with a 1000 detected particles shows a characteristic maximum. The close-up views show that in proximity of this maximum the result of the maximum-likelihood estimator can be approximated by the parabolic function 4.5. The maximum and the curvature are estimates of g and its error, respectively.

proximity of the peak indicates that the estimator itself distributes approximately normally. Following equation 4.6, the position and curvature of the peak deliver single estimates of g and its error δg. To study the statistical behaviour of the estimates, the simulation is repeated

a thousand times for the three grating periods 40 µm, 20 µm and 10 µm. Figure 4.4 shows the result of these simulations, each consisting of thousand detected particles. The top row depicts histograms of the estimates $\hat{g}$ for the three grating periodicities, the bottom row shows the estimates of the corresponding error $\delta\hat{g}$. The estimates of g distribute normally and centre on the nominal value of the gravitational acceleration $g = 9.81\,\mathrm{m\,s^{-2}}$ which is indicated as vertical black line. The introduced bias can been seen to be much smaller than the variance. Additionally, one can see that a smaller grating period significantly reduces the variance of the estimator and therefore improves the performance. The single estimates of the error $\delta\hat{g}$

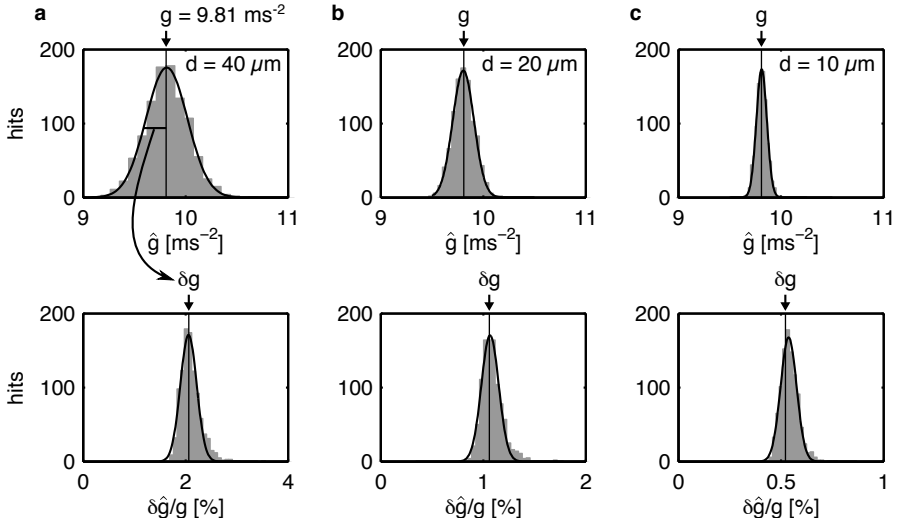

Figure 4.4.: The top row shows the variance of estimator of g, the bottom row the variance of the estimator of δg for a 1000 simulations each. The estimators show a low bias as the mean of $\hat{g}$ centres on the nominal value of g (vertical black line). Likewise, the estimator of the error centres on the standard deviation of $\hat{g}$ drawn above. The value of g and its error determined from a single measurement appear to be appropriate estimates.

should centre on the variance obtained when repeating the simulation and the subsequent estimation of g, which is indicated with the curved arrow. This is fulfilled to a high degree even though one sees a couple of cases for which the error is slightly overestimated.

This evaluation is repeated for varying numbers of detected particles. The results are depicted in figure 4.5, which shows the relative error $\delta\hat{g}/g$ as function of the number of detected particles N_{det}. The data points (a, b, c) denote the data shown above in figure 4.4. The error appears to be decreasing with $\sqrt{N_{\mathrm{det}}}$ and is proportional to the grating period. To put these results into perspective, they are compared to the minimal detectable acceleration (equation 2.61) with a visibility $\mathcal{V}$ of one, which represents the ultimate limit that can be reached

$$a_{\mathrm{min}} = \frac{d}{2\pi\,\mathcal{V}\,\tau^2\sqrt{N_{\mathrm{det}}}}\ . \tag{4.9}$$

The method describes here comes close to this limit. The major reason for not reaching the shot noise limit is the reduced visibility of the two probability functions $p_{\mathrm{p},j}$ and $p_{\mathrm{s},j}$, which

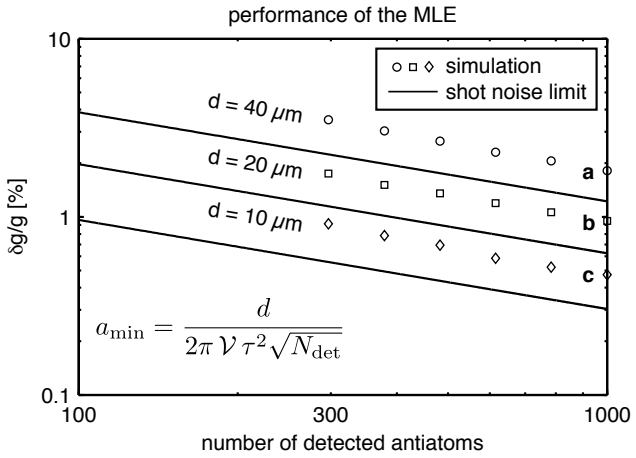

Figure 4.5.: The standard deviation of the estimation of g for an increasing number of detected particles and different grating periodicities. Each point results from the variance of a thousand simulations. The error decreases with the square root of the number of atoms detected N_{det} and is inversely proportional to the grating period. The black solid line denotes the corresponding shot noise limit $a_{\min}$. For exemplary points (a) to (c), the variance of the estimation of g and its error δg are shown in detail in figure 4.4.

results mainly from the opening fraction of the gratings. The expected visibility of both signals as a function of the grating's open fraction η is shown in figure 4.6a. High visibility is attained at small open fractions but the transmitted flux increases with η^2. A compromise is found [38] at open fraction of 30 %, which is the value used here. The signal's visibility for the particles passing the last grating is 83 %, for the ones being stopped it is 31 %. The reduced visibility of the second channel can easily be understood from the geometrical constraints which are depicted in figure 4.6b: The gratings' single slits with an open fraction η restrict the particle trajectories of an uncollimated beam. The shape of the resulting fringe can be approximated by a trapezium. Therefore, the maximum transmission through last grating is limited to about 50 %. At this point, the other half of the flux is being stopped by the last grating, which means that the last gratings always absorbs at least half of the flux. It is easy to convince oneself that for a sufficiently small open fraction, the last grating can be positioned to absorb the complete flux. Therefore, the signal's visibility of the atom being stopped is limited to $\mathcal{V}_{\max} = (1 - 0.5)/(1 + 0.5) \approx 33\,\%$.

One can conclude that a three-grating device can make efficient use of the particle flux and deliver reliable results with less than a thousand detected particles. The premise is that the particles being stopped are detected with an enclosing detector and that the probability functions can be determined. This approach overcomes a significant limitation of the AEgIS two-grating design, whereby the grating period can not be less than the resolution of the spatially resolving detector. The statistical error is proportional to the grating period of the gratings, but it can not be reduced any further in a two-grating system as the detector needs sufficient resolution to resolve the fringe pattern. With the use of an additional third

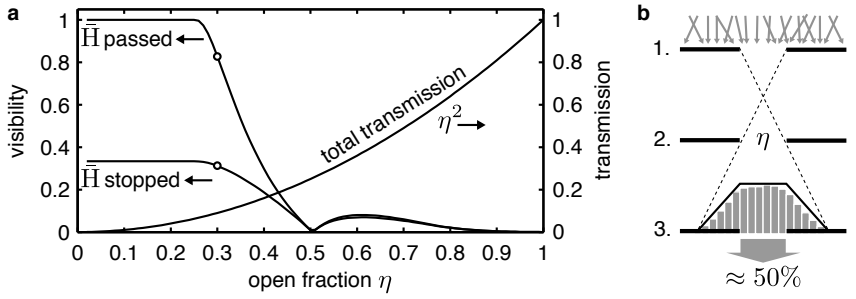

Figure 4.6.: (a) The antihydrogen atoms passing the last grating and the ones being stopped by it generate two complementary signals of which the visibility depends on the grating's open fraction η. The total transmission of the two gratings is approximately η^2. The two dots indicate the expected value for the open fraction of 30 % used in the simulation. (b) The maximal transmission through a slit of the third grating is limited due to geometrical constraints to approximately 50 %, thus the signal's minimum of the atoms being stopped can not be lower than 50 %. The signal's visibility of the atoms being stopped is consequently limited to $\mathcal{V} = (1 - 0.5)/(1 + 0.5) \approx 33\,\%$.

grating, the performance is only limited by the grating period - and therefore by what grating period one can realise. This may allow for a significant improvement over the antihydrogen deflectometer as originally proposed [28] for the AEgIS experiment.

4.4. Dispersion and Symmetry of a Three-Grating System

The approach of a three-grating system described here does not require the last grating to move or to scan the fringe pattern. For the simulations described above, the grating was set to a fix position of $\phi = d/4$. But the balance of these count numbers depends on the time-of-flight, a consequence of the moiré deflectometer being a dispersive device. It is therefore the broadness of the velocity distribution that causes the single absolute maximum of $L(p)$ to emerge. Figure 4.7 shows a broad (grey) and monochromatic (black) velocity distribution and the corresponding values of $L(p)$ for $g_{\text{test}} = [-60\,\text{m}\,\text{s}^{-2}, ..., 60\,\text{m}\,\text{s}^{-2}]$. A monochromatic beam causes periodic solutions as one can not know by how many periods the beam has been

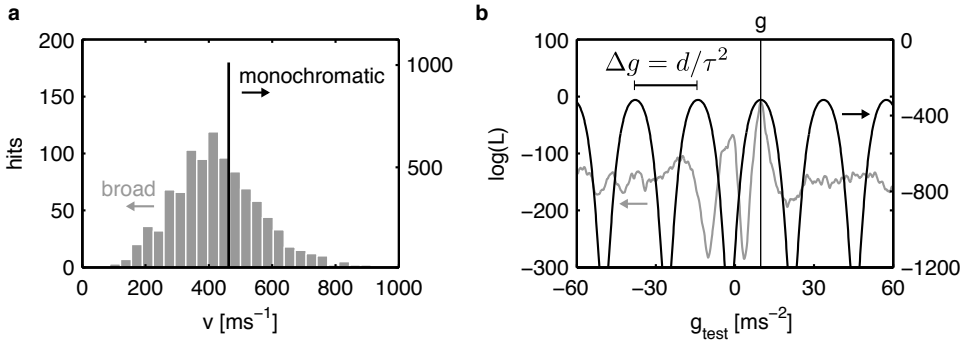

Figure 4.7.: The unambiguousness of the maximum-likelihood estimator's single peak arises solely from the broadness of the velocity distribution and the moiré deflectometer being a dispersive device. Due to the sinusoidal character of the MLE, a monochromatic beam results in periodic solutions with $\Delta g = d/\tau^2$ because one can not determine how many periods the beam has been deflected. Identifying the right peak in this case is impossible.

deflected. This expresses itself in $L(g)$ as one adds up trigonometric functions of the same periodicity for a fixed value of τ. The periodicity of these solutions is simply given by a shift of the fringe pattern by a single period d, for the example given it results in

$$\Delta g\,\tau^2 = d \Rightarrow \Delta g = \frac{d}{\tau^2} = \frac{d\,v^2}{L^2} \approx 23.8\,\text{m}\,\text{s}^{-2}\ . \tag{4.10}$$

A broad velocity distribution is therefore favourable. Furthermore, the above does not mean that the grating's position has to be held for the duration of the measurement. The algorithm allows to input an individual position ϕ_j at the time of the j^{th} event, for example caused by drift as long as this drift is independently measured with light. On the other hand certain positions are to be avoided for the reason described in the following. Figure 4.8 shows a single simulation of 1000 antihydrogen atoms being detected, but repeated with the last grating placed at four different fixed positions ϕ_i. The openings of the three gratings being in line (see inset (a)) corresponds to $\phi = 0$. As the deflectometer is then axis-symmetric along the horizontal plane, one cannot distinguish between up and down. Consequently, $L(p)$ becomes symmetric as well (see figure 4.8) and a second maximum emerges at $-g$. The same occurs for $\phi = d/2$ as shown in (c). This effect is highly suppressed when breaking the symmetry.

$L(p)$ is shown for the intermediate positions $\phi = d/4$ and $\phi = 3d/4$ for which negative g is even the absolute minimum. For the first attempt to measure the gravitational acceleration of antihydrogen, it is therefore required that some of the data is taken while the symmetry of the moiré deflectometer is broken, so that the sign of g is unambiguously determined.

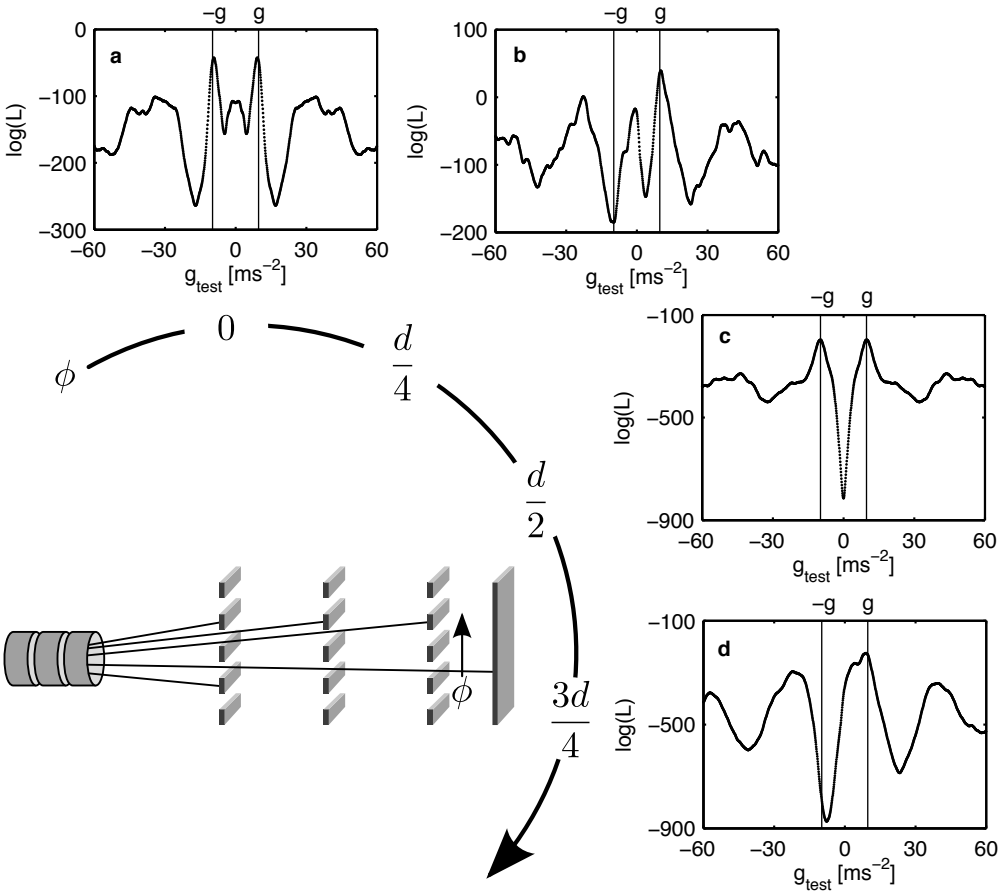

Figure 4.8.: The third grating's position ϕ during the measurement is of special interest. (a) to (d) show the parameter scans on g_{test} for the identical simulation, but with different grating positions ϕ. If the grating position is symmetric ((a) and (c)), one can not distinguish a beam falling upwards or downwards as the parameter scan is symmetric as well, even though the absolute value of g can be determined. To determine the sign of g, it is therefore necessary that a portion of the data is taken with the last grating positioned so that the symmetry is broken ((b) and (d)).

4.5. Discussion

The AEgIS proposal foresees a two-grating design in which the fringe pattern is resolved with a spatially resolving detector. The idea is to use a combination of an emulsion detector and a silicon strip detector. The emulsion detector provides the spatial resolution and the silicon

detector measures the arrival time of the antihydrogen atom. While this 'hybrid' detection scheme, if shown to work, certainly acquires more information, it does not seem to contain significantly more *phase* information, however, it significantly increases the complexity of the device and the mode of operation. The emulsion detector needs to be replaced from time to time to be developed and analysed. Additionally, the use of an emulsion detector sets a couple of mechanical constraints. For instance it cannot be used at 4 K or in ultra high vacuum. On the other side the emulsion detector provides a nearly perfect particle identification what is a great advantage. The ongoing efforts in the collaboration will show if this approach can be realised but it appears to be worthwhile to consider the use a three a three-grating device with an enclosing detector as discussed in this chapter. This may allow for a paradigm change on approaching the measurement of the gravitational acceleration of antihydrogen as it sets no principal lower on bound the grating's periodicity in use while making efficient use of the slim antihydrogen statistics. One is therefore free to reduce the periodicity to increase the inertial sensitivity of the measurement device. The limit is set than by what grating periodicity can be realised. The following chapters examine the use of gratings with significantly smaller grating periods. For the use with antihydrogen having thermal velocities one inevitably brings the measurement device into the wave regime. As, to the knowledge of the author, no interferometers for antimatter have been reported yet, an expedient strategy is to demonstrate such a device in the next experimental step – such as an interferometer for antiprotons (see chapter 5), for which much higher flux is available at the AD.

If you are soft on the hardware,
you need to be hard on the software.

(Claude Amsler)

5. An Antiproton Interferometer

This chapter discusses the possibility of realising an antiproton interferometer within the AEgIS apparatus. The content of this chapter is subject of an internal proposal [113], which was distributed among members of the AEgIS collaboration to promote this experiment. The focus of this experiment is to demonstrate that an interferometer for antimatter can be realised, not to measure gravity.

There is no reason to doubt that antimatter is not subject to the laws of quantum mechanics, however, an interferometer for antimatter has not been demonstrated yet. Several proposals for interferometers using antimatter systems exist, some of these with the intent to measure gravity [30,32,114,115], but demonstrating interferometry with antimatter is by itself of high interest. Experiments using other kinds of 'exotic' matter such as heavy molecules [39,40,116] receive notable attention. This section examines the possibility to demonstrate the wave-like behaviour of antimatter by means of a Talbot-Lau interferometer [73, 75] using antiprotons. The experimental requirements seem to be rather manageable. An experimental attempt can therefore be prepared and implemented on a relatively short timescale in comparison to experiments with antihydrogen. The major complication with the use of antiprotons is the fact that they are charged, but interferometers for charged particles were shown to work (Young's double slit experiment[1] performed with electrons [117]) much earlier than for neutral matter such as neutrons [92,109,118] or even atoms [34,35,37,79,119–121]. Mach-Zehnder and Talbot-Lau interferometry using electrons has been demonstrated [78, 122, 123]. An overview of electron- and ion-interferometry can be found in reference [124]. For interferometry with atoms and molecules refer to reference [125].

At the same time, an interferometer with antiprotons is a worthwhile intermediate step toward the measurement of gravity with antihydrogen. A repetition of the experiment with antihydrogen, when available, should be straightforward and could lead the way towards the measurement of gravity. One should be aware that a successful demonstration of interferometry with charged matter heavier than an electron has not been published. A single result shown in a German PhD thesis [126] in 1997 was not reproduced. The biprism-like

[1] In fact, the double slit experiment with electrons was voted to be 'the most beautiful experiment' by the readers of *Physics World* in 2002.

interferometer used there require a source with high spatial coherence, a difficulty that the Talbot-Lau interferometer described here circumvents as the first grating generates the spatial coherence. Still, a group from the University of Tübingen is reactivating the approach of a biprism using a new type of single atom tip sources [127, 128]. An interferometer using even heavier strontium ions is under development to test coulomb's law [129].

The following estimations reveal that the two key ingredients for interferometry with antiprotons are low-energy antiprotons and gratings with very small periodicity. The gratings under consideration for this experiment are made from silicon nitride membranes with a thickness of 160 nm and have a periodicity of $d = 265\,\mathrm{nm}$, which is a factor 150 smaller than the gratings used in chapter 3. They have a size of $3 \times 3\,\mathrm{mm}^2$. Still, they have four times as many slits. For the use with a charged particle such as the antiproton, the gratings need to be vapour coated with gold to ensure conductivity.

5.1. Scaling of a Talbot-Lau Interferometer for Antiprotons

Given the energy or the temperature, the antiproton's velocity is given by

$$v = \sqrt{\frac{2\,E}{m}} \text{ or } v = \sqrt{\frac{8\,k_b\,T}{\pi\,m}} \tag{5.1}$$

and the de Broglie wavelength follows as

$$\lambda = \frac{h}{p} = \frac{h}{m\,v} = \frac{h}{\sqrt{2\,m\,E}}\ . \tag{5.2}$$

The mean energy and therefore the de Broglie wavelength of the particles defines the length of the interferometer since the distance between two gratings is matched to the Talbot length

$$L_T = \frac{d^2}{\lambda} = \frac{m\,v\,d^2}{h} = \frac{d^2\,\sqrt{2\,m\,E}}{h}\ . \tag{5.3}$$

The Talbot length denotes the distance where a first rephasing of the pattern can be observed and is therefore the smallest possible length of a Talbot-Lau interferometer. The time of flight τ between two gratings follows as

$$\tau = \frac{L_\mathrm{T}}{v} = \frac{m\,d^2}{h}\ . \tag{5.4}$$

Note that τ is independent of the velocity since the interferometer's length equals the Talbot length, which scales linearly with the particles velocity. Due to its charge, the antiproton is susceptible to electromagnetic fields. These fields can reduce the visibility (as previously observed in the antiproton measurement in chapter 3) or even completely smear out the interference pattern. One way to estimate this effect is to determine the force required to shift the pattern by one grating period. This 'critical' force F_crit follows from

$$d \stackrel{!}{=} a\tau^2 = \frac{F_\mathrm{crit}}{m} \cdot \frac{L_T^2}{v^2} = \frac{F_\mathrm{crit}}{m} \cdot \frac{d^4\,m^2\,v^2}{v^2\,h^2}\ , \tag{5.5}$$

mean $\bar{p}$ energy	100 eV	1 keV	10 keV
mean velocity	$1.4 \cdot 10^5\,\mathrm{m\,s^{-1}}$	$4.4 \cdot 10^5\,\mathrm{m\,s^{-1}}$	$1.4 \cdot 10^6\,\mathrm{m\,s^{-1}}$
de Broglie wavelength	$2.9 \cdot 10^{-12}\,\mathrm{m}$	$9 \cdot 10^{-13}\,\mathrm{m}$	$2.9 \cdot 10^{-13}\,\mathrm{m}$
Talbot length	24.4 mm	77.2 mm	244 mm
time of flight	176 ns	176 ns	176 ns
critical force	$1.4 \cdot 10^{-20}\,\mathrm{N}$	$1.4 \cdot 10^{-20}\,\mathrm{N}$	$1.4 \cdot 10^{-20}\,\mathrm{N}$
critical electrical field	$0.089\,\mathrm{V\,m^{-1}}$	$0.089\,\mathrm{V\,m^{-1}}$	$0.089\,\mathrm{V\,m^{-1}}$
critical magnetic field	6.41 mG	2.03 mG	0.64 mG
min. det. acceleration	$1.4 \cdot 10^6\,\mathrm{m\,s^{-2}} \cdot \frac{1}{\sqrt{N}}$	$1.4 \cdot 10^6\,\mathrm{m\,s^{-2}} \cdot \frac{1}{\sqrt{N}}$	$1.4 \cdot 10^6\,\mathrm{m\,s^{-2}} \cdot \frac{1}{\sqrt{N}}$

Table 5.1.: Estimates using an antiproton beam and the grating constant $d = 265\,\mathrm{nm}$.

which can be rewritten as

$$F_{\mathrm{crit}} = \frac{h^2}{m\,d^3}\ . \tag{5.6}$$

This result is quite interesting. The smaller the grating period, the smaller the interferometer's sensitivity to stray fields! Note that there is no energy dependence – the grating period is the only parameter one can tune for a given particle. With the Lorentz force

$$\vec{F} = e \cdot \left(\vec{E} + \vec{v} \times \vec{B}\right) \tag{5.7}$$

one finds

$$|\vec{E}_{\mathrm{crit}}| = \frac{h^2}{e\,m\,d^3} \text{ and } |\vec{B}_{\mathrm{crit}}| = \frac{h^2}{e\ v\ m\ d^3}\ , \tag{5.8}$$

where only absolute components are considered. The minimal detectable acceleration for a given visibility $\mathcal{V}$ and number of detected antiprotons N_{det} is given by

$$a_{\mathrm{min}} = \frac{d}{2\pi\,\mathcal{V}\,\tau^2\,\sqrt{N_{\mathrm{det}}}} = \frac{h^2}{2\pi\,\mathcal{V}\,m^2\,d^3\,\sqrt{N_{\mathrm{det}}}}\ . \tag{5.9}$$

Table 5.1 gives an overview of estimates derived for a variety of antiproton energies between 100 eV and 10 keV using a grating periodicity of 265 nm. The de Broglie wavelengths are comparable to the ones observed in experiments using heavy molecules (compare to [40]). The Talbot length and therefore the size of the device is in the order of tens of centimetres, which gives the impression that such a device can be mechanically realised rather easily. The critical force is four orders of magnitude smaller than the force observed with the antiproton moiré deflectometer (see chapter 3). But the critical force of $1.4 \cdot 10^{-20}\,\mathrm{N}$ is still rather large – which makes the interferometer less susceptible to stray fields. As a comparison, a single charge would need to be placed as close as 130 µm to induce a force of that magnitude. The corresponding critical fields have a magnitude that can commonly be achieved through dedicated shielding. Section 5.4 focuses on the susceptibility of the interferometer to external fields and to the inner beam interaction, i.e. the antiprotons' mutual repulsion.

5.2. Extinction Efficiency of a Thin Silicon Grating

For gratings as thin as 160 nm it is not obvious that an antiproton beam of high energy stops and consequently annihilates within the material of the grating. A high extinction ratio is a requirement for the grating to act as a pure amplitude grating. Figure 5.1 shows the result of a Monte Carlo simulation using the Geant 4 [108] toolkit. It depicts the fraction of antiprotons passing through a silicon foil of 160 nm as function of the antiproton's energy. Above 10 keV, the grating is practically transparent. From this simulation it seems safe to design the experiment for a mean energy around 1 keV.

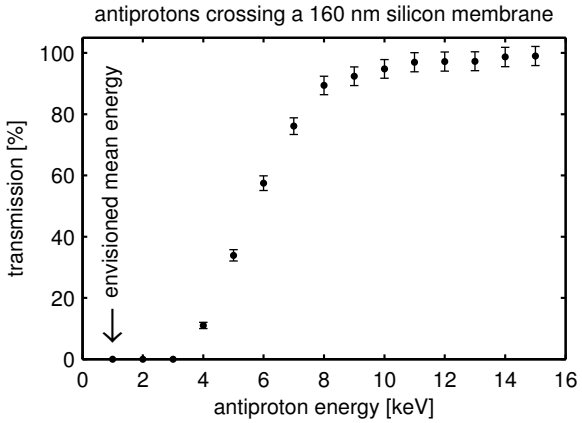

Figure 5.1.: Geant4 [108] simulation showing the fraction of antiprotons passing through a silicon membrane of 160 nm as a function of the antiproton's energy. At energies below 3 keV, the grating acts as a true transmission grating as practically all antiprotons stop within the material. At energies above 10 keV the grating is transparent. Courtesy of G. Bonomi.

5.3. The Fringe Visibility is the Signal

A possible design of an antiproton interferometer for 1 keV is shown in figure 5.2. When using gratings with submicron periodicity, directly resolving the fringe pattern is not possible with available technology. Consequently, the interferometer is a three-grating design, where the last grating is used to probe the fringe pattern. Each grating is placed on a commercial actuator. Two of the actuators are goniometers, whose pivot points are outside the actuators. The third one is a linear actuator which can scan the grating vertically. The rotational alignment between the gratings and the phase can therefore be remotely adjusted. The base plate has a half-round shape so the interferometer fits inside a μ-metal tube for magnetic shielding. The attainable flux of antiprotons at the AD is much higher than for the envisioned antihydrogen production. One can certainly use an enclosing detector as discussed in chapter 4 to profit from the entire statistics. This interferometer could then be used to test MLE and study the systematics of this approach. But as the flux of antiprotons is high one can simplify the device by focussing on the transmitted antiprotons. These can be detected with a silicon detector

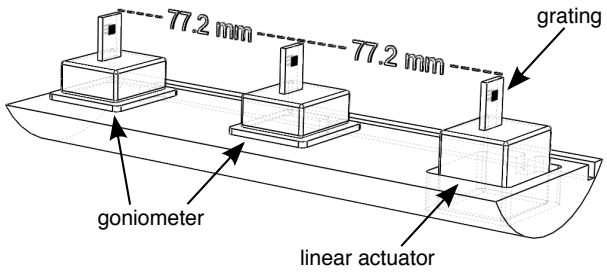

Figure 5.2.: A possible design of an interferometer for 1 keV antiprotons: The three gratings are placed on commercial actuators – two goniometers for rotational alignment and one linear actuator for scanning. The half-round base allows the use of a cylindrical magnetic shield as shown in figure 5.5.

placed behind the third grating. If the last grating is tilted with respect to the antiprotonic fringe pattern (see figure 5.3), the resulting moiré fringes can have macroscopic dimensions as the period of the moiré pattern is given by

$$d_{\text{moiré}} = \frac{d}{2\sin(\alpha/2)} \ . \tag{5.10}$$

Tilting the last grating by a 100 µrad results in macroscopic fringes separated by about a millimetre which can be resolved with a detector having two-dimensional spatial resolution. The visibility of the moiré fringes is equal to the visibility extracted by scanning the third

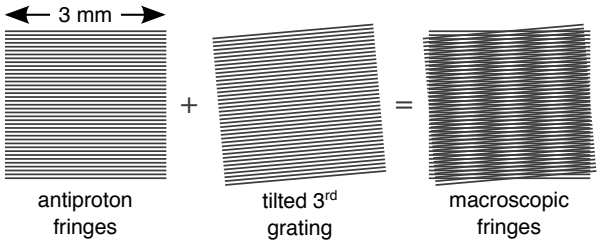

Figure 5.3.: Tilting the third grating circumvents the necessity of scanning it. Assuming sufficient flux, the fringe pattern could be recorded with a single antiproton bunch. The resulting vertical moiré fringes can have a 'macroscopic' extension (≈ 1 mm), which can be resolved with a spatially resolving detector (2D) behind the third grating. (Additional moiré beating can be observed when reading this document on a computer screen.)

grating. The important experimental advantage when tilting the grating is that one can potentially record the fringe pattern with a single antiproton bunch - making vibrations and drift irrelevant. The premise is that sufficient flux can be attained to detect around a hundred antiprotons per bunch – which is sufficient to detect a possible fringe pattern with the Rayleigh test (see section 3.2.1). Otherwise, one must use several bunches and incrementally move the third grating to record the fringe pattern. If low flux demands to accumulate data over several AD cycles, the phase difference between the subsequent measurements cannot be ignored.

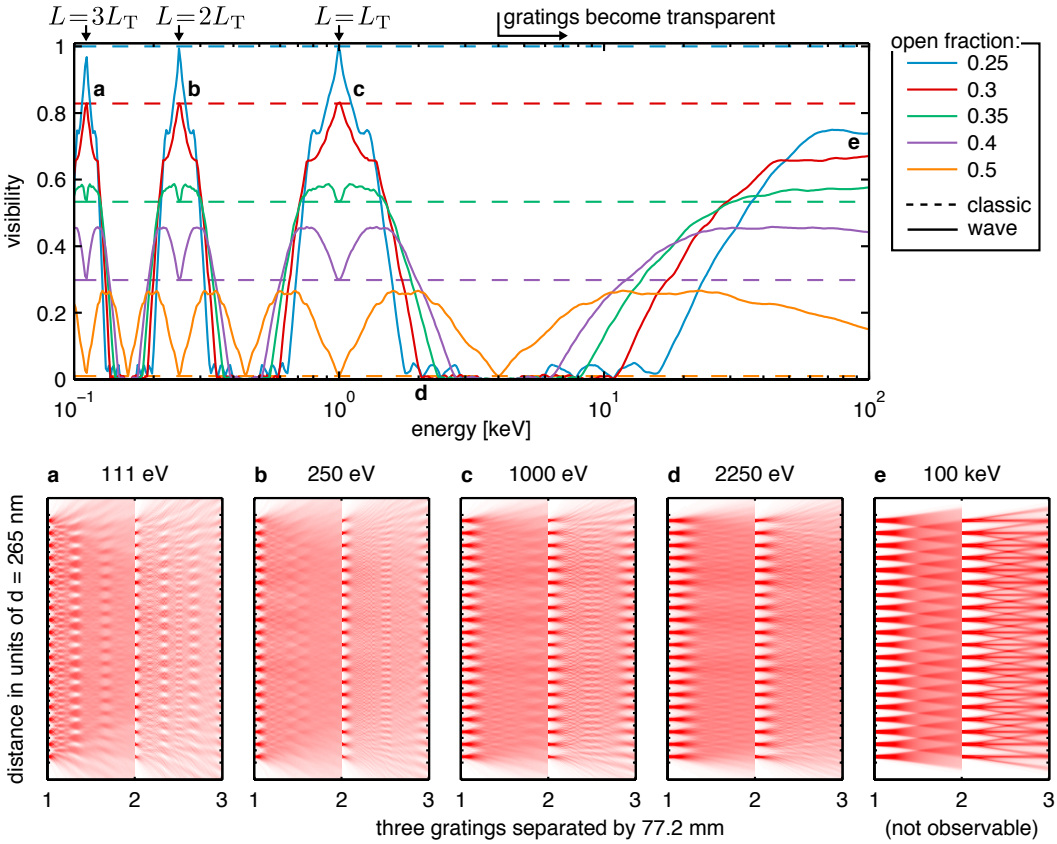

Figure 5.4.: Expected visibilities as a function of the antiproton energy for different open fractions. The grating separation is fixed to 77.2 mm and corresponds to a single Talbot length for 1 keV antiprotons. Measuring the visibility of the fringes as a function of the antiproton energy is a well established way to demonstrate that the device operates in the wave regime (solid lines) because one expects no energy dependence of the visibility in the classical regime (dashed lines): The lower part shows representative intensity fields for an open fraction of 30 %: (a) Grating separation equals three times the Talbot length. (b) Grating separation equals twice the Talbot length. (c) Grating separation equal to the Talbot length. (d) Exemplary energy with low visibility. (e) For increasing energies (decreasing de Broglie wavelength) the pattern resembles classical trajectories – visibility comes back – a classic Moiré deflectometer. Note that this regime is not observable as the gratings are completely transparent for antiprotons of this energy.

It is important to realise that the visibility itself is the figure of merit. One has to demonstrate that the device actually operates in the wave regime as one can also observe fringes in the classical regime (see discussion in chapter 2). The apparent 'smoking gun' is to measure the visibility for different antiproton mean energies. One expects no dependence for a classical device in contrast to a Talbot-Lau interferometer, for which a distinctive rephasing must be observable. For thermal atomic or molecular beams it is typically rather difficult to change the kinetic energy and therefore to tune the de Broglie wavelength. As a consequence, these experiments tune the grating separation (see reference [36]), thus increase the physical distance between the gratings. The mean energy of a charged particle beam can easily be tuned, for example by reaccelerating the particles. This represents an important advantage, as one is not required to change the grating separation during the measurement. The signal one is looking for is shown in the upper part of figure 5.4, assuming a device with a fixed grating separation of 77.2 mm, which corresponds to one Talbot length for 1 keV antiprotons. The expected visibility of the Talbot-Lau interferometer as a function of the antiproton's energy is depicted as a solid line. It is computed with equation 2.48 for different open fractions of the gratings (depicted as solid lines). The visibility of the corresponding moiré patterns, thus ignoring the wave nature of the antiproton, are determined using equation 2.54 and are plotted as dashed lines. The clear distinction between wave-like and classical description arises from the fact that the former depends on the antiproton energy, while the latter does not. The lower part of figure 5.4 depicts the corresponding intensity fields, which are known as 'Talbot carpets', for several energies using an open fraction η of 30 %. The uncollimated wavefronts enter from the left and pass the first and second grating. The resulting intensity field is probed at the position of the third grating. In the insets (a, b, c) of figure 5.4 the Talbot length equals a third, a half and a full grating separation of $L = 77.2\,\mathrm{mm}$, respectively. As expected, these show high visibility. An example of very low visibility is given in (d). Toward high energies (e), all lines approach the classical expectation with no further rephasing being observed – a form of Bohr's correspondence principle. With the gratings foreseen for this experiment, the classic limit can not be observed as the gratings become transparent for energy higher than 4 keV.

It is important to note that if an integer multiple of the Talbot length equals the grating separation, the resulting visibility of the quantum and classical descriptions are identical. Consequently, one cannot distinguish between the two if this condition is met. For low open fractions, the Talbot-Lau fringes' visibility reaches upmost the value of the moiré deflectometer. In contrast, at an open fraction of 50 %, the classical visibility vanishes completely. Therefore, an observed fringe pattern at this open fraction can only result from the wave character of the antiproton. The open fraction of the grating under consideration is slightly larger than 40 %. If one is able to measure the visibility from 500 eV to 3 keV, one should observe a broad peak, with a dip centred at the design wavelength (corresponding to 1 keV). Being able to measure down to 100 eV, thus showing the scaling of the rephasing, would represent even stronger evidence that the device operates in the wave regime.

5.4. Susceptibility to External and Internal Fields

To perform interferometry at the envisioned antiproton energy range around 1 keV, a magnetic shield is required to reduce the residual field between the gratings to below 1 mG. Assuming a residual field in the AD zone of 10 G, a suppression of at least 10^4 is necessary. A multilayer structure of μ-metal can easily achieve 10^3. The suppression can be improved further with three pairs of compensation coils – this type of compensation is commonly used in many experiments. A starting point for good shielding is detailed knowledge of the magnetic field

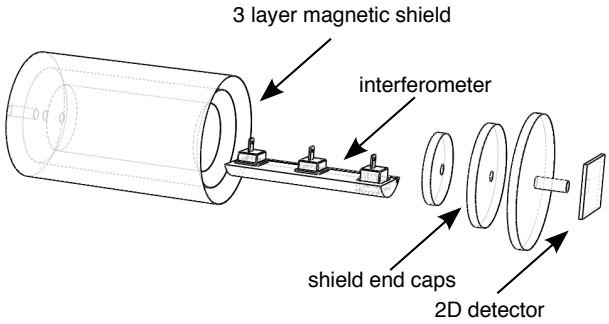

Figure 5.5.: A possible magnetic shield consisting of 3 cylindrical layers of μ-metal. The field entering the cylinders through the axial openings of the antiproton beam can significantly be reduced by adding cylindrical collars to the shield [130]. For a beam with low divergence, the detector can be placed outside the shield - reducing the influence of stray fields from the detector.

one starts with. A recommended approach is to measure the magnetic field map in the area of interest and optimise the shielding's geometry using dedicated simulation software. Figure 5.5 shows the interferometer in a possible three layer cylindrical shielding. This geometry has the advantage that the transversal suppression (the one the interferometer is most sensitive to) is higher than the axial suppression. The inner shield is commonly equipped with with a demagnetisation coil (not drawn) to increase the permeability. This design including the shield fits inside a CF 160 vacuum flange. Note that at a level sufficient for the proposed experiment, the inner conducting shield serves as an electrostatic shield, too.

With increasing antiproton flux, the number of charges within the interferometer increases and the electrostatic repulsion will tend to smear out the pattern. To estimate this effect, one can compare the force due to the space charge with the critical force (see equation 5.6). Following the approach described in reference [131], one can assume a continuous, homogeneous beam with the charge density ρ as shown in figure 5.6. With Gauss' law $\int E \,\mathrm{d}A = \frac{1}{\epsilon_0} \int \rho \,\mathrm{d}V$ follows $E_r \cdot 2\pi\, r\, l\, \epsilon_0 = \rho\, \pi\, r^2\, l$ and thus

$$E_r = \frac{\rho\, r}{2\, \epsilon_0} \ . \tag{5.11}$$

The resulting force due to the space charge expands the beam. The use of Ampere's law $\int B \,\mathrm{d}s = \mu_0 \int j \,\mathrm{d}A$ leads to $2\, l\, B = \mu_0\, j\, l\, r$ and with the current density $j = v\, \rho$ one

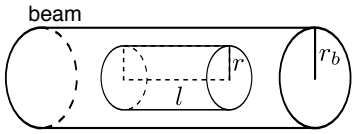

Figure 5.6.: Geometry of a continuous, homogeneous beam with radius r_b and charge density ρ.

finds the expression

$$B = \frac{\mu_0\, j\, r}{2} = \frac{\mu_0\, v \rho\, r}{2} \ . \tag{5.12}$$

The magnetic field acts in the opposite direction of the electrostatic repulsion but is only significant at high velocities. The link between the electric and magnetic component becomes apparent with $\epsilon_0\, \mu_0 = \frac{1}{c^2}$ leading to $B = \frac{\beta}{c}\, E_r$. Both components are brought together in the Lorentz force

$$F = e\,(E_r - v\, B) = \frac{e\, E_r}{\gamma^2} = \frac{1}{\gamma^2} \cdot \frac{e\, \rho\, r}{2\, \epsilon_0} \ . \tag{5.13}$$

The charge density ρ is given by the number of antiprotons N and the total volume of the interferometer[2]

$$\rho = \frac{e\, N}{2\, L_T \cdot \pi\, r_\mathrm{b}^2} \ . \tag{5.14}$$

As the force on the outer antiprotons is the strongest, one sets $r = r_\mathrm{b}$ to examine the upper limit, which leads to

$$F = \frac{1}{\gamma^2} \cdot \frac{e^2\, N}{4\, \epsilon_0\, L_T\, \pi\, r_\mathrm{b}} \ . \tag{5.15}$$

For the energy range in question relativistic effects can be ignored ($1/\gamma^2 \approx 1$). The force due to inner beam interaction for the energy ranging from 100 eV to 100 keV is shown in figure 5.7 in comparison to the critical force. For the envisioned energy range of 1 keV and a hundred antiprotons within the interferometer this perturbing force is two orders of magnitude smaller than the critical limit. Following this simplified estimation, recording the fringe pattern with a single antiproton bunch seem possible and should be the goal of the first experimental attempt. If space charges turn out to be a limiting effect, one can reduce the flux and increase the measurement time. This can even be brought to the extreme of single antiprotons passing the interferometer making space charge effects irrelevant. This is further examined in the following section, which focuses on the antiproton source. It describes three experimental realisations of incrementally increasing complexity.

[2]The total length of the three grating interferometer is twice the Talbot length.

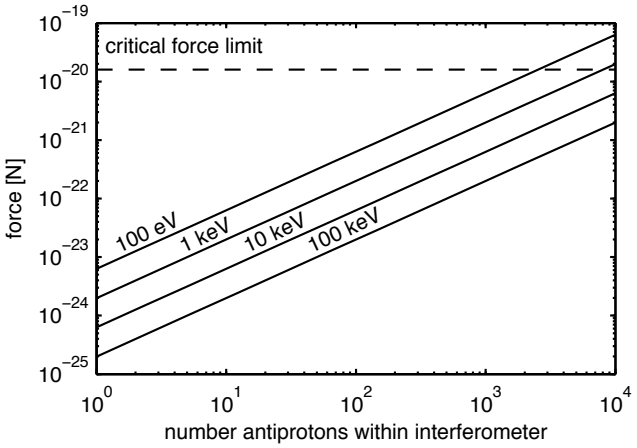

Figure 5.7.: The force due to space charge effects in dependency on the number of antiprotons within the interferometer. For the envisioned mean energy of 1 keV and 100 antiprotons, this force is two orders of magnitude smaller than the critical force limit where the interferometric pattern is smeared out. This means that it might be possible to record the pattern with a single antiproton bunch if a sufficient flux is reached.

5.5. Antiproton Source

The most minimalistic experimental realisation is depicted in figure 5.8a. The AD extraction ports have a vacuum separation foil to isolate the vacuum of the decelerator ring from the vacuum of the experiments. This titanium foil holds atmospheric pressure but is still so thin, that the vast majority of the antiproton bunch passes it. This allows one to place the interferometer inside an independent vacuum chamber with an identical foil as an entrance window. Consequently, the antiprotons pass a short air gap[3]. The common way[4] to decelerate antiprotons of 5.3 MeV coming from the AD is to place a thin degrading foil into the beam, which slows down the antiprotons via multiple scattering (compare to the degrading system described in section 3.1.2). The degrader foil is placed inside the air gap between the two vacuum chambers. The thickness of the degrader is critical as it affects the antiprotons' mean energy. It has the shape of a wedge such that its effective thickness can be tuned by translation of the foil. The energy distribution after such a degrader is very broad as seen in figure 3.13, but the AD's antiproton bunch length of 200 ns is very short. One can therefore envision to perform a time-of-flight measurement to separate the different velocity classes in the post selection to determine the individual visibility. A separation of 1 meter between degrading foil and detector results in a time-of-flight of 2.3 µs for the 1 keV antiprotons. A detector with temporal resolution in the order of the bunch length or better would imply relative energy resolution of $\sim 10\,\%$. An important advantage of this approach is that the large background of particles such as pions coming the degrader foil – most antiprotons annihilate within the

[3] In the first experiment that succeeded to trap antiprotons [132], the antiprotons travelled several centimetres through air.

[4] An exception is the ASACUSA experiment [133] which includes a RF decelerator.

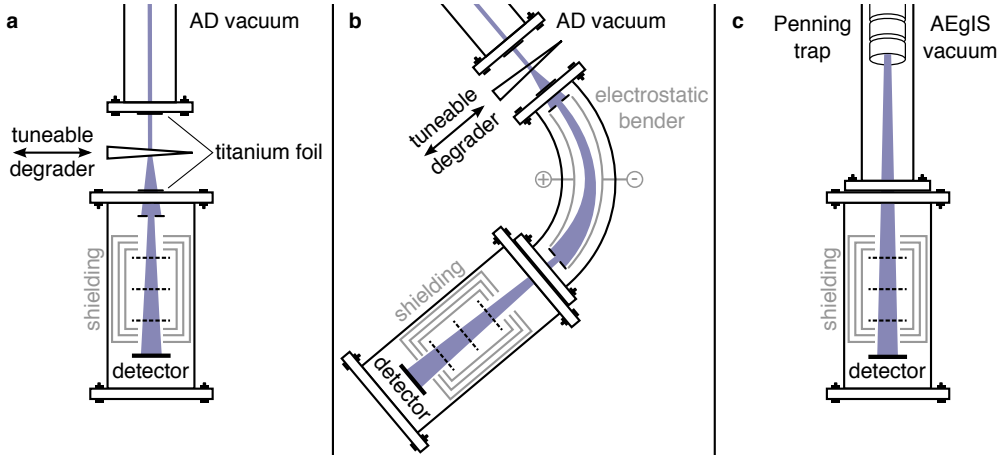

Figure 5.8.: Possible antiproton sources in order of increasing complexity. (a) Direct exposure of the interferometer with antiprotons from degrader foil. The velocity classes are separated via time-of-flight post selection. (b) An electrostatic bender as velocity selector. The mean energy is selected with the deflecting potential. (c) The antiprotons are primarily trapped, cooled and subsequently released using the Penning trap of the AEgIS main apparatus.

foil – have speeds approaching the speed of light. When the slow antiprotons arrive at the detector, the vast majority of the background is already gone.

A single, additional element placed in front of the interferometer (figure 5.8b) may allow a better velocity selection. Electrostatic benders [134] consisting of two curved plate electrodes can be used as a velocity selector. The voltage U applied to the electrodes and thus the field between the curved plates guides the charged particles on the radius r_0 if they have the matching energy

$$E_{\mathrm{kin}} = \frac{U\, r_0}{2\, d} \ , \tag{5.16}$$

where d represents the distance between the plates. Faster particles have a larger, and slower particles a smaller curvature radius and do not pass the exit aperture. The advantage of an electrostatic bender over its magnetic counterpart, is that electric fields can easily be shielded and one does not want to place an additional magnet in front of the magnetic shield.

It is interesting to note that neither of the experimental approaches described so far require the use of the main AEgIS apparatus. This can be seen as an advantage as it reduces complexity of the measuring apparatus. For example, the vacuum requirements for this experiment are very low. A vacuum pressure of 10^{-7} mbar to 10^{-8} mbar is certainly sufficient for the interferometer to work. If the interferometer is connected to the AEgIS apparatus, the vacuum requirements are naturally defined by the latter ($\approx 10^{-11}$ mbar) and necessitate a deliberate pumping strategy for the interferometer's chamber. On the other hand, the Penning traps and the cooling mechanism implemented in the main apparatus offer a high

level of control over the antiprotons. Using primarily trapped antiprotons (see figure 5.8c), which are subsequently cooled and released towards the interferometer would create a nearly monochromatic, tuneable beam. Additionally, a piecewise release of the antiprotons from the Penning trap allows the reduction of possible disturbing effects such as inner beam interaction. With a slow release in a time window of 50 µs, which is still faster than most acoustic vibrations of the interferometer, the antiprotons would spread over a length of 25 m. This would reduce the number of antiprotons within the interferometer - making space charge effects negligible. Pion background from the degrading foils is completely removed as the traps can hold the antiprotons for several seconds.

5.6. Requirements of the Detection System

The spatially resolving detector needs to work in vacuum and cover an area of $3 \times 3\,\mathrm{mm}^2$. To resolve three macroscopic fringes (see figure 5.3) with 10 bins per period, a single event resolution of around 100 µm is sufficient. The detector needs to distinguish antiproton annihilations from background pions and should be able to detect up to a hundred antiproton annihilations per AD bunch.

The amount of equipment within the interferometric volume (the volume between the gratings) has to be minimised to what is absolutely necessary. The only indispensable elements are the gratings and their actuators. The spatially resolving detector does not need to be placed directly behind the third grating and can even be placed outside the magnetic field shielding. The maximum distance L_D allowed between the last grating and the detector is limited by the divergence of the antiproton beam as it smears out the pattern. This effect can be estimated as follows: A total distance of 1 m from the degrader foil to the last grating and a grating with an edge length of 3 mm result in a divergence of approximately 3 mrad. The divergence multiplied with the distance between the last grating and the detector needs to be much smaller than the periodicity of the macroscopic fringe one wants to observe. For three fringes on the total detector surface (see figure 5.3), the spacing between two fringes is 1 mm, thus

$$L_D \ll \frac{1\,\mathrm{mm}}{3\,\mathrm{mrad}} \approx 330\,\mathrm{mm}\ . \tag{5.17}$$

Placing the detector at one tenth of this distance should insure that the pattern is not smeared out in the plane of the detector.

5.7. Discussion

Having access to the two key ingredients – slow antiprotons and gratings with extremely small grating periods – the demonstration of an interferometer for antimatter appears to be within reach. Several technical aspects need be addressed in more detail, in particular the detection system. Preliminary tests on the antiproton source and the various detection systems available within the AEgIS collaboration are needed to identify the best solution. While this experiment is of interest by itself, many of its aspects are similar to a possible

measurement with antihydrogen. One should note that the interferometer's inertial sensitivity is $2 \cdot 10^5$ times larger than the antiproton deflectometer (smaller gratings ≈ 200, three times longer ≈ 10 and lower energy ≈ 100). A realisation would therefore represent a significant leap forward towards the detection of gravitational acceleration of antihydrogen.

As all good things need to be named, the author deems the acronym 'AtliX' – Antimatter Talbot-Lau Interferometry eXperiment – to be an appropriate name.

All animals are equal, but some
animals are more equal than others.

(George Orwell)

6. Outlook and Conclusion

Much remains to be done to reach the goal of a 1 % measurement on $\bar{g}$ as envisioned by the AEgIS collaboration. The two most crucial steps to be taken are the new antihydrogen production method based on the charge-exchange reaction and the realisation of a cooling scheme that reaches an antihydrogen temperature below 1 K. The first antihydrogen atoms produced by this new machine will certainly have a higher temperature; however, one should use these antihydrogen atoms to lower the direct experimental limit, which is currently set by the ALPHA experiment [52]. For instance, one could intend to measure the sign of the gravitational acceleration. The following outlook outlines how such an interferometer *could* look like in order to show how methods discussed in the previous chapters increase the flexibility in designing such an experiment.

6.1. Outlook on Gravity

An emulsion detector cannot be used in the environment of the antihydrogen production trap, which is placed in ultra-high vacuum at 4 K. However, with a three-grating configuration as discussed in chapter 4, one is free to place such a device as close to the point of production as possible. This increases the solid angle and therefore the number of detected antihydrogen atoms. One could even consider to place the interferometer inside the superconducting magnet of the production trap, which has a field strength of 1 T. The antihydrogen atom is not susceptible to absolute fields, but remains susceptible to magnetic field gradients. As this magnet's field is axially symmetric, one can expect small transversal gradients on the central axis of the magnet, but increasing gradients for larger radii. Figure 6.1a depicts how the gradients of the magnetic field translate into a transversal acceleration of antihydrogen atoms in the ground state. This figure can be understood as follows: The magnetic field behind the production trap is computed for the coil configuration of the existing magnet of the AEgIS apparatus. The hyperfine splitting of ground state antihydrogen is shown in figure 6.1b as a function of the magnetic field. The two low-field and the two high-field seeking states experience an opposite acceleration for a given field gradient. This is used to compute figure 6.1a, which depicts the transversal acceleration on a radius of 6 mm as a function of the distance z from the production trap. Up to a distance of a 100 mm, the transversal acceleration is smaller than $2\,\mathrm{m\,s^{-2}}$; for radii smaller than 6 mm, the atoms

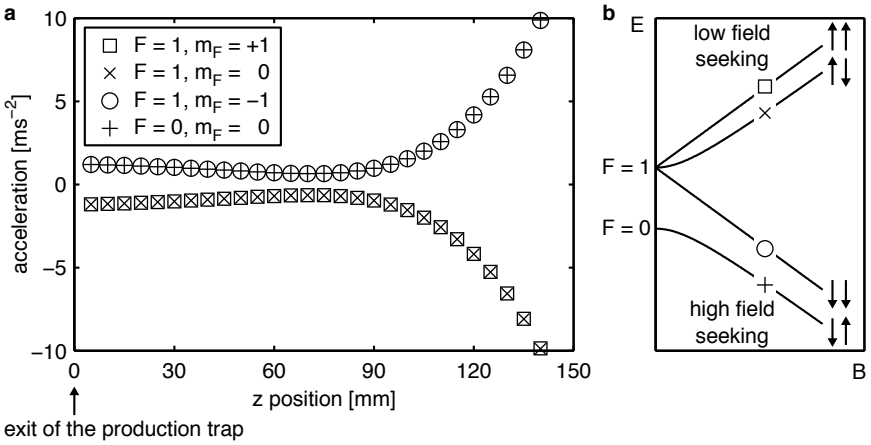

Figure 6.1.: Magnetic field gradients at the exit of the antihydrogen production trap cause a transversal acceleration of the antihydrogen atoms. (a) The transversal acceleration on a radius of 6 mm with respect to the magnet's central axis is smaller than one-fifth of the gravitational acceleration for a flight distance of ~ 100 mm. The acceleration for smaller radii is even smaller. (b) The hyperfine splitting of antihydrogen induces two low-field and two high-field seeking states, which experience opposite acceleration for a given magnetic field gradient. Courtesy of A. Demetrio.

experience an even smaller acceleration due to the magnetic field. Thus, one could consider this volume (100 mm in length and 12 mm in diameter) for an interferometer and presume an antihydrogen temperature of 5 K, which is below the temperatures reported by ALPHA, but 50 times hotter than the temperature AEgIS ultimately envisions to reach. The following considers the 'traditional' antihydrogen production scheme and a production rate that has been reported to work. The resulting mean velocity at that temperature can be estimated to $\bar{v} = \sqrt{8\,k_b T/\pi m} \approx 325\,\mathrm{m\,s^{-1}}$. A Talbot-Lau interferometer with a total length of a 100 mm results in a grating separation of $L = 50$ mm, which is chosen to correspond to one Talbot length. This requires a grating period of $d = \sqrt{L\,h/m\bar{v}} \approx 8\,\mu\mathrm{m}$. The critical acceleration at which the fringe pattern is completely smeared out follows with equation 5.6 to

$$a_{\mathrm{crit}} = \frac{h^2}{m^2 d^3} \approx 330\,\mathrm{m\,s^{-2}}\ , \tag{6.1}$$

which is 30 times larger than the gravitational acceleration. This makes the interferometer quite robust. However, the mere observation of a high-visibility fringe would limit the absolute value of the gravitational acceleration to a value below this number. From such an observation one could directly lower the current direct experimental limit [52] by an order of magnitude without having time-of-flight information or a light reference. The minimal detectable acceleration for this configuration follows as

$$a_{\mathrm{min}} = \frac{d\,\bar{v}^2}{2\pi\,\mathcal{V}\,L^2\sqrt{N_{\mathrm{det}}}} \approx \frac{65\,\mathrm{m\,s^{-2}}}{\sqrt{N_{\mathrm{det}}}} \overset{N_{\mathrm{det}}=500}{\approx} 3\,\mathrm{m\,s^{-2}}\ . \tag{6.2}$$

One could reach the level at which the systematics due to magnetic field gradients become significant with 500 detected ground state antihydrogen atoms. Assuming normal gravity,

a minimal detectable acceleration of $3\,\mathrm{m\,s^{-2}}$ corresponds to a relative precision of 30 %. The ALPHA experiment reports to produce 6000 atoms every ten minutes. Without the acceleration to form a beam, the atoms leave the point of production isotropically and the number of atoms flying in the direction of the interferometer is given by its solid angle, which is about $4.4 \cdot 10^{-3}$. Due to the open fraction η of the gratings, the fraction of atoms that passes the first two gratings is given by η^2. This results, on average, in 2.4 detectable atoms every ten minutes. One shift at the AD consists of eight hours of beam time, so that ~ 500 hits could be accumulated in five shifts.

While this discussion assumes a high temperature and a production scheme that has been shown to work, it assumes that all atoms are produced in the ground state, which is a simplification. In an approach where the interferometer is placed inside the superconducting magnet, it comes down to how well one understands the magnetic field and the state distribution of the produced antihydrogen atoms.

6.2. Conclusion

In the course of this thesis, tools from the field of atom optics were explored for their use with antimatter. The starting point was the moiré deflectometer, a classical device the AEgIS collaboration plans to use for a measurement of the gravitational acceleration of antihydrogen. Such a test of the weak equivalence principle represents a challenging experimental goal and sets high requirements to the antihydrogen source. Any improvement of the inertial sensitivity of the measuring apparatus reduces these requirements and is therefore of great importance to make such a measurement feasible. In this context, the extension of this classical tool to the wave regime, where it is known as Talbot-Lau interferometer, has shown to be a promising path and allows new, creative solutions to tackle this challenge. In a first experimental step, the deflection of antiprotons due to an electromagnetic force on the $\sim 500\,\mathrm{aN}$ level was measured with a device that is in the classical regime for antiprotons but in the wave regime for photons. Even though the sensitivity of this device was too small to measure gravity and the details of this realisation disclosed systematic errors, this preliminary test demonstrated three important aspects: Firstly, one can determine the sign of a force without having time-of-flight information on single events using an absolute reference based on light. Secondly, this absolute reference may allow the connection of data from different runs, a problem, for which no other solution has been identified so far. Finally, the mere observation of a high-visibility fringe pattern sets an upper bound on forces being present. This effect could be used to reduce the directly observed limits on the gravitational acceleration of antihydrogen.

The work with antimatter complicates many things. Especially the small numbers of detected events in future antihydrogen experiments will necessitate adequate statistical methods. Here, the Rayleigh test provides the means for efficient fringe detection. However, it was shown, that the use of antimatter opens up possibilities that are difficult to access with experiments based on ordinary matter. The annihilation of the antiproton for instance allows the unambiguous detection of single events with emulsions, which offer a very high spatial resolution of $\sim 2\,\mu\mathrm{m}$. Another example is the proposed detection and evaluation scheme that

allows the use of a third grating while still making efficient use of the particle flux. This approach requires the detection of the particles that are stopped by the third grating. For antiprotons (and antihydrogen), this can be achieved with a vertex-reconstructing detector.

The grating period turned out to be a parameter of great interest. Of all geometrical parameters it offers the biggest potential to improve the inertial sensitivity of the measuring apparatus. Additionally, it plays a central role in which regime the device operates – a Talbot-Lau interferometer for antihydrogen based on a three grating configuration may result in a higher inertial sensitivity than a moiré deflectometer. It would therefore be favourable to explore the wave regime with antimatter in the next experimental step. In this context, a Talbot-Lau interferometer for antiprotons appears technically feasible and timely.

One should go for it.

Bibliography

[1] G. Galilei. Discorsi e dimostrazioni matematiche intorno à due nuoue scienze. *Elsevirii*, 1638.

[2] G. Galilei. Dialogues Concerning Two New Sciences (translation by H. Crew and A. de Salvio). *Macmillan, New York*, 1914.

[3] I. Newton. *Philosophiæ Naturalis Principia Mathematica*. Jussu Societatis Regiæ ac Typis J. Streater, 1687.

[4] K. Kuroda and N. Mio. Test of a composition-dependent force by a free-fall interferometer. *Physical Review Letters*, 62(17):1941–1944, 1989.

[5] S. Fray, C. A. Diez, T. W. Hänsch, and M. Weitz. Atomic Interferometer with Amplitude Gratings of Light and Its Applications to Atom Based Tests of the Equivalence Principle. *Physical Review Letters*, 93(24), 2004.

[6] E. G. Adelberger, J. H. Gundlach, B. R. Heckel, S. Hoedl, and S. Schlamminger. Torsion balance experiments: a low-energy frontier of particle physics. *Progress in Particle and Nuclear Physics*, 62:102–134, 2009.

[7] J. G. Williams, S. G. Turyshev, and D. H. Boggs. Lunar laser ranging tests of the equivalence principle. *Classical and Quantum Gravity*, 29(18):184004, 2012.

[8] C. D. Anderson. The positive electron. *Physical Review*, 43(6):491, 1933.

[9] P. A. M. Dirac. The quantum theory of the electron. *Proceedings of the Royal Society of London. Series A, Containing Papers of a Mathematical and Physical Character*, pages 610–624, 1928.

[10] P. Morrison. Approximate nature of physical symmetries. *American Journal of Physics*, 26:358–368, 1958.

[11] L. I. Schiff. Sign of the gravitational mass of a positron. *Physical Review Letters*, 1:254–255, 1958.

[12] L. I. Schiff. Gravitational properties of antimatter. *Proceedings of the National Academy of Sciences*, 45:69–80, 1959.

[13] R. J. Hughes and M. H. Holzscheiter. Constraints on the gravitational properties of antiprotons and positrons from cyclotron-frequency measurements. *Physical Review Letters*, 66(7):854–857, 1991.

[14] M. L. Good. K_2^0 and the Equivalence Principle. *Physical Review*, 121:311–313, 1961.

[15] A. Apostolakis et al. Tests of the equivalence principle with neutral kaons. *Physics Letters B*, 452:425–433, 1999.

[16] E. G. Adelberger, B. R. Heckel, C. W. Stubbs, and Y. Su. Does antimatter fall with the same acceleration as ordinary matter? *Physical Review Letters*, 66:850–853, 1991.

[17] J. M. LoSecco. The case for neutrinos from SN 1987a. *Physical Review D*, 39:1013–1019, 1989.

[18] T. Goldman, M. V. Hynes, and M. M. Nieto. The gravitational acceleration of antiprotons. *General Relativity and Gravitation*, 18:67–70, 1986.

[19] Michael Martin Nieto and T. Goldman. The arguments against "antigravity" and the gravitational acceleration of antimatter. *Physics Reports*, 205(5):221–281, 1991.

[20] M. Fischler, J. Lykken, and T. Roberts. Direct observation limits on antimatter gravitation. *arXiv*, 2008.

[21] M. M. Nieto, T. Goldman, J. D. Anderson, E. L. Lau, and J. Pérez-Mercader. Theoretical Motivation for Gravitation Experiments on Ultra-Low Energy Antiprotons and Antihydrogen. *arXiv*, 1994.

[22] G. Chardin. Motivations for antigravity in General Relativity. *Hyperfine Interactions*, 109:83–94, 1997.

[23] T. Goldman and M. M. Nieto. Gravitational properties of antimatter. In Ugo Gastaldi, editor, *Physics with antiprotons at LEAR in the ACOL era*, pages 639–648. Editions Frontières, Gif-sur-Yvette, 1985.

[24] F. C. Witteborn and W. M. Fairbank. Experimental comparison of the gravitational force on freely falling electrons and metallic electrons. *Physical Review Letters*, 19(18):1049, 1967.

[25] M. H. Holzscheiter et al. Trapping of antiprotons in a large penning trap—progress towards a measurement of the gravitational acceleration of the antiproton. *Nuclear Physics A*, 558:709–718, 1993.

[26] M. Amoretti et al. (ATHENA collaboration). Production and detection of cold antihydrogen atoms. *Nature*, 419(6906):456–459, 2002.

[27] G. Gabrielse et al. (ATRAP collaboration). Driven production of cold antihydrogen and the first measured distribution of antihydrogen states. *Physical Review Letters*, 89(23):233401, 2002.

[28] G. Drobychev et al. (AEgIS collaboration). Proposal for the AEgIS experiment at the CERN Antiproton Decelerator. *SPSC-P-334; CERN-SPSC-2007-017*, 2007.

[29] P. Perez. The gbar experiment: gravitational behaviour of antihydrogen at rest. *Classical and Quantum Gravity*, 29:184008, 2012.

[30] P. Hamilton et al. Antimatter interferometry for gravity measurements. *Physical Review Letters*, 112(12), 2014.

[31] D. B. Cassidy and S. D. Hogan. Atom control and gravity measurements using rydberg positronium. In *International Journal of Modern Physics: Conference Series*, volume 30. World Scientific, 2014.

[32] K. Kirch. Testing gravity with muonium. arXiv, 2013.

[33] D. Keith. Diffraction of atoms by a transmission grating. *Physical Review Letters*, 61(14):1580–1583, 1988.

[34] O. Carnal and J. Mlynek. Young's double-slit experiment with atoms: A simple atom interferometer. *Physical Review Letters*, 66(21):2689–2692, May 1991.

[35] D. W. Keith, C. R. Ekstrom, Q. A. Turchette, and D. E. Pritchard. An interferometer for atoms. *Physical Review Letters*, 66(21):2693–2696, 1991.

[36] M. S. Chapman et al. Near-field imaging of atom diffraction gratings: The atomic Talbot effect. *Physical Review A*, 51:R14–R17, 1995.

[37] S. Nowak, Ch. Kurtsiefer, T. Pfau, and C. David. High-order Talbot fringes for atomic matter waves. *Optics letters*, 22(18):1430–1432, 1997.

[38] M. K. Oberthaler. Inertial sensing with classical atomic beams. *Physical Review A*, 54(4):3165–3176, 1996.

[39] B. Brezger et al. Matter-Wave Interferometer for Large Molecules. *Physical Review Letters*, 88(10), 2002.

[40] P. Haslinger et al. A universal matter-wave interferometer with optical ionization gratings in the time domain. *Nature Physics*, 9(3):144–148, 2013.

[41] D. Schlippert et al. Quantum test of the universality of free fall. *Physical Review Letters*, 112(20):203002, 2014.

[42] A. Sugarbaker, S. M. Dickerson, J. M. Hogan, D. M. S. Johnson, and M. A. Kasevich. Enhanced atom interferometer readout through the application of phase shear. *Physical Review Letters*, 111(11):113002, 2013.

[43] S. M. Dickerson, J. M. Hogan, A. Sugarbaker, D. M. S. Johnson, and M. A. Kasevich. Multiaxis inertial sensing with long-time point source atom interferometry. *Physical Review Letters*, 111(8):083001, 2013.

[44] T. van Zoest et al. Bose-einstein condensation in microgravity. *Science*, 328(5985):1540–1543, 2010.

[45] H. Müntinga et al. Interferometry with bose-einstein condensates in microgravity. *Physical Review Letters*, 110(9):093602, 2013.

[46] G. Varoquaux et al. How to estimate the differential acceleration in a two-species atom interferometer to test the equivalence principle. *New Journal of Physics*, 11(11):113010, 2009.

[47] G. Gabrielse et al. Cooling and slowing of trapped antiprotons below 100 mev. *Physical Review Letters*, 63(13):1360, 1989.

[48] G. Gabrielse et al. Thousandfold improvement in the measured antiproton mass. *Physical Review Letters*, 65(11):1317, 1990.

[49] G. Gabrielse et al. Precision mass spectroscopy of the antiproton and proton using simultaneously trapped particles. *Physical Review Letters*, 82(16):3198–3201, 1999.

[50] R. J. Hughes. New test of the equivalence principle for the antiproton. *Physical Review D*, 46(6):R2283, 1992.

[51] J. Walz and T. W. Hänsch. A proposal to measure antimatter gravity using ultracold antihydrogen atoms. *General Relativity and Gravitation*, 36(3):561–570, 2004.

[52] The ALPHA Collaboration and A. E. Charman. Description and first application of a new technique to measure the gravitational mass of antihydrogen. *Nature Communincations*, 4:1785, 2013.

[53] G. B. Andresen et al. Trapped antihydrogen. *Nature*, 468(7324):673–676, 2010.

[54] Alpha Collaboration et al. Confinement of antihydrogen for 1,000 seconds. *Nature Physics*, 7(7):558–564, 2011.

[55] P. R. Berman, editor. *Atom Interferometry*. Academic Press, 1997.

[56] A. Stibor, K. Hornberger, L. Hackermüller, A. Zeilinger, and M. Arndt. Talbot-Lau Interferometry with Fullerenes: Sensitivity to Inertial Forces and Vibrational Dephasing. *Laser Physics*, 15(1):10–17, 2005.

[57] M. Doser. Exploring the WEP with a pulsed cold beam of antihydrogen. *Classical Quant. Grav.*, 29:184009, 2012.

[58] A. Kellerbauer. Proposed antimatter gravity measurement with an antihydrogen beam. *Nuclear Instruments and Methods in Physics Research Section B*, 266:351–356, 2008.

[59] G. Consolati, R. Ferragut, A. Galarneau, F. Di Renzo, and F. Quasso. Mesoporous materials for antihydrogen production. *Chemical Society Reviews*, 42(9):3821–3832, 2013.

[60] S. Cialdi et al. Efficient two-step positronium laser excitation to rydberg levels. *Nuclear Instruments and Methods in Physics Research Section B:*, 269(13):1527–1533, 2011.

[61] Ch. Seiler, S. D. Hogan, H. Schmutz, J. A. Agner, and F. Merkt. Collisional and radiative processes in adiabatic deceleration, deflection, and off-axis trapping of a rydberg atom beam. *Physical Review Letters*, 106(7):073003, 2011.

[62] E. Vliegen, S. D. Hogan, H. Schmutz, and F. Merkt. Stark deceleration and trapping of hydrogen rydberg atoms. *Physical Review A*, 76(2):023405, 2007.

[63] E. Vliegen and F. Merkt. Stark deceleration of hydrogen atoms. *Journal of Physics B*, 39(11):L241–L247, 2006.

[64] K. Hornberger, J. E. Sipe, and M. Arndt. Theory of decoherence in a matter wave Talbot-Lau interferometer. *Physical Review A*, 70(5), 2004.

[65] J. Jahns, A.W. Lohmann, and J. Ojeda-Castañeda. Talbot and Lau Effects, a Para-geometrical Approach. *Optica Acta: International Journal of Optics*, 31(3):313–324, 1984.

[66] Ch. Siegel, F. Loewenthal, and J. E. Balmer. A wavefront sensor based on the fractional Talbot effect. *Optics Communications*, 194:265 – 275, 2001.

[67] M. V. Berry and S. Klein. Integer, fractional and fractal Talbot effects. *Journal of modern optics*, 43(10):2139–2164, 1996.

[68] B. Dubetsky and P. R. Berman. Creating and probing subwavelength atomic gratings using spatially separated fields. *Physical Review A*, 50(5):4057, 1994.

[69] F. C. Haupert. *A Moiré-Deflectometer as Gravimeter for Antihydrogen.* PhD thesis, Heidelberg University, 2012.

[70] H. Filter. Methoden zur Flussbestimmung von metastabilen Argonatomen. Master's thesis, Heidelberg University, 2011.

[71] F. Bergermann. Characterization of the Moiré Deflectometer for the AEgIS-Experiment. Master's thesis, Heidelberg University, 2012.

[72] Tobias M. Wintermantel. Measurement of Gravity using a Moiré Deflectometer for metastable Argon Atoms. Bachelor thesis, 2013.

[73] H. F. Talbot. Facts relating to Optical Science No IV. *Philosophical Magazine Series 3*, 9(56):401–407, 1836.

[74] Lord Rayleigh. On copying diffraction-gratings, and on some phenomena connected therewith. *Philosophical Magazine Series 5*, 11(67):196–205, 1881.

[75] E. Lau. Beugungserscheinungen an Doppelrastern. *Annalen der Physik*, 437:417–423, 1948.

[76] M. Tomandl. Realisierung von optischen Talbot- und Talbot-Lau-Teppichen. Master's thesis, University of Vienna, 2010.

[77] W. B. Case, M. Tomandl, S. Deachapunya, and M. Arndt. Realization of optical carpets in the Talbot and Talbot-Lau configurations. *Optics Express*, 17(23), 2009.

[78] R. Bach, G. Gronniger, and H. Batelaan. An electron Talbot-Lau interferometer and magnetic field sensing. *Applied Physics Letters*, 103(25), 2013.

[79] J. F. Clauser and S. Li. Talbot-von Lau atom interferometry with cold slow potassium. *Physical Review A*, 49:R2213–R2216, 1994.

[80] M. R. Dennis, N. I. Zheludev, and F. J. García de Abajo. The plasmon Talbot effect. *Optics express*, 15(15):9692–9700, 2007.

[81] S. Cherukulappurath et al. Local observation of plasmon focusing in Talbot carpets. *Optics express*, 17(26):23772–23784, 2009.

[82] W. Zhang, C. Zhao, J. Wang, and J. Zhang. An experimental study of the plasmonic Talbot effect. *Optics express*, 17(22):19757–19762, 2009.

[83] B. Brezger, M. Arndt, and A. Zeilinger. Concepts for near-field interferometers with large molecules. *Journal of Optics B*, 5(2), 2003.

[84] K. H. Brenner. Computational optics. Seminar at Heidelberg University.

[85] M. K. Kim. *Digital holographic microscopy: principles, techniques, and applications*, volume 162. Springer, 2011.

[86] E. Wigner. On the Quantum Correction For Thermodynamic Equilibrium. *Physical Review*, 40(5):749–759, 1932.

[87] W. Heisenberg. Über den anschaulichen Inhalt der quantentheoretischen Kinematik und Mechanik. *Zeitschrift für Physik*, 43(3-4):172–198, 1927.

[88] P. Bräunig. Analytical estimation of the deflectometer's performance. Internal Note of AEgIS collaboration, 2014.

[89] S. Aghion et al. A moiré deflectometer for antimatter. *Nature Communincations*, 5, 2014.

[90] R. L. Golden et al. Search for antihelium in the cosmic rays. *The Astrophysical Journal*, 479(2):992, 1997.

[91] J. Alcaraz et al. (AMS collaboration). Search for antihelium in cosmic rays. *Physics Letters B*, 461(4):387–396, 1999.

[92] R. Colella and A. W. Overhauserand S. A. Werner. Observation of gravitationally induced quantum interference. *Physical Review Letters*, 34(23):1472–1474, 1975.

[93] O. Chamberlain et al. On the observation of an antiproton star in emulsion exposed at the bevatron. *Nuovo Cimento*, 3:447–467, 1956.

[94] N. Agafonova et al. (OPERA collaboration). Observation of a first ν_τ candidate event in the OPERA experiment in the CNGS beam. *Physics Letters B*, 691:138–145, 2010.

[95] S. Aghion et al. (AEgIS collaboration). Prospects for measuring the gravitational free-fall of antihydrogen with emulsion detectors. *Journal of Instrumentation*, 8:P08013, 2013.

[96] C. Amsler et al. A new application of emulsions to measure the gravitational force on antihydrogen. *JINST*, 8:P02015, 2013.

[97] M. Kimura et al. A new method to correct deformations in emulsion using a precise photomask. *Nuclear Instruments and Methods in Physics Research Section A*, 711:1–7, 2013.

[98] Lord Rayleigh. On the problem of Random Vibrations, and of Random Flights in one, two, or three Dimensions. *Philosophical Magazine*, 37(6):321–347, 1919.

[99] R. J. Beran. Asymptotic Theory of a Class of Tests for Uniformity of a Circular Distribution. *The Annals of Mathematical Statistics*, 40(4):1196–1206, 1969.

[100] K.V. Mardia. *Statistics of directional data*. Probability and mathematical statistics. Academic Press, 1972.

[101] L. Guillemot. Statistical analysis 1. HTRA Autumn School, 2011.

[102] W. Wiltschko and R. Wiltschko. Magnetic compass of european robins. *Science*, 176(4030):62–64, 1972.

[103] S. Engels. Anthropogenic electromagnetic noise disrupts magnetic compass orientation in a migratory bird. *Nature*, 509(7500):353–356, 2014.

[104] A. I. Gibson et al. Transient emission of ultra-high energy pulsed γ rays from Crab pulsar PSR0531. *Nature*, 296(5860):833–835, 1982.

[105] R. Buccheri et al. Search for pulsed gamma-ray emission from radio pulsars in the COS-B data. *Astronomy and Astrophysics*, 128:245–251, 1983.

[106] D. A. Leathy, R. F. Elsner, and M. C. Weisskopf. On searches for periodic pulsed emission: The Rayleigh test compared to epoch folding. *The Astronomical Journal*, 272:256–258, 1983.

[107] M. P. Muno. X-ray Sources with Periodic Variability in a Deep Chandra Image of the Galactic Center. *The Astronomical Journal*, 599:465–474, 2003.

[108] S. Agostinelli et al. Geant - a simulation toolkit. *Nuclear Instruments and Methods in Physics Research A*, 506(3):250–303, 2003.

[109] H. Rauch, W. Treimer, and U. Bonse. Test of a single crystal neutron interferometer. *Physics Letters A*, 47(5):369–371, 1974.

[110] J. Storey et al. (AEgIS collaboration). Particle tracking at 4K: The Fast Annihilation Cryogenic Tracking (FACT) detector for the AEgIS antimatter gravity experiment. *Nuclear Instruments and Methods in Physics Research Section A*, 732:437–441, 2013.

[111] K. Bosch. *Elementare Einführung in die angewandte Statistik*. Viewig, 5. edition, 1995.

[112] W. T. Eadie, D. Dryard, F. E. James, M. Roos, and B. Sadoulet. *Statisctical Methods*. North-Holland, 1971.

[113] P. Bräunig, J. Storey, and M. K. Oberthaler. AtliX: Antimatter Talbot-Lau Interferometry Experiment. Internal Proposal of the AEgIS collaboration, 2014.

[114] T. J. Phillips. Antimatter gravity studies with interferometry. *Hyperfine Interactions*, 109(1-4):357–365, 1997.

[115] M. K. Oberthaler. Anti-matter wave interferometry with positronium. *Nuclear Instruments and Methods in Physics Research B*, 192:129–134, 2002.

[116] Sandra Eibenberger, Stefan Gerlich, Markus Arndt, Marcel Mayor, and Jens Tüxen. Matter-wave interference of particles selected from a molecular library with masses exceeding 10000 amu. *Physical Chemistry Chemical Physics*, 15(35):14696–14700, 2013.

[117] C. Jönsson. Elektroneninterferenzen an mehreren künstlich hergestellten Feinspalten. *Zeitschrift für Physik*, 161(4):454–474, 1961.

[118] Manfred Gruber, Kurt Eder, Anton Zeilinger, Roland Gähler, and Walter Mampe. A phase-grating interferometer for very cold neutrons. *Physics Letters A*, 140(7-8):363 – 367, 1989.

[119] F. Riehle, Th. Kisters, A. Witte, J. Helmcke, and Ch. J. Bordé. Optical ramsey spectroscopy in a rotating frame: Sagnac effect in a matter-wave interferometer. *Physical Review Letters*, 67(2):177–180, Jul 1991.

[120] M. Kasevich and S. Chu. Atomic interferometry using stimulated Raman transitions. *Physical Review Letters*, 67(2):181–184, Jul 1991.

[121] E. Rasel. Atom wave interferometry with diffraction gratings of light. *Physical Review Letters*, 75(14):2633–2637, 1995.

[122] B. Barwick G. Gronniger and H. Batelaan. A three-grating electron interferometer. *New Journal of Physics*, 8(224), 2006.

[123] A. D. Cronin and B. McMorran. Electron interferometry with nanogratings. *Physical Review A*, 74:061602, 2006.

[124] F. Hasselbach. Progress in electron- and ion-interferometry. *Reports on Progress in Physics*, 73, 2010.

[125] A. D. Cronin, J. Schmiedmayer, and D. E. Pritchard. Optics and interferometry with atoms and molecules. *Reviews of Modern Physics*, 81(3):1051, 2009.

[126] U. Maier. *Ein Biprisma Interferometer für Ionen.* PhD thesis, Eberhard-Karls-Universität Tübingen, 1997.

[127] G. Schütz et. al. Biprism electron interferometry with a single atom tip source. arXiv, 2013.

[128] G. Schütz, A. Rembold, A. Pooch, and A. Stibor. An ion interferometer for the measurement of the electric Aharonov-Bohm effect. arXiv, 2013.

[129] B. Neyenhuis, D. Christensen, and D. S. Durfee. Testing nonclassical theories of electromagnetism with ion interferometry. *Physical Review Letters*, 99(20), 2007.

[130] D. Budker and D. F. Jackson Kimball, editors. *Optical Magnetometry.* Cambridge University Press, 2013.

[131] M. Ferrario. Space charge effects. CERN accelerator school, 2003.

[132] G. Gabrielse et al. First capture of antiprotons in a penning trap: a kiloelectronvolt source. *Physical Review Letters*, 57(20):2504, 1986.

[133] N. Kuroda et al. A source of antihydrogen for in-flight hyperfine spectroscopy. *Nature Communications*, 5, 2014.

[134] H. Kreckel et al. A simple double-focusing electrostatic ion beam deflector. *Review of Scientific Instruments*, 81(6), 2010.

[135] J. A. Greenwood and D. Durand. The Distribution of Length and Components of the Sum of n Random Unit Vectors. *The Annals of Mathematical Statistics*, 26(2):233–246, 1955.

[136] D. Wilkie. Rayleigh Test for Randomness of Circular Data. *Applied Statistics*, 32(3):311–312, 1983.

A. Derivation and P-Values of the Rayleigh Test

This section provides a brief derivation [99–101] of the Rayleigh test and its P-values and can be regarded as supplementary information to complete its discussion. Let $(\theta_1, \theta_2, ..., \theta_n)$ be a set of n independent realisations of a random variable on a circle C. The null hypothesis H_0 (no periodic signal) is tested against the alternative H_A (a periodic signal is present):

$$H_0 : p = 0 \quad \text{against} \quad H_\mathrm{A} : p > 0 \ . \tag{A.1}$$

$p = 0, ..., 1$ denotes signal strength [101] of a periodic function $f_s(\theta)$ over uniform noise, so that the observed signal can be described as

$$f(\theta) = p \cdot f_s(\theta) + \frac{1-p}{2\pi} \ . \tag{A.2}$$

For $p = 1$ one observes only the periodic function $f_s(\theta)$ and for $p = 0$ one observes only flat noise. A measure of distance between the resulting function $f(\theta)$ and a uniform density $g(x) = 1/2\pi$ on a circle is given by the Beran statistics [99]:

$$\Psi(f) = \int_0^{2\pi} \left(f(\theta) - \frac{1}{2\pi} \right)^2 \mathrm{d}\theta = p^2 \int_0^{2\pi} \left(f_s(\theta) - \frac{1}{2\pi} \right)^2 \mathrm{d}\theta \ . \tag{A.3}$$

For $\Psi(f)$ follows $\Psi(f) \to 0$ for $p \to 0$ and $\Psi(f) = 0$ for $f_s = 1/2\pi$. One can reject the null hypothesis H_0 when $\Psi(f)$ is large [99, 101]. A probability density function (pdf) to be tested can be represented as Fourier series

$$f(\theta) = \frac{1}{2\pi} \sum_{p=-\infty}^{\infty} \phi_p \, e^{-i\,p\,\theta} \tag{A.4}$$

with the Fourier coefficients

$$\phi_p = \int_0^{2\pi} e^{i\,p\,\theta} f(\theta) \mathrm{d}\theta \ , \tag{A.5}$$

which in circular statistics are referred to as trigonometric moments [100]. For these coefficients follows $\phi_0 = 1$ as the distribution is normalised and $\phi_p^* = \phi_{-p}$. This can be used to rewrite

$$\begin{aligned} f(\theta) &= \frac{1}{2\pi}\left[1 + 2\sum_{p=1}^{\infty} \phi_p\, e^{-i\,p\,\theta}\right] \\ &= \frac{1}{2\pi}\left[1 + 2\sum_{p=1}^{\infty} \alpha_p \cos(p\,\theta) + \beta_p \sin(p\,\theta)\right] \end{aligned} \tag{A.6}$$

with

$$\alpha_p = \frac{1}{n}\sum_{i=1}^{m} \cos(p\,\theta_i) \quad \text{and} \quad \beta_p = \frac{1}{n}\sum_{i=1}^{m} \sin(p\,\theta_i)\ . \tag{A.7}$$

Limiting the Fourier series to the first order results in

$$f_1(\theta) = \frac{1}{2\pi}\left[1 + 2\,\alpha_1 \cos(\theta) + 2\,\beta_1 \sin(\theta)\right]\ , \tag{A.8}$$

which allows the evaluation of the integral in equation A.3

$$\begin{aligned} \Psi(f_1) &= \int_0^{2\pi} \left(f_1(\theta) - \frac{1}{2\pi}\right)^2 \mathrm{d}\phi \\ &= \int_0^{2\pi} \left(\frac{1}{2\pi}\left(1 + 2\,\alpha_1 \cos(\theta) + 2\,\beta_1 \sin(\theta)\right) - \frac{1}{2\pi}\right)^2 \mathrm{d}\theta \\ &= \frac{1}{(2\pi)^2}\int_0^{2\pi} \left(2\,\alpha_1^2\,\cos^2(\theta) + 8\,\alpha_1\beta_1 \cos(\theta)\sin(\theta) + 2\,\beta_1^2\,\sin^2(\theta)\right) \mathrm{d}\theta \\ &= \frac{1}{(2\pi)^2}\left(4\pi\,\alpha_1^2 + 4\pi\,\beta_1^2\right) = \frac{\alpha_1^2 + \beta_1^2}{\pi} = \frac{L_1^2}{\pi} \end{aligned} \tag{A.9}$$

where

$$L_1 = \sqrt{\alpha_1^2 + \beta_1^2} = \sqrt{\left(\frac{1}{n}\sum_{i=1}^{n} \cos(\theta_i)\right)^2 + \left(\frac{1}{n}\sum_{i=1}^{n} \sin(\theta_i)\right)^2}$$

is the length of the added vectors $v_i = (\cos(\theta_i), \sin(\theta_i))$. As one is only trying to maximise L, normalisation is not critical. Nevertheless, L_1^2 is usually multiplied with $2n$ so the Rayleigh test is in line [101] with χ^2 with 2 degrees of freedom for large n ($n > 100$). Thus, the Rayleigh test has the final form:

$$Z^2 = 2nL_1^2 = \frac{2}{n}\left[\left(\sum_{i=1}^{n} \cos\left(\theta_i\right)\right)^2 + \left(\sum_{i=1}^{n} \sin\left(\theta_i\right)\right)^2\right]\ . \tag{A.10}$$

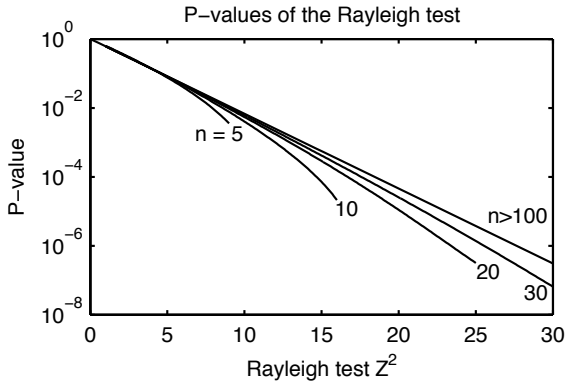

Figure A.1.: The P-value of the Rayleigh test is the probability that the null hypothesis of no periodic signal being present is true.

The orientation angle and periodicity of the antiproton fringe pattern can be extracted unambiguously, as clear peaks are visible in figure 3.5. In cases where the presence of a periodicity or a fringe pattern is in doubt (for example in future antihydrogen measurements), the corresponding P-values of Z^2 can be calculated to estimate the probability of such a signal. For datasets with more than a hundred events, this is given by

$$P(Z^2) = e^{-\frac{Z^2}{2}} \ . \tag{A.11}$$

For less than a hundred data points one can use the approximation derived by Greenwood and Durand [135, 136] with $K = Z^2/2$:

$$P\left(Z^2\right) = e^{-K} \cdot \left[1 + \frac{2K - K^2}{4n} - \frac{24K - 132K^2 + 76K^3 - 9K^4}{288n^2} - \frac{1440K + 1440K^2 - 8280K^3 + 4890K^4 - 870K^5 + 45K^6}{17280n^3}\right] \ . \tag{A.12}$$

B. Constants

Constants used in this thesis are listed in the following table.

constant	symbol	value
Planck constants	$\hbar$	$1.0546 \cdot 10^{-34}\,\mathrm{J\,s}$
	h	$\hbar \cdot 2\pi$
Boltzmann constant	k_b	$1.3087 \cdot 10^{-23}\,\mathrm{J\,K^{-1}}$
speed of light	c	$299\,792\,458\,\mathrm{m\,s^{-1}}$
standard acceleration of gravity	g	$9.806\,65\,\mathrm{m\,s^{-2}}$

C. Acknowledgements

This section is dedicated to those whose support have made this work possible. I am deeply grateful to

- Prof. Dr. Oberthaler for supervising my thesis and being such an inspiring and motivating mentor.
- Prof. Dr. Uwer for taking the time to evaluate and grade my thesis.
- Dr. M. Doser and Dr. G. Testera for their support.
- the members of the matterwave group and the AEgIS collaboration for making the last years such a fun ride.
- the members of the LHEP group from the University of Bern for the great help with the emulsion detector, especially Prof. Dr. Ereditato, Prof. Dr. C. Amsler and Prof. P. Scampoli, Dr. M. Kimura, Dr. A. Ariga, Dr. T. Ariga, Dr. C. Pistillo and Dr. J. Kawada.
- the board members of the IMPRS-PTFS for the many interesting seminars and granting me a stipend for the first months of my thesis.
- Dr. J. Storey for the fruitful discussions on interferometry with antimatter and Dr. D. Krasnický for having answers to all my questions about the AEgIS apparatus.
- D. Hufnagel and C. Jäger for the best team assistance.
- J. Schölles for his insights in electronics and yoga and S. Spiegel for the introduction to the workshop.
- the staff of the KIP workshop for the ongoing support. Special thanks to W. Lamade and M. Weißer.
- Dr. G. Bonomi for his work on the Geant4 simulations and A. Demetrio for interesting discussions.

- Dr. A. Kellerbauer for his etymological awareness and E. Jordan for her work on electrostatic benders.
- T. Wintermantel, F. Bergermann , H. Filter, J. Kohlrus and F. Haupert for their support in the lab.
- C. Kaup for the elements of style.
- my parents and sisters for being there and S. Trick for being a part of my life.

D. A moiré deflectometer for antimatter

This appendix contains a printout of a publication on which the author of this thesis is the corresponding author: S. Aghion et al. A moiré deflectometer for antimatter. Nature Communincations, 5:4538, doi: 10.1038/ncomms5538, (2014).

nature COMMUNICATIONS

ARTICLE

Received 5 Nov 2013 | Accepted 27 Jun 2014 | Published 28 Jul 2014

DOI: 10.1038/ncomms5538 OPEN

A moiré deflectometer for antimatter

S. Aghion[1,2], O. Ahlén[3], C. Amsler[4], A. Ariga[4], T. Ariga[4], A.S. Belov[5], K. Berggren[3], G. Bonomi[6,7], P. Bräunig[8], J. Bremer[3], R.S. Brusa[9], L. Cabaret[10], C. Canali[11], R. Caravita[2,12], F. Castelli[2,12], G. Cerchiari[13], S. Cialdi[2,12], D. Comparat[10], G. Consolati[1,2], H. Derking[3], S. Di Domizio[14], L. Di Noto[9], M. Doser[3], A. Dudarev[3], A. Ereditato[4], R. Ferragut[1,2], A. Fontana[7], P. Genova[7], M. Giammarchi[2], A. Gligorova[15], S.N. Gninenko[5], S. Haider[3], T. Huse[16], E. Jordan[13], L.V. Jørgensen[3], T. Kaltenbacher[3], J. Kawada[4], A. Kellerbauer[13], M. Kimura[4], A. Knecht[3], D. Krasnický[1,14], V. Lagomarsino[14,17], S. Lehner[18], A. Magnani[7,19], C. Malbrunot[3,18], S. Mariazzi[9,18], V.A. Matveev[5,20], F. Moia[1,2], G. Nebbia[21], P. Nédélec[22], M.K. Oberthaler[8], N. Pacifico[15], V. Petràček[23], C. Pistillo[4], F. Prelz[2], M. Prevedelli[24], C. Regenfus[11], C. Riccardi[7,19], O. Røhne[16], A. Rotondi[7,19], H. Sandaker[15], P. Scampoli[4,25], J. Storey[4], M.A. Subieta Vasquez[6,7], M. Špaček[23], G. Testera[14], R. Vaccarone[14], E. Widmann[18], S. Zavatarelli[14] & J. Zmeskal[18]

The precise measurement of forces is one way to obtain deep insight into the fundamental interactions present in nature. In the context of neutral antimatter, the gravitational interaction is of high interest, potentially revealing new forces that violate the weak equivalence principle. Here we report on a successful extension of a tool from atom optics—the moiré deflectometer—for a measurement of the acceleration of slow antiprotons. The setup consists of two identical transmission gratings and a spatially resolving emulsion detector for antiproton annihilations. Absolute referencing of the observed antimatter pattern with a photon pattern experiencing no deflection allows the direct inference of forces present. The concept is also straightforwardly applicable to antihydrogen measurements as pursued by the AEgIS collaboration. The combination of these very different techniques from high energy and atomic physics opens a very promising route to the direct detection of the gravitational acceleration of neutral antimatter.

[1] Politecnico di Milano, Piazza Leonardo da Vinci 32, 20133 Milan, Italy. [2] Istituto Nazionale di Fisica Nucleare, Sez. di Milano, Via Celoria 16, 20133 Milan, Italy. [3] Physics Department, European Organisation for Nuclear Research, 1211 Geneva 23, Switzerland. [4] Laboratory for High Energy Physics, Albert Einstein Center for Fundamental Physics, University of Bern, 3012 Bern, Switzerland. [5] Institute for Nuclear Research of the Russian Academy of Sciences, Moscow 117312, Russia. [6] Department of Mechanical and Industrial Engineering, University of Brescia, Via Branze 38, 25133 Brescia, Italy. [7] Istituto Nazionale di Fisica Nucleare, Sez. di Pavia, Via Agostino Bassi 6, 27100 Pavia, Italy. [8] Kirchhoff Institute for Physics, Heidelberg University, Im Neuenheimer Feld 227, 69120 Heidelberg, Germany. [9] Department of Physics, University of Trento and TIFPA-INFN, Via Sommarive 14, 38123 Povo, Trento, Italy. [10] Laboratoire Aimé Cotton, CNRS, University of Paris-Sud, ENS Cachan, Bâtiment 505, Campus d'Orsay, 91405 Orsay, France. [11] Physics Institute, University of Zurich, Winterthurerstrasse 190, 8057 Zurich, Switzerland. [12] Department of Physics, University of Milan, Via Celoria 16, 20133 Milan, Italy. [13] Max Planck Institute for Nuclear Physics, Saupfercheckweg 1, 69117 Heidelberg, Germany. [14] Istituto Nazionale di Fisica Nucleare, Sez. di Genova, Via Dodecaneso 33, 16146 Genoa, Italy. [15] Institute of Physics and Technology, University of Bergen, Allégaten 55, 5007 Bergen, Norway. [16] Department of Physics, University of Oslo, Sem Sælandsvei 24, 0371 Oslo, Norway. [17] Department of Physics, University of Genoa, Via Dodecaneso 33, 16146 Genoa, Italy. [18] Stefan Meyer Institute for Subatomic Physics, Austrian Academy of Sciences, Boltzmanngasse 3, 1090 Vienna, Austria. [19] Department of Physics, University of Pavia, Via Bassi 6, 27100 Pavia, Italy. [20] Joint Institute for Nuclear Research, Dubna 141980, Russia. [21] Istituto Nazionale di Fisica Nucleare, Sez. di Padova, Via Marzolo 8, 35131 Padua, Italy. [22] Institute of Nuclear Physics of Lyon, CNRS/IN2P3, University Lyon 1, 69622 Villeurbanne, France. [23] Czech Technical University in Prague, FNSPE, Břehová 7, 11519 Prague 1, Czech Republic. [24] Department of Physics and INFN Bologna, University of Bologna, Via Irnerio 46, 40126 Bologna, Italy. [25] Department of Physics, University of Napoli Federico II, Via Cinthia, 80126 Naples, Italy. Correspondence and requests for materials should be addressed to P.B. (email: antiprotons@matterwave.de).

The precise measurement of forces between objects gives deep insight into the fundamental interactions and symmetries of nature. A paradigm example is the comparison of the motion of matter in the gravitational field, testing with high precision that the acceleration is material-independent, that is, the weak equivalence principle[1–4]. Although indirect experimental evidence suggests that the weak equivalence principle also holds for antimatter[5–7], a direct observation for antimatter is still missing. First attempts in this direction have recently been reported by the ALPHA collaboration[8], who used the release of antihydrogen from a magnetic trap to exclude the absolute value of the gravitational acceleration of antihydrogen to be 100 times larger than for matter. An alternative approach is followed by the GBAR collaboration[9], which is based on sympathetic cooling of positive antihydrogen ions and their subsequent photodetachment. One of the specified goals of the AEgIS collaboration (antihydrogen experiment: gravity, interferometry, spectroscopy) is the direct detection of the gravitational acceleration using an antihydrogen beam[10,11] combined with a moiré deflectometer[12], a device with high sensitivity for acceleration measurements.

Here, we present the successful realization of such a device for antiprotons. This has been achieved using slow antiprotons from the Antiproton Decelerator (AD) at CERN, the technology of emulsion detectors developed for recent high-energy neutrino experiments[13] and a novel referencing method employing Talbot–Lau interferometry[14,15] with light. The observation is consistent with a force at the 500 aN level acting on the antiprotons. This demonstration is an important prerequisite for future studies of the gravitational acceleration of antimatter building on an antihydrogen beam.

Results

Moiré deflectometer. The principle used in the experiment reported here is visualized in Fig. 1a. A divergent beam of antiprotons enters the moiré setup consisting of three equally spaced elements: two gratings and a spatially resolving emulsion detector. The two gratings with periodicity d define the classical trajectories leading to a fringe pattern with the same periodicity at the position of the detector. If the transit time of the particles through the device is known, absolute force measurements are possible by employing Newton's second law of mechanics[16]. As indicated in Fig. 1b, the position of the moiré pattern is shifted in the presence of a force with respect to the geometric shadow by

$$\Delta y = \frac{F_{\parallel}}{m}\tau^2 = a\tau^2, \qquad (1)$$

where $F_{\parallel}$ represents the force component along the grating period, m is the inertial mass of the test particle, a is the acceleration and τ is the time of flight between the two gratings. It is important to note that the shift has two contributions. The velocity of the particle after the second grating in the direction of the acceleration is non-zero and the particle is also accelerated in the second half of the moiré deflectometer. The relevant parameter for precision measurements is the sensitivity, that is, the minimal detectable acceleration a_{min}. This can be estimated by considering the maximal signal S to noise ratio possible in this scenario. Since the influence of a pattern shift is most sensitively detected at the steepest gradient of the pattern the visibility $\upsilon = (S_{\mathrm{max}} - S_{\mathrm{min}})/(S_{\mathrm{max}} + S_{\mathrm{min}})$ should be maximized and the periodicity minimized. The noise of the signal is intrinsically limited for classical particle sources to the shot noise which scales as $1/\sqrt{N}$, where N is the number of detected particles. Consequently, the minimal detectable acceleration[12] is given by $a_{\mathrm{min}} = d/\left(2\pi\upsilon\tau^2\sqrt{N}\right)$. It is important to note that this device works even for a very divergent source of particles as shown in Fig. 1a, and thus is an ideal device for the highly divergent beam of antihydrogen atoms that is expected in the AEgIS apparatus.

Talbot–Lau interferometry with light as absolute reference. To determine the magnitude of the fringe pattern shift, knowledge of the undeflected fringe position (indicated as grey trajectories in Fig. 1b) is required. Due to the neutrality and high speed of photons, it is favourable to measure this position independently with light so that the action of forces is negligible. Unlike the case of classical particles described above, geometric paths are not applicable for visible light as diffraction at the gratings has to be taken into account. Figure 1c depicts the corresponding light field pattern where the distance between the gratings is given by the Talbot length $L_{\mathrm{Talbot}} = 2d^2/\lambda$. This configuration is known as Talbot–Lau interferometer[14], which is based on the near-field Talbot effect[15]—the rephasing of the pattern in discrete distances behind a grating illuminated with light. The final pattern is not a classical distribution, but an interference pattern and coincides with the pattern of the moiré

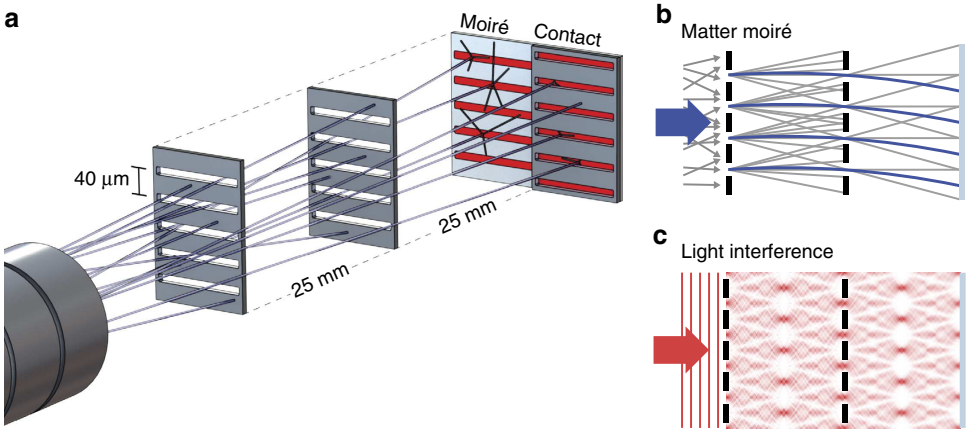

Figure 1 | Moiré deflectometer for antiprotons. (**a**) A divergent antiproton beam impinges on two subsequent gratings that restrict the transmitted particles to well-defined trajectories. This leads to a shadow fringe pattern as indicated in **b**, which is shifted in the presence of a force (blue trajectories). Finally, the antiprotons are detected with a spatially resolving emulsion detector. To infer the force, the shifted position of the moiré pattern has to be compared with the expected pattern without force. (**c**) This is achieved using light and near-field interference, the shift of which is negligible. A grating in direct contact with the emulsion is used to reference the antimatter and the light measurements.

deflectometer experiencing no acceleration. Thus, light provides the required absolute zero-force reference. The only prerequisite is that the Talbot length (or a multiple integer of it) is matched to the distance between the gratings and the detector. With that, the absolute shift of the antimatter pattern can be directly accessed and systematic errors can be significantly reduced as the moiré deflectometer and Talbot–Lau interferometer use the same gratings. We would like to stress that Talbot–Lau interferometry is also possible for matter waves such as atoms and molecules[17,18] if their de Broglie wavelength is long enough.

Experimental implementation. The experiment was performed within the AEgIS apparatus designed to produce antihydrogen for a future measurement of the gravitational acceleration[10,19]. A beam of antiprotons with a broad energy distribution, delivered by the AD at CERN, is realized after the 5.3 MeV antiprotons are transmitted through degrader foils with a total thickness of 225 μm (170 μm of aluminium and 55 μm of silicon). The simulated distribution has a mean energy of 106 keV and a root mean squared value of about 150 keV (see Methods). After traversing a 3.6-m long tube within two homogeneous magnetic fields of 5 T and 1 T, the antiprotons enter the deflectometer. We estimate the mean de Broglie wavelength to be 8.8×10^{-14} m, which implies that the concept of classical paths for the trajectories of the antiprotons is applicable for our gratings with a periodicity of 40 μm.

The grating holder is compact (25 mm distance between the gratings) so that the passive stability of the relative positions between the gratings for the long measurement time of 6.5 h is ensured. The slit arrays are manufactured in silicon by reactive ion etching, leading to a 100-μm thick silicon membrane with a slit width of 12 μm and a periodicity of $d = 40$ μm. Low-energy antiprotons hitting the slit array annihilate on the surface of the array and do not reach the detector. For this measurement, the final pattern, that is, the annihilation positions of antiprotons after passing two gratings, is detected by an emulsion detector. The moiré deflectometer and the annihilation detector are mounted in a vacuum chamber (10^{-5} mbar) on the extraction line of the AEgIS apparatus. After the exposure to antiprotons, the emulsion detector is removed, developed and analysed with an automatic microscope available at one of the participating institutions to determine the location of single annihilations. This facility was initially developed for the detection of neutrino-induced τ-leptons by the OPERA experiment[13]. The development of emulsion detectors for the application presented here, which involves operation in vacuum, is described in refs 20,21.

After removal of the emulsion detector the pattern of the Talbot–Lau interferometry with light was recorded in a subsequent measurement. For this purpose, the grating holder was homogenously illuminated by an incoherent light source (red light-emitting diode with spatial diffuser). For a wavelength of $\lambda = 640$ nm, the Talbot distance is $L_{\mathrm{Talbot}} = 2d^2/\lambda \approx 5$ mm. Thus, for our setup ($L = 25$ mm), we analyse the fifth rephasing of the light waves. The light pattern was directly recorded at the plane of the emulsion with a high-resolution flatbed charge-coupled device scanner (2.7 μm resolution). To align the antiproton and light measurement in the experiment reported here, an independent spatial reference is implemented. For that purpose we installed an additional transmission grating in direct contact with the detector plane. Contact grating and moiré deflectometer (see Fig. 1a) were simultaneously illuminated: first with antiprotons and subsequently with light. In each case, the pattern behind the contact grating is a simple shadow without any force dependence, and thus can be used as a reference for alignment.

Antimatter fringe patterns. With the emulsion detector, the positions of the annihilation vertices can be detected with a typical resolution of 2 μm (see Fig. 2a). The fragments produced by the annihilation of antiprotons lead to a characteristic star-shaped pattern, which can be observed with the microscope (an example is depicted in Fig. 2a). The first observation of such an annihilation star succeeded shortly after the discovery of the antiproton using emulsions[22]. This allows for very robust and high-quality particle identification, which makes this detector practically background-free. In addition, this detector can detect the arrival of antiprotons over a large area and thus is compatible with an upscaling of the grating area necessary for experiments with a divergent antihydrogen beam.

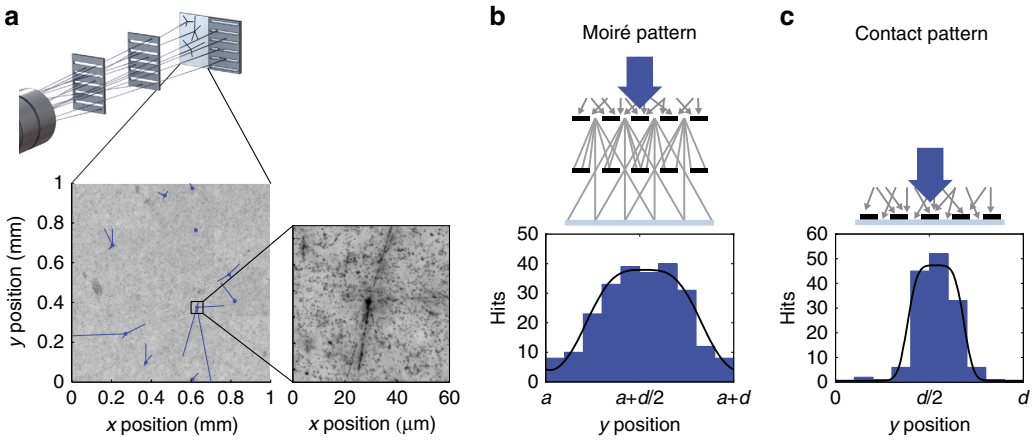

Figure 2 | Antiproton fringe pattern. (**a**) The spatial pattern of the antiprotons (highlighted as blue tracks) as detected by the emulsion detector in an exemplary area of 1 mm^2. The annihilation of an antiproton leads to a clear signal from which the annihilation vertex can be extracted with a precision of 2 μm by reconstruction analysing the emitted secondary particles. The image enlargement shows an exemplary annihilation star. (**b**) The fringe pattern after transmission through the moiré deflectometer setup reveals a visibility as high as (71 ± 10) %. Since less than one antiproton is detected per lattice period, the pattern shown is obtained by binning the vertical positions modulo the extracted periodicity of the fringe pattern. The solid black line denotes the expected distribution. (**c**) The pattern behind a grating placed directly on the emulsion detector ('contact') is a simple shadow that is smeared out due to the finite resolution of the detection. The few background events are consistent with independently observed grating defects. This pattern is used as a reference with no force dependence since the transit time is zero. The position of the moiré fringe pattern (indicated as offset a) is measured using light.

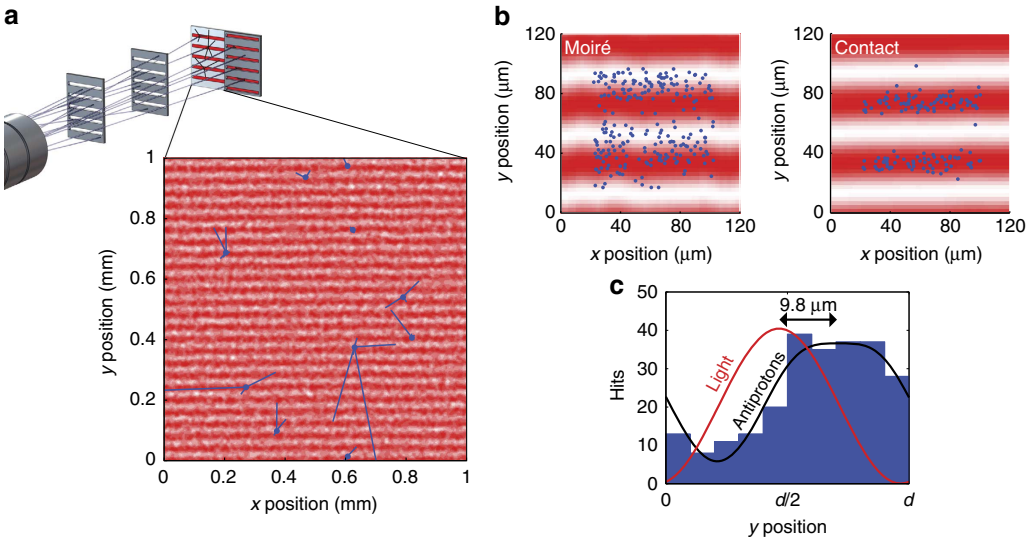

Figure 3 | Comparison between photon and antiproton patterns. (**a**) The spatial positions of the detected antiprotons (blue dots) are compared with the subsequently recorded light pattern (measured intensity indicated by the red shading). The Talbot-Lau fringe pattern provides the zero-force reference, presented here for the same exemplary detector area with ten annihilations as in Fig. 2a. (**b**) The antiproton and light measurements are aligned by overlaying the two patterns obtained with the contact grating. The result of this procedure is visualized on the right, where the annihilation positions of all antiprotons are folded into an area of $80 \times 80\,\mu m^2$. The moiré and Talbot-Lau pattern depicted on the left, without any further alignment, can be compared to determine a shift. (**c**) The data is projected onto the *y* axis for quantitative analysis. A relative shift between moiré and Talbot-Lau pattern indicates that a force is present. The observed mean shift of 9.8 μm is consistent with a mean force of 530 aN.

The pattern of 146 antiprotons detected for the grating in direct contact with the emulsion is depicted in Fig. 2c. The high visibility implies that the periodicity is well-defined in an area as large as $15 \times 6\,mm^2$ since the data collapses onto one fringe by taking the detected position modulo the extracted periodicity d of the pattern. To extract the periodicity, we employ the Rayleigh test[23] that is also widely used in astronomy[24]. The periodicity d and the relative rotation α of the pattern is found by maximizing

$$Z^2 = \frac{2}{n}\left[\left(\sum_{i=1}^{n}\sin\left(\frac{2\pi}{d}\cdot y_i\right)\right)^2 + \left(\sum_{i=1}^{n}\cos\left(\frac{2\pi}{d}\cdot y_i\right)\right)^2\right], \quad (2)$$

where n is the total number of antiprotons and $y_i = y'\cdot\cos\alpha + x'\cdot\sin\alpha$ depicts the antiproton's projected coordinate. This leads to an inferred periodicity of $40.22 \pm 0.02\,\mu m$, which is consistent with the expected emulsion expansion of $\sim 1\%$ and the nominal periodicity of 40 μm. It is interesting to note that the analysed area corresponds to 368 slits and, on average, only in every second slit an antiproton is detected.

In Fig. 2b, the observed moiré pattern for antiprotons is shown. The 241 events associated with antiproton annihilations were accumulated during the 6.5-h run of the experiment. The Rayleigh tests on sub-segments of the detected patterns reveal local distortion due to the expansion/shear of the emulsion and allow the identification of regions with negligible distortion. We have restricted the areas to two-thirds of their initial size, which ensures a position uncertainty due to shear to be smaller than $\pm 1.2\,\mu m$.

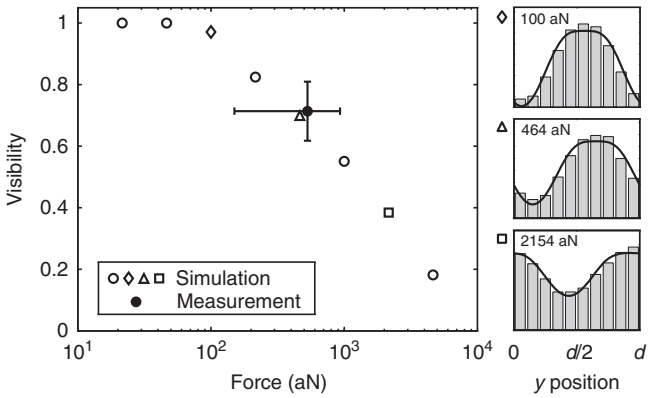

Figure 4 | Monte Carlo simulation. A detailed simulation study based on the expected energy distribution of the antiprotons (see Methods) shows the visibility for increasingly large forces. As the observed pattern in the presence of a force is an ensemble of differently shifted patterns corresponding to different transit times τ the visibility consequently decreases. The measured fringe pattern exhibits a visibility of (71 ± 10) % and is consistent with the result of this simulation. The error bar on the measured visibility is determined via resampling; the error bar on the measured force includes the systematic error bound and the one sigma statistical error bound. The observed high visibility excludes that the fringe pattern is shifted by more than one period and sets an upper limit for a force present without the necessity of referencing.

Absolute deflection measurement. To determine the absolute position of the antiproton fringe pattern (parameter a in Fig. 2b), we conduct a comparison with the measurement with light. The results are represented in Fig. 3a,b where the detected intensity is indicated by the red shading. The alignment is achieved by overlaying the contact patterns as depicted on the right of Fig. 3b. The moiré pattern can now be directly compared with the Talbot–Lau pattern (left of Fig. 3b) to extract a possible deflection.

For the quantitative analysis, we extract the orientation of the antimatter (Rayleigh test) and light patterns (Fourier transformation as the data is discrete in space). We find that the relative angle of the two antiproton patterns, which are 15 mm apart, deviates from the angle measured between the two corresponding light patterns by $\Delta\theta = 0.92 \pm 0.27$ mrad.

This observation is consistent with independent systematic studies of the distortion of emulsions on this large scale[25]. It is important to realize that this angle implies an intrinsic systematic

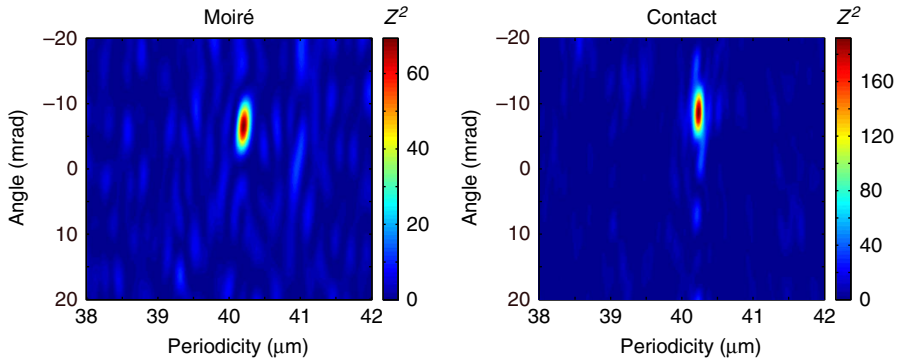

Figure 5 | Rayleigh test. The results of the Rayleigh test applied on the antiproton data of the moiré deflectometer and the contact grating show unambiguous maxima from which orientation and periodicity of the patterns are extracted.

uncertainty in the determination of the relative shift between the light and antimatter patterns since one cannot know which part has undergone the deformation. Assuming that both areas of the emulsion corresponding to contact and moiré have changed the same way on the centimetre scale, that is, half of the angular deviation for each pattern, we can compare the relative positions of the antiprotons with that of the light pattern as shown in Fig. 3b. The contact patterns on the right overlay as these are direct shadows of the grating (no force dependence), while an upward shift of the antiprotons in the force sensitive moiré pattern is noticeable. For quantitative analysis, we collapse the data onto one fringe (see Fig. 3c) and deduce the relative shift of $\Delta y_{\mathrm{mean}} = 9.8 \pm 0.9\,\mu\mathrm{m}$ (stat.) where the error is due to the uncertainties (one sigma) of the involved fits. Estimating a bound on the systematic uncertainties, we repeat our analysis assuming that either the contact or the moiré pattern has been changed due to the distortion. With that we find a minimal shift of $\Delta y_{\mathrm{min}} = 3.7 \pm 0.9\,\mu\mathrm{m}$ (stat.) and maximal shift of $\Delta y_{\mathrm{max}} = 16.4 \pm 0.9\,\mu\mathrm{m}$ (stat.) leading to a shift of $\Delta y_{\mathrm{mean}} = 9.8 \pm 0.9\,\mu\mathrm{m}$ (stat.) $\pm 6.4\,\mu\mathrm{m}$ (syst.).

Discussion

The observed shift of the moiré pattern is consistent with a force acting on the antiprotons. With the assumption of a mean velocity of $v = 4.5 \times 10^6\,\mathrm{m\,s^{-1}}$ implying a transit time of $\tau = 5.6$ ns, we find a mean force of $F = 530 \pm 50$ aN (stat.) ± 350 aN (syst.).

It is important to note that the mere observation of a pattern sets an upper bound for the force being present. The impinging antiproton beam has a very broad velocity distribution due to the degrading process in the foils. Thus, in the case that a force is present, the experimentally observed moiré pattern is an ensemble of differently shifted patterns corresponding to the transit times τ for different velocities. The results of a simulation of the performance of the moiré deflectometer are depicted in Fig. 4 and clearly reveal how the visibility vanishes for increasingly large forces (a force of 10 fN reduces the visibility below $\upsilon = 10\%$). The observed visibility of 71% is consistent with a mean force of ~ 500 aN. The visibility of the antiproton moiré pattern on its own (not relying on additional referencing) is an independent consistency check that the observed pattern is indeed shifted due to a force. Additionally with the observed high visibility of the moiré pattern, we exclude the possibility that the force has shifted the pattern by more than one period (see Fig. 4).

The measured force could arise from a Lorentz force either caused by an electric field of $\sim 33\,\mathrm{V\,cm^{-1}}$ in direction of the grating period or a magnetic field component of ~ 7.4 G perpendicular to the grating period and antiproton direction. The latter is compatible with the measured magnetic field of ~ 10 G at the position of the deflectometer due to the fringe field of the trapping region and stray fields of neighbouring experiments in the AD zone.

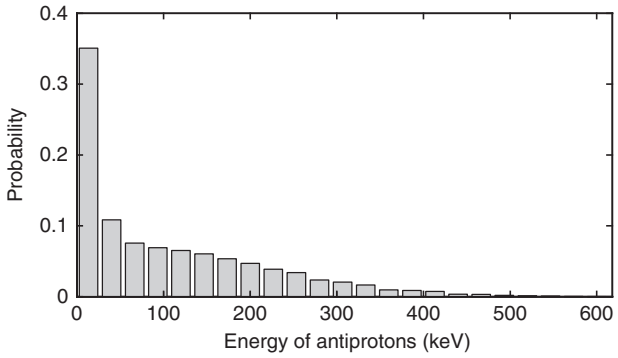

Figure 6 | Simulated energy distribution. A Monte Carlo simulation based on the Geant4 toolkit provides an estimate of the kinetic energy distribution of the antiprotons reaching the moiré deflectometer. This calculation takes into account the degrading foil system, the magnetic field and the geometry of the AEgIS apparatus.

The results presented are a crucial step towards the direct detection of gravitational acceleration of antihydrogen with the AEgIS experiment. Its concept is based on the formation of excited antihydrogen through the charge exchange reaction of electromagnetically trapped antiprotons with bunched Rydberg positronium. The resulting dipole moments of the antihydrogen atoms in a weak electric field allow their subsequent acceleration with electric field gradients, thus forming a beam towards the moiré deflectometer. The measurement of the antihydrogen's arrival position is realized by detection of the annihilation of its antiproton—thus using techniques presented here.

It is important to note that the expected absolute shift of the antihydrogen pattern due to gravity is comparable to the one observed in the current experiment. Although the gravitational force acting on antihydrogen is 10 orders of magnitude smaller than the sensitivity level reached with the presented small prototype deflectometer, the resolution of the setup can be simply improved by scaling up the deflectometer and the detector. A detailed discussion of the expected performance can be found in refs 10,19. The main improvement is achieved by increasing the transit time τ (see equation (1)). Using a beam of antihydrogen atoms with a significantly lower velocity of $\sim 500\,\mathrm{m\,s^{-1}}$ and a distance of 1 m between the gratings (this experiment $v = 4.5 \times 10^6\,\mathrm{m\,s^{-1}}$ and $L = 25$ mm) will improve the sensitivity by 11 orders of magnitude (eight orders of magnitude due to slower velocity and three orders of magnitude due to increased length of

the device), thus allowing the application of this technique to direct measurements of the gravitational force with antihydrogen.

High resolution is a prerequisite for the successful direct detection of the gravitational acceleration of antimatter. For absolute measurements, the sensitivity is the relevant parameter, which is ultimately limited by the intrinsic shot noise due to the detection of single atoms. Since the sensitivity scales with $1/\sqrt{N_{\mathrm{det}}}$ (N_{det} representing the number of detected particles) increasing the length of the moiré setup implies a similar expansion of the transverse dimensions to keep the throughput, and thus the flux, high. We have already successfully produced high-quality gratings with a transverse extent as large as 100 mm. The currently limiting systematic errors due to the distortion of the emulsion can be overcome by referencing the antihydrogen pattern directly to an *in situ*-realized light pattern, by employing emulsions on a glass substrate instead of the plastic used for this measurement or by the use of photomasks[25].

Methods

Orientation of the antiproton pattern. Collapsing the detected annihilation events to a single histogram as shown in Fig. 2 relies on the accurate determination of the periodicity as well as the angular orientation of the two dimensional fringe pattern. For this reason, we conduct the Rayleigh test given by equation (2) for different angles and periodicities and the results are depicted in Fig. 5 for the moiré and the contact pattern. The maximum is well-defined so that periodicity and angular orientation can be extracted for further analysis. The performance of the Rayleigh test has been tested with simulated data sets.

Velocity distribution. The kinetic energy of the antiprotons reaching the deflectometer is estimated with a simulation based on Geant4 (ref. 26). All the materials interposed along the beamline, between the AD antiproton beam (initial kinetic energy of 5.3 MeV) and the deflectometer, as well as the magnetic field and geometry of the AEgIS apparatus, are taken into account.

The input parameters of the Monte Carlo simulation are matched to meet the experimentally observed best antiproton trapping efficiency. This measurement was performed by counting the number of trapped antiprotons for various thicknesses of an aluminium degrader placed upstream of the antiproton trap. The thickness of the degrader foils used to slow down the antiprotons was selected in order to maximize the number of antiprotons with a kinetic energy lower than 10 keV that enter the antiproton trap and was set to 55 μm of silicon and 170 μm of aluminium. An additional foil of titanium (2 μm) is placed at the exit of the 1 T magnet. The energy distribution at the position of the deflectometer is depicted in Fig. 6. It is very broad and thus can be employed for setting limits on the maximum force present by analysing the visibility of the moiré pattern.

References

1. Galilei, G. *Discorsi e dimostrazioni matematiche intorno à due nuoue scienze* (Elsevirii, 1638).
2. Adelberger, E. G., Gundlach, J. H., Heckel, B. R., Hoedl, S. & Schlamminger, S. Torsion balance experiments: a low-energy frontier of particle physics. *Prog. Part. Nucl. Phys.* **62,** 102–134 (2009).
3. Fray, S., Diez, C. A., Hänsch, T. W. & Weitz, M. Atomic interferometer with amplitude gratings of light and its applications to atom based tests of the equivalence principle. *Phys. Rev. Lett.* **93,** 240404 (2004).
4. Kuroda, K. & Mio, N. Test of a composition-dependent force by a free-fall interferometer. *Phys. Rev. Lett.* **62,** 1941–1944 (1989).
5. Apostolakis, A. *et al.* Tests of the equivalence principle with neutral kaons. *Phys. Lett. B* **452,** 425–433 (1999).
6. Pakvasa, S., Simmons, W. A. & Weiler, T. J. Test of equivalence principle for neutrinos and antineutrinos. *Phys. Rev. D* **39,** 1761–1763 (1989).
7. Hughes, R. J. & Holzscheiter, M. H. Constraints on the gravitational properties of antiprotons and positrons from cyclotron-frequency measurements. *Phys. Rev. Lett.* **66,** 854–857 (1991).
8. The ALPHA Collaboration and Charman, A. E. Description and first application of a new technique to measure the gravitational mass of antihydrogen. *Nat. Commun.* **4,** 1785 (2013).
9. Perez, P. & Sacquin, Y. The GBAR experiment: gravitational behaviour of antihydrogen at rest. *Classical Quant. Grav.* **29,** 184008 (2012).
10. Drobychev, G. *et al.* (AEgIS collaboration) Proposal for the AEgIS experiment at the CERN Antiproton Decelerator. SPSC-P-334; CERN-SPSC-2007-017 (2007).
11. Doser, M. *et al.* Exploring the WEP with a pulsed cold beam of antihydrogen. *Classical Quant. Grav.* **29,** 184009 (2012).
12. Oberthaler, M. K., Bernet, S., Rasel, E. M., Schmiedmayer, J. & Zeilinger, A. Inertial sensing with classical atomic beams. *Phys. Rev. A* **54,** 3165–3176 (1996).
13. Agafonova, N. *et al.* (OPERA collaboration) Observation of a first ν_τ candidate event in the OPERA experiment in the CNGS beam. *Phys. Lett. B.* **691,** 138–145 (2010).
14. Lau, E. Beugungserscheinungen an Doppelrastern. *Ann. Phys.* **437,** 417–423 (1948).
15. Talbot, H. F. Facts relating to optical science No IV. *Philos. Mag.* **3,** 401–407 (1836).
16. Newton, I. *Philosophiæ Naturalis Principia Mathematica* (Jussu Societatis Regiæ ac Typis J. Streater, 1687).
17. Clauser, J. F. & Li, S. Talbot-von Lau atom interferometry with cold slow potassium. *Phys. Rev. A* **49,** R2213 (1994).
18. Berman, P. R. (ed.) *Atom Interferometry* (Academic Press, 1997).
19. Kellerbauer, A. *et al.* Proposed antimatter gravity measurement with an antihydrogen beam. *Nucl. Instr. Meth. Phys. Res. B* **266,** 351–356 (2008).
20. Aghion, S. *et al.* (AEgIS collaboration) Prospects for measuring the gravitational free-fall of antihydrogen with emulsion detectors. *JINST* **8,** P08013 (2013).
21. Amsler, C. *et al.* A new application of emulsions to measure the gravitational force on antihydrogen. *JINST* **8,** P02015 (2013).
22. Chamberlain, O. *et al.* On the observation of an antiproton star in emulsion exposed at the Bevatron. *Nuovo Cimento* **3,** 447–467 (1956).
23. Mardia, K. V. *Statistics of Directional Data* (Academic Press, 1972).
24. Gibson, A. I. *et al.* Transient emission of ultra-high energy pulsed γ rays from crab pulsar PSR0531. *Nature* **296,** 833–835 (1982).
25. Kimura, M. *et al.* A new method to correct deformations in emulsion using a precise photomask. *Nucl. Instr. Meth. Phys. Res. A* **711,** 1–7 (2013).
26. Agostinelli, S. *et al.* Geant4—a simulation toolkit. *Nucl. Instr. Meth. Phys. Res. A* **506,** 250–303 (2003).

Acknowledgements

This work was supported by: DFG research grant, excellence initiative of Heidelberg University, ERC under the European Union's Seventh Framework Program (FP7/2007–2013)/ERC Grant agreement no. (291242), Austrian Ministry for Science, Research and Economy, Research Council of Norway, Bergen Research Foundation, Istituto Nazionale di Fisica Nucleare (INFN- Italy). J.S. wishes to acknowledge the Swiss National Science Foundation. Technical support by the Cockcroft Institute, U.K. is gratefully acknowledged. We are grateful to the CERN AD team for providing the antiproton beam.

Author contributions

All authors contributed equally to the work presented.

Additional information

Competing financial interests: The authors declare no competing financial interests.

Reprints and permission information is available online at http://npg.nature.com/reprintsandpermissions/

How to cite this article: Aghion, S. *et al.* A moiré deflectometer for antimatter. *Nat. Commun.* 5:4538 doi: 10.1038/ncomms5538 (2014).